J. Fluid Mech. (2026), *vol.* 1034, P1, doi:10.1017/jfm.2026.11494

JFM PERSPECTIVES

Turbulence intermittency and velocity gradients

Dhawal Buaria[1,2] **and Alain Pumir**[2,3,4]

[1]Department of Mechanical and Aerospace Engineering, Texas Tech University, Lubbock, TX 79409, USA

[2]Max Planck Institute for Dynamics and Self-Organization, 37077 Göttingen, Germany

[3]CNRS, Ecole Normale Superieure de Lyon, LPENSL, UMR5672, 69342, Lyon CEDEX 07, France

[4]French American Center for Theoretical Science, CNRS, KITP, University of California, Santa Barbara, CA 83106-4030, USA

Corresponding author: Dhawal Buaria, dhawal.buaria@ttu.edu

(Received 28 March 2026; revised 28 March 2026; accepted 1 April 2026)

A central problem in turbulence is understanding small-scale intermittency, which refers to the sporadic generation of intense fluctuations in velocity gradients and increments. These extreme events, strongly non-Gaussian in nature, govern dissipation, mixing and transport processes in virtually all turbulent flows. Yet, despite decades of study, a faithful and predictive characterisation of small scales remains elusive owing to the inherent mathematical intractability of the Navier–Stokes equations and the difficulty in resolving them in both simulations and experiments at high Reynolds numbers. Recent advances in high-resolution simulations and experiments have significantly reshaped this picture, particularly by providing precise data at high Reynolds numbers to probe the full tensorial structure and dynamics at small scales. In this article, we synthesise the current understanding of small-scale intermittency and universality, drawing on modern data from well-resolved simulations and experiments that resolve the full velocity-gradient tensor. The results show that, while prevailing intermittency theories capture several key trends, they fail to describe or account for observed asymmetries between longitudinal and transverse fluctuations or between strain and vorticity amplification. Evidence suggests that intermittency is closely tied to the dynamics and geometry of vorticity and strain fields, with non-locality playing an important role. We argue that a consistent picture has emerged, but a complete theory will require unifying the statistical scaling frameworks with the underlying dynamical mechanisms that govern gradient amplification. Additional implications of these findings are discussed, and several pressing open problems are identified for future work.

Key words: turbulent flows, turbulence theory, intermittency

'Each advance in our understanding of turbulence seems to illuminate one layer of complexity while uncovering another beneath.'

Contents

1. Introduction

Turbulence hardly needs an introduction, as it is one of the most striking and ubiquitous phenomena in nature, influencing systems across an extraordinary range of scales and contexts. Representing the chaotic and unpredictable motion of fluids, turbulence governs physical processes in the atmosphere and the oceans, shaping ecosystems, weather patterns, air quality, global circulation and the global climate system. Its importance extends well beyond our planet to astrophysical phenomena, driving the formation of stars and galaxies and shaping the universe on the largest scales. Turbulence is equally indispensable in engineering: it dictates how fluids are transported through ducts and pipes, around vehicles and structures and underpins the efficiency of energy conversion in engines, reactors and turbines.

Despite its ubiquity and obvious importance, turbulence remains notoriously difficult to characterise and predict. What makes the problem particularly compelling is that, unlike many other frontiers of physics, turbulence is both directly observable in everyday life and firmly rooted in well-established conservation laws. These laws have been known for over two centuries and are conceptually straightforward to write down, yet they conceal extraordinary complexity. For low-speed flows (relative to speed of sound) in Newtonian fluids such as water and air, turbulence is described by the incompressible Navier–Stokes equations (INSE):

$$\begin{aligned} \frac{\partial u_i}{\partial x_i} &= 0, \\ \frac{\partial u_i}{\partial t} + u_j \frac{\partial u_i}{\partial x_j} &= -\frac{\partial P}{\partial x_i} + \nu \nabla^2 u_i + f_i, \end{aligned} \tag{1.1}$$

where u_i is the velocity field ($i = 1, 2, 3$), P is the kinematic pressure (which is pressure divided by fluid density), ν is the fluid kinematic viscosity and f_i is a forcing term. These equations can be non-dimensionalised using characteristic velocity and length scales, U and L, respectively, which typically represent the motion of the fluid at the size of the system. This leads to the introduction of the Reynolds number $Re = UL/\nu$, which can be loosely interpreted as the ratio of inertial and viscous forces.

The complexity of turbulence is, at its core, a mathematical one. The challenge lies not in formulating the INSE but in solving them in the turbulent regime where Re is very large. In this regime, inertial forces overwhelm viscous forces, producing a vast hierarchy of interacting scales that extend from the size of the system down to dissipative eddies, which are orders of magnitude smaller. The INSE as written above represent the simplest kind of turbulence, where Re is the sole control parameter. Even in this ostensibly minimal case, no general solutions are known. In fact, even the basic question of whether smooth solutions to the INSE exist for all times remains unresolved, standing as one of the Clay Millennium Prize Problems (Fefferman 2006). The intractability of the INSE stems from two core aspects: nonlinearity and non-locality. The nonlinearity is evident from the advective term, whereas the non-locality is implicitly hidden in the pressure term. This can be made explicit by taking the divergence of INSE, leading to a Poisson equation for pressure

$$\nabla^2 P = -A_{ij}A_{ji}, \tag{1.2}$$

where $A_{ij} \equiv \partial u_i/\partial x_j$ is the velocity-gradient tensor. Thus, the INSE are, in effect, partial integro-differential equations, where the evolution of the flow at any given point is nonlinearly coupled to the state of the entire field.

One may argue that exact solutions are not always necessary for technological progress; after all, the Wright brothers successfully engineered the first aircraft (1903) even before Prandtl's boundary-layer theory (1904) was established. Since then, engineers have devised increasingly sophisticated methods to deal with turbulence for design purposes, for example to predict quantities like lift, drag and heat transfer. Still, a faithful description of turbulence across all scales is essential for problems that transcend conventional design. For instance, flows in the atmosphere or oceans are governed not only by planetary-scale motions but also by processes occurring at centimetre to millimetre scales, where essential mixing, entrainment and transport occur. Cloud formation, pollutant dispersion, mixing in the ocean, all hinge on dynamics that require a deeper theoretical and predictive understanding of turbulence (Thorpe 2005; Bodenschatz *et al.* 2010; Wyngaard 2010). Even otherwise, advances in turbulence modelling for engineering applications are invariably tied to theoretical progress.

Given the lack of a general method for solving the INSE, the turbulence problem has necessarily splintered into several problems, each shaped in its own way by large-scale conditions tied to flow geometry, particularly presence of walls, and the physical effects under consideration. Shear flows, wall-bounded turbulence, rotating and stratified turbulence, magnetohydrodynamic turbulence and compressible turbulence, each present unique challenges, and progress in one regime does not necessarily translate directly to another. The physical effects typically show up directly through the forcing term f_i in (1.1), possibly involving other fields (such as a temperature, salinity or magnetic field) – making it extremely challenging, perhaps impossible, to construct a single 'theory of turbulence' that accounts for all cases. Nevertheless, the interaction of a vast range of scales, as encoded by the nonlinear terms of the INSE, is a fundamental trait shared by all flows. Thus, a central goal of a turbulence theory, if any, is to understand how energy and information are transferred across scales through these nonlinear interactions, even under simplifying assumptions of homogeneity and isotropy. The essential idea is that uncovering any universal rules that govern the scale-to-scale dynamics provides a baseline for understanding turbulence itself. Thereafter, additional physics can be meaningfully built upon this baseline, depending on the specific problem.

A landmark step in this direction came with the work of Kolmogorov (1941), which proposed a statistical description of turbulence, rooted in universality of small-scale fluctuations, independent of forcing or geometry. Building upon the observation of Richardson (1922), his phenomenology envisioned a self-similar cascade, whereby energy injected into the system at large scales is progressively redistributed to smaller scales through nonlinear interactions, until it gets dissipated into heat by viscosity. Such a cascade allows large-scale anisotropies to be progressively forgotten, with isotropy and universality emerging at small scales. This idea has been enormously influential, shaping much of turbulence research since its inception, and providing the foundation upon which most present-day theories and models of turbulence have been developed. Its reach also extends beyond fluid mechanics, informing problems in nonlinear physics, critical phenomena, astrophysics and even finance (Ghashghaie *et al.* 1996; Bramwell, Holdsworth & Pinton 1998).

While Kolmogorov's original work essentially hypothesised a mean-field description for the energy cascade and accompanying small-scale statistics (such as those of velocity increments and gradients), it was soon realised that this picture is incorrect. Instead, the energy cascade is highly sporadic and spatially uneven, a phenomenon termed intermittency, giving rise to strongly non-Gaussian behaviour in small-scale statistics. An enormous amount of research has since been devoted to understanding small-scale turbulence and intermittency. In the second half of 20th century, much of the progress was initially driven by laboratory experiments, cementing intermittency as a central aspect of turbulence, and motivating new theoretical frameworks rooted in multifractality (Frisch 1995; Sreenivasan & Antonia 1997).

Towards the end of 20th century, direct numerical simulations (DNS) of the INSE began to emerge as a transformative tool in turbulence research. While initially restricted to low Reynolds numbers, DNS provided unfettered access the full three-dimensional (3-D) velocity field, and thus any other conceivable quantities. This capability revolutionised the study of turbulence by enabling an unprecedented scrutiny of the small-scale dynamics. Most notably, DNS grants the full knowledge of the velocity-gradient tensor A_{ij}, which governs the local stretching, rotation and dissipation, and encodes the intricate coupling between strain and vorticity that drives the cascade. In fact, as we saw in (1.2), the non-locality of the INSE is also mediated by the gradients. While DNS were originally restricted to low Re, the sustained exponential growth of computing power has allowed DNS to advance to high Reynolds numbers, comparable to those available in most laboratory experiments. This allows one to reliably extract asymptotic scaling laws (which were once only accessible in experiments), while still having access to the full tensorial dynamics of the flow. Experiments of course continue to play a central and irreplaceable role in turbulence research, and modern measurements techniques can now access velocity gradients directly, albeit at relatively low Reynolds numbers. However, at high Re, experimental measurements are typically restricted to 1-D surrogates of the velocity field, making DNS an essential complement in probing the small-scale structure of turbulence.

The goal of this Perspective is to synthesise current understanding of turbulence intermittency and small-scale universality, and also highlight open questions that continue to challenge it. Given the enormous body of existing literature on the subject, it is neither possible nor intended to offer an exhaustive review. Instead, our viewpoint will be built around the velocity-gradient tensor as a fundamental descriptor of small-scale turbulence, emphasising its role in linking phenomenology, statistics and the underlying dynamics. Our discussion draws primarily on insights from recent well-resolved DNS of homogeneous isotropic turbulence, but also incorporates findings from laboratory experiments and DNS of wall-bounded flows to underscore the universality of the observed small-scale dynamics. This article complements and extends the perspective of Dubrulle (2019), which focused on the cascade dynamics and inertial-range intermittency, relying primarily on experimental data, and also the recent review by Johnson & Wilczek (2024), which focused on the average gradient and cascade dynamics along with reduced-order modelling.

In what follows, we first provide background on the dynamics of velocity gradients derived from INSE, setting the stage for the mechanisms that govern small-scale dynamics. We then revisit the foundations of Kolmogorov's phenomenology and the emergence of intermittency, tracing how these classical ideas have evolved into modern intermittency theories. Their predictions are compared against available data, primarily from high-resolution DNS, complemented where possible by laboratory experiments. Although these theoretical frameworks explain many observed trends, they also fail to reproduce several important features. To address these issues, we turn to the dynamics of strain and vorticity amplification and also examine the role of non-local interactions. Finally, we summarise the key insights gained and discuss open questions and possible directions for future work.

2. Navier–Stokes dynamics and velocity-gradient amplification

2.1. *Energy budget and the zeroth law of turbulence*

A natural consequence of viscosity is that kinetic energy is irreversibly dissipated in a moving fluid. This obviously bears out in our everyday experiences, whether stirring a cup of coffee, pumping water through a pipe or the motion of a fan. In each case, motion is damped by internal friction, as mechanical energy is converted into heat at the molecular level. One can mathematically formalise this by taking the dot product of INSE with $\boldsymbol{u}$ and integrating over the spatial domain. Using standard vector identities, the incompressibility condition in (1.1) and appropriate boundary conditions (e.g. no-slip walls or periodicity), we arrive at the energy-budget equation

$$\frac{1}{2}\frac{\partial}{\partial t}\langle|\boldsymbol{u}|^2\rangle = \langle \boldsymbol{f}\cdot\boldsymbol{u}\rangle - \nu\langle|\boldsymbol{\nabla}\boldsymbol{u}|^2\rangle, \tag{2.1}$$

where $\langle\cdot\rangle$ denotes a spatial average (or an ensemble average under ergodic assumptions). Despite its simplicity, the above equation captures the essential energetics of turbulence. The left-hand side quantifies the rate of change of kinetic energy. On the right-hand side, the forcing term produces energy, as described by $\mathcal{P}\equiv\langle \boldsymbol{f}\cdot\boldsymbol{u}\rangle$, while the viscous term always acts to dissipate energy. The mean dissipation rate is defined as

$$\langle\epsilon\rangle = \nu\langle|\boldsymbol{\nabla}\boldsymbol{u}|^2\rangle. \tag{2.2}$$

Evidently, in the absence of any forcing ($\boldsymbol{f}=\boldsymbol{0}$ and $\mathcal{P}=0$), the kinetic energy monotonically decreases and turbulence quickly decays.

On the other hand, if energy is continuously injected into the system, a statistically stationary state may be established whereby the energy injection and dissipation balance each other, i.e. $\mathcal{P}=\langle\epsilon\rangle$. In most turbulent flows, the injection of energy occurs at scales of system size, i.e. the largest scales. For instance, consider a fan driving the flow in a room, or a pressure gradient driving the flow through a pipe. In contrast, the viscous dissipation term, governed by the gradients of velocity, acts only at smallest scales (to be formally defined later), which are typically orders of magnitude smaller than the system size. This separation of scales between energy injection and dissipation establishes the notion of an energy cascade, wherein energy gets transferred from large to small scales before being dissipated. In fact, this multiscale nature is intrinsic to all turbulent flows, underpinning much of their complexity.

An important question arising from (2.2) is what happens to the dissipation rate as ν becomes very small (approaching zero) or equivalently the Reynolds number *Re* becomes very large (approaching infinity), as encountered in turbulence. Naively, one may expect the dissipation rate to vanish in the limit $\nu\to 0$. Instead, observations suggest a remarkable behaviour that the dissipation rate instead approaches a finite constant. From dimensional considerations, one can write: $\langle|\boldsymbol{\nabla}\boldsymbol{u}|^2\rangle \simeq (U/L)^2 f(Re)$, where $f(\cdot)$ is some non-dimensional function of *Re*. It follows that $\langle\epsilon\rangle \simeq (U^3/L)\ f(Re)/Re$. Empirically, one finds that $\langle\epsilon\rangle \sim U^3/L$ and $f(Re)/Re \simeq 1$. This behaviour is illustrated in figure 1, which shows the ratio $\langle\epsilon\rangle L/U^3$ as a function of Reynolds number as obtained from various DNS of isotropic turbulence. While there are some minor variations, possibly arising due to

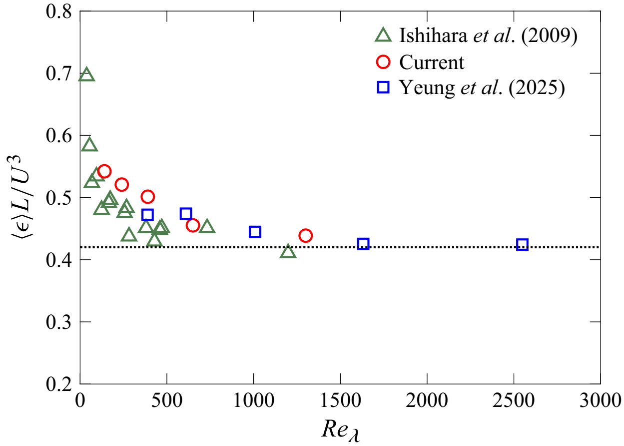

Figure 1. Mean energy-dissipation rate, $\langle\epsilon\rangle$ normalised by U^3/L from DNS of isotropic turbulence, where U is the root-mean-square (r.m.s.) of the velocity fluctuations, and L is the integral scale. The data are shown as a function of the Taylor-scale Reynolds number Re_λ (defined by (4.1)), which is proportional to $Re^{1/2}$. In the limit $Re_\lambda \rightarrow \infty$, the value of the ratio appears to asymptote to $C_\epsilon \approx 0.42$. The current database is summarised in table 1, the green triangles are from Ishihara, Gotoh & Kaneda (2009), whereas the blue squares are from Yeung *et al.* (2025), which differ somewhat in the details of large-scale forcing, and thus might asymptote to slightly different constants.

differences in forcing, the numerical evidence that the ratio $\langle\epsilon\rangle L/U^3$ is approaching a constant (independent of Reynolds number) is very strong.

While figure 1 is restricted to DNS data, dissipation anomaly has been even more strongly confirmed in experiments across numerous flow configurations (Sreenivasan 1998; Pearson, Krogstad & van de Water 2002; Vassilicos 2015; Dubrulle 2019) – establishing it as a cornerstone of turbulence research, so much so that it is often referred to as the 'zeroth law of turbulence'. However, the asymptotic limit of the ratio $\langle\epsilon\rangle \sim U^3/L$ as $Re \rightarrow \infty$ appears to be flow-dependent (Sreenivasan 1998; Vassilicos 2015). It is worth noting that dissipation anomaly has only been established empirically. Since the incompressible Euler equations are recovered from the INSE in the limit $\nu \rightarrow 0$, the expectation, first conjectured by Onsager (1949), is that turbulent solutions of the INSE correspond to singular solutions of the Euler equations, which anomalously dissipate energy (without viscosity). While a formal mathematical proof of this conjecture remains elusive, much progress has been made on this front. We refer interested readers to a recent review of the topic by Eyink (2024).

It follows from dissipation anomaly that velocity-gradient fluctuations must become increasingly intense as ν decreases, with its variance scaling as $\langle|\boldsymbol{\nabla u}|^2\rangle \sim \langle\epsilon\rangle/\nu$. This scaling naturally highlights a characteristic time scale: $(\nu/\langle\epsilon\rangle)^{1/2}$, of the smallest scales, where viscous dissipation dominates. In fact, it is easy to realise that additional dimensional groups can be formed using ν and $\langle\epsilon\rangle$, which characterise the viscous scales. This foundational idea indeed paved the way for Kolmogorov's 1941 theory, which formalises the statistical description of small scales and will be discussed in § 3.

2.2. *Velocity-gradient dynamics*

The amplification of velocity gradients is evidently a fundamental ingredient for the zeroth law of turbulence. In fact, the formation of large gradients is essential to the generation of small scales in the flow. It is therefore natural to investigate how velocity gradients evolve and amplify in turbulent flows. To do so, we define the velocity-gradient tensor $\boldsymbol{A} = \nabla \boldsymbol{u}$ and take the gradient of (1.1), yielding the evolution equation

$$D_t A_{ij} = -A_{ik}A_{kj} - H_{ij} + \nu \nabla^2 A_{ij}, \tag{2.3}$$

where $D_t = (\partial_t + \boldsymbol{u} \boldsymbol{\cdot} \nabla)$ is the material derivative and $\boldsymbol{H} = \nabla\nabla P$ is the pressure-Hessian tensor. In the above equation, we have ignored the contribution $\nabla \boldsymbol{f}$ from the forcing term, since it often acts on the largest scales and its local spatial variation is negligible for the dynamics of $\boldsymbol{A}$. Nevertheless, caution is warranted in certain flows, for instance, turbulence in the presence of rotation or stratification, where the forcing term can interact with velocity over the entire range of scales. The first term on the right-hand side of (2.3), a quadratic nonlinearity, governs the self-amplification (or attenuation) of gradients. The incompressibility condition: $A_{ii} = 0$, leads to the pressure Poisson equation given earlier in (1.2), highlighting the non-locality mediated by the pressure field.

While (2.3) is generally intractable, useful insight can be gained by considering simplified scenarios in which certain terms are approximated or neglected. One such simplification is the restricted Euler (RE) model, which ignores the viscous term and eliminates the non-locality, while preserving incompressibility, by assuming that the pressure-Hessian tensor is isotropic: $H_{ij} = (1/3)H_{kk}\delta_{ij} = -(1/3)A_{mn}A_{nm}\delta_{ij}$. The resulting system of ordinary differential equations for $\boldsymbol{A}$ is closed and can, in fact, be solved analytically for any specified initial condition $\boldsymbol{A}_0 = \boldsymbol{A}(t_0)$ (Vieillefosse 1982; Cantwell 1992). However, for almost all initial conditions, the RE model exhibits a finite-time singularity, with the gradient norm scaling as $||\boldsymbol{A}(t)|| \sim 1/(t^* - t)$. This blow-up is a direct manifestation of the self-amplification due to the quadratic nonlinearity. For the INSE, viscosity is expected to regularise any potential blow-up, but the situation is obviously more complicated because of the non-local pressure Hessian. However, the insight from the RE model clearly highlights the tendency for gradients to amplify, the more so as viscosity gets weaker, qualitatively aligning with the emergence of the dissipation anomaly. Nevertheless, as we will observe soon, the dynamics of gradients in turbulent flows extends beyond what is captured by dissipation anomaly, with fluctuations of gradients being significantly larger than their r.m.s. values.

2.2.1. *Strain and vorticity*

To fully analyse the dynamics of $\boldsymbol{A}$, it is necessary to consider its full tensorial structure. To that end, it is particularly useful to decompose $\boldsymbol{A}$ into its symmetric and skew-symmetric parts, respectively, corresponding to the strain-rate tensor and vorticity vector

$$S_{ij} = \frac{1}{2}(A_{ij} + A_{ji}), \qquad \omega_i = (\nabla \times \boldsymbol{u})_i = \varepsilon_{ijk}A_{kj}, \tag{2.4}$$

where ε_{ijk} is the Levi-Civita symbol. In principle, the skew-symmetric part of $\boldsymbol{A}$ is directly given by the rotation-rate tensor: $R_{ij} = (1/2)(A_{ij} - A_{ji})$, but it is synonymous with the vorticity vector, since $\omega_i = -\varepsilon_{ijk}R_{jk}$. The evolution equations for the strain and vorticity deduced from (2.3) are

$$\frac{\mathrm{D}\omega_i}{\mathrm{D}t} = \omega_j S_{ij} + \nu \nabla^2 \omega_i, \tag{2.5}$$

$$\frac{\mathrm{D}S_{ij}}{\mathrm{D}t} = -S_{ik}S_{kj} - \frac{1}{4}\left(\omega_i\omega_j - \omega^2\delta_{ij}\right) - H_{ij} + \nu\nabla^2 S_{ij}\ , \tag{2.6}$$

where $\omega^2 = \omega_k\omega_k$. From the vorticity equation, we see that its nonlinear amplification is governed by the vector $W_i = \omega_j S_{ij}$, which is typically associated with the stretching and amplification of vorticity by strain, but generally also captures the effects of vortex compression/attenuation and tilting by strain. In contrast, strain self-amplifies through a quadratic nonlinearity (same as for $\boldsymbol{A}$), but with additional feedback from vorticity. The pressure-Hessian tensor, given its symmetric form, only contributes to the evolution of the strain. But since vorticity is amplified by strain, the pressure Hessian still indirectly influences vorticity amplification.

To quantify the intensity of strain and vorticity, it is convenient to use their square-norms, defined as

$$\varOmega = \omega_i \omega_i, \quad \varSigma = 2 S_{ij} S_{ij}, \tag{2.7}$$

where the former is the enstrophy and the latter is the dissipation rate divided by viscosity, i.e. $\varSigma = \epsilon/\nu$. Note that the dissipation rate is formally defined as $\epsilon = 2\nu S_{ij} S_{ij}$, but in homogeneous turbulence it is easy to show that their averages are equal: $\langle \varOmega \rangle = \langle \varSigma \rangle = \langle \epsilon \rangle / \nu = \langle A_{ij} A_{ij} \rangle$. These magnitudes provide a natural measure of local gradient intensity relative to the mean and serve as convenient diagnostics to identify regions of strong rotation and stretching in turbulent flows.

As hinted earlier, gradients in turbulence can be far more intense than what is implied by dissipation anomaly. This can be qualitatively established by visualising $\varOmega$ and $\varSigma$, as shown in figure 2. The figure demonstrates that intense gradients are spatially inhomogeneous, concentrating into coherent structures that dominate the small-scale dynamics. Vorticity tends to concentrate in elongated tube-like regions (vortex tubes), while strain organises into thin, sheet-like structures, often wrapping around vortex tubes. Despite their spatial sparsity, these structures maintain remarkable coherency even at very high intensities. Moreover, while their distribution is inhomogeneous, their coherency persists remarkably well even at very high intensities. This organisation of small-scale gradients has been repeatedly observed in both DNS and laboratory experiments (Jiménez *et al.* 1993; Zeff *et al.* 2003; Ishihara *et al.* 2007; Buaria *et al.* 2019) and underpins much of the intermittency phenomena discussed in later sections.

2.2.2. *The Q-R plane*

An alternative way to study the dynamics of velocity-gradient tensor is through its principal invariants defined as

$$Q = -\frac{1}{2} A_{ij} A_{ji} = \frac{1}{4} (\varOmega - \varSigma), \tag{2.8}$$

$$R = -\frac{1}{3} A_{ij} A_{jk} A_{ki} = -\frac{1}{4} \omega_i \omega_j S_{ij} - \frac{1}{3} S_{ij} S_{jk} S_{ki}, \tag{2.9}$$

which arise naturally in the characteristic polynomial of the velocity-gradient tensor

$$p_A(\lambda) \equiv \det(\boldsymbol{A} - \lambda \boldsymbol{I}) = -\lambda^3 - Q\lambda + R, \tag{2.10}$$

where λ corresponds to the eigenvalues. Note that the first principal invariant $P = A_{ii}$ is zero from incompressibility, eliminating the quadratic term in the polynomial. Another motivation for using the invariants comes from the RE model, for which the tensorial equations reduce to a closed dynamical system: $(\mathrm{d}/\mathrm{d}t)\{Q, R\} = \{-3R, -2Q^2/3\}$ (Vieillefosse 1982; Cantwell 1992). It is easy to show that these equations imply that $4Q^3 + 27R^2 = \text{const.}$ along trajectories in the Q-R plane. In the full Navier–Stokes dynamics, this is obviously not the case. Rather, the sign of $(4Q^3 + 27R^2)$ determines the nature of the eigenvalues of A_{ij}, with negative leading to all real eigenvalues and positive leading to two eigenvalues being complex conjugates.

For homogeneous turbulence, one can show that the averages are $\langle Q \rangle = 0$ and $\langle R \rangle = 0$ (Betchov 1956). The invariants therefore are often used to characterise the local flow

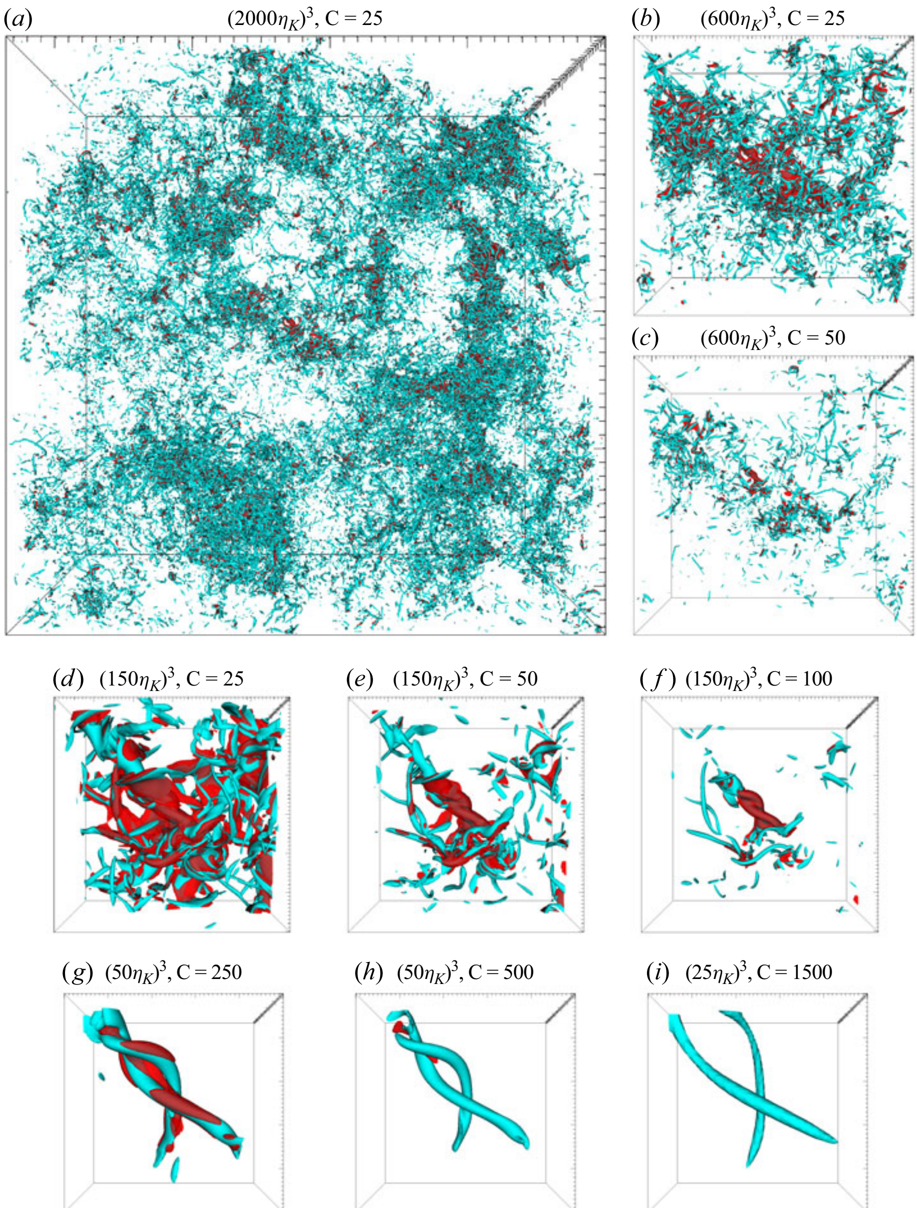

Figure 2. Perspective view of isosurfaces of enstrophy (cyan) and dissipation (red), normalised by their mean values. The fields correspond to a representative instantaneous snapshot from DNS of isotropic turbulence at $Re_\lambda = 650$ on a grid of size 8192^3, corresponding to $4096\eta_K^3$, where η_K is the Kolmogorov length scale, defined by (3.1). Starting from (*a*), we successively zoom in and also increase the contour threshold in other panels, such that all sub-domains share the same centre, which corresponds to the strongest gradient in the snapshot. Domain sizes together with the contour thresholds C are noted at the top of each panel.

topology. For instance, the sign and magnitude of Q distinguishes regions where vorticity dominates over strain (for $Q > 0$) and *vice versa* (for $Q < 0$), whereas that of R distinguishes their corresponding amplification and attenuation mechanisms. Thus, examining the joint probability distribution of Q and R offers a compact way to describe the local structure and dynamics of velocity gradients. Whereas a Gaussian ensemble of

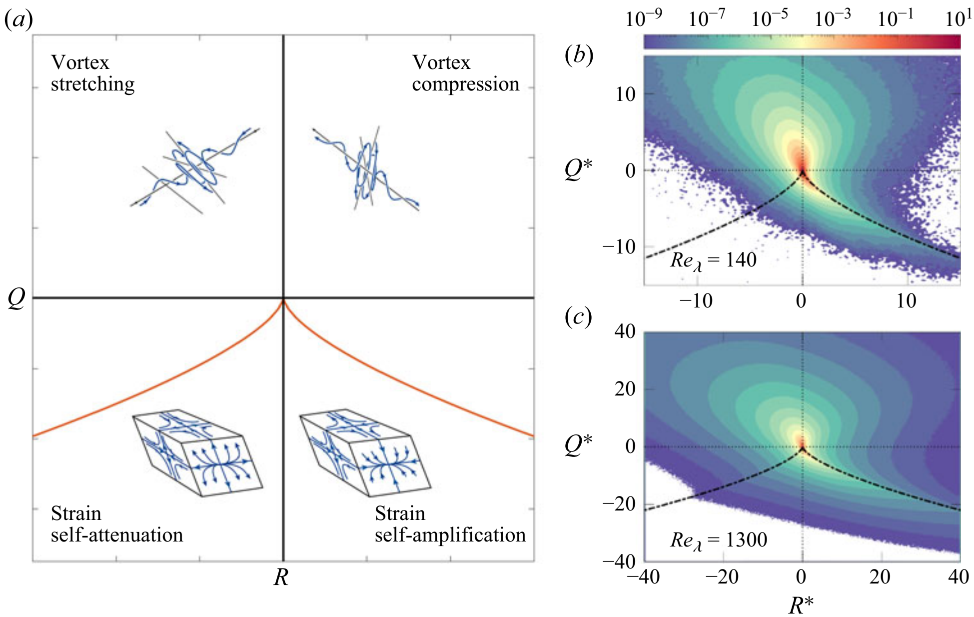

Figure 3. (a) Qualitative description of the local flow topology in the Q-R plane. The joint PDF of R and Q (non-dimensionalised using the Kolmogorov time scale) from DNS of isotropic turbulence at (b) $Re_\lambda = 140$ and (c) $Re_\lambda = 1300$ as adapted from Buaria & Sreenivasan (2023a).

trace-free tensors would yield a symmetric distribution with respect to R, turbulent flows exhibit a characteristic asymmetry in the Q-R plane. This is illustrated in figure 3. Panel (a) presents a qualitative picture of how the quadrants of the Q-R plane characterise the local flow topology (Cantwell 1992). Furthermore, panels b–c show the joint probability density function (PDF) from simulations at two different Reynolds numbers, revealing the well-known inverted tear-drop shape corresponding to preferential organisation of gradients associated with amplification of vorticity and strain, and also their intermittent nature, which is more formally explored in later sections.

While the Q-R representation has been often utilised in the literature to study and model gradient dynamics, it can also present substantial ambiguity when focusing on intense gradients as necessary for intermittency. For instance, events with large positive Q as visible in figure 3(b–c) point to intense vorticity, consistent with observations in figure 2. However, $Q \approx 0$ only suggests a mutual cancellation between vorticity and strain, irrespective of their individual intensities. To avoid this ambiguity, we will not rely on the Q-R plane to analyse the flow topology, but rather directly consider events of intense vorticity and strain as identified by their square norms defined in (2.7). Nevertheless, we refer interested readers to previous reviews by Wallace & Vukoslavčević (2010) and Meneveau (2011) and references therein for an exposition of the gradient dynamics in the Q-R plane.

2.3. *Singularities and turbulence*

The presence of nonlinear amplification mechanisms in the INSE naturally leads to a fundamental question: Is the growth of gradients bounded, or can they grow unbounded, leading to a finite-time singularity? In fact, whether solutions to the INSE with smooth initial conditions remain smooth for all times or whether a finite-time singularity appears remains one of the outstanding open mathematical problems, as recognised by the Clay Mathematical Institute (Fefferman 2006). It is in a way surprising that this question remains unanswered, since the INSE have been known for more than two centuries. So far, detailed comparisons between the experimental results and DNS suggest that the INSE accurately describe turbulent flows.

Simply formulated, the regularity (or smoothness) of a velocity field, $\boldsymbol{u}$, refers to the existence of a sufficiently large number of derivatives. Leray (1934) established the first essential results about the regularity of solutions of the INSE, and proved the existence of smooth solutions of the Navier–Stokes equations when the viscosity is large enough, using boundary conditions in a finite box without walls. Although he could not rule out that some solutions of the initial value problem could lose their regularity in a finite time, t^* when the viscosity ν becomes very small, Leray (1934) established that the loss of regularity manifests itself by the growth of the velocity gradients $\boldsymbol{A}$. However, it remains unclear whether the observation of strong gradients in turbulent flows has any relation to potential singularities; but the related underlying mathematical challenges provide a further motivation to study the amplification of velocity gradients.

Along with the inequality proving that a singularity must lead to an infinite amplification of the velocity gradients, Leray (1934) also showed that even the velocity of a singular solution of the INSE must also diverge at time t^*, i.e. the infinity norm of velocity also blows up. Clearly, any kind of divergence would question the validity of the INSE as a physical model of turbulence. However, the available numerical or experimental data for incompressible turbulence do not provide any evidence for the appearance of particularly large velocity fluctuations (remaining significantly smaller compared with the speed of sound, and also precluding compressibility effects). This casts a doubt on the existence of possible singular solutions of the INSE, at least over the range of Reynolds numbers available so far. In this article, we will work under the assumption that the solutions to the INSE are smooth, with well-defined derivatives.

A related but different problem is the question of the regularity of solutions to the Euler equations, obtained by setting $\nu = 0$ in (1.1). The conceptually appealing result that the solutions of the Navier–Stokes equations tend to solutions of the Euler equations when $\nu \to 0$ has been established, under the condition that the solutions of the Euler equations remain regular enough, by Kato (1972). The rigorous results available for the Euler equations also point to the importance of gradient amplification: Beale, Kato & Majda (1984) showed that for a solution of the Euler equations, singular at t^*, the L_∞-norm of vorticity $||\omega||_{L^\infty}$ has to satisfy $\int^{t^*} ||\omega(t')||_{L^\infty} \mathrm{d}t' = \infty$. This relation emphasises the amplification of vorticity in any solution of the Euler equations. Subsequent work led to more precise necessary conditions for the development of singular solutions. In particular, Constantin, Fefferman & Majda (1996) established the importance of the strain generated locally, based on the Biot–Savart formulation, an aspect we will return to in § 8. Only recently has Luo & Hou (2014) shown that singular solutions of the Euler equations appear in an axisymmetric configuration, close to the wall of a cylinder. However, given its essential dependence on the presence of a wall, its general relevance to turbulent flows remains unclear (Eyink 2024).

To summarise, the question of gradient amplification is at the heart of the search for singularities of the INSE equations. As such, turbulence studies would greatly benefit from a better mathematical understanding of the amplification and possibly of the saturation of velocity gradients in high-Reynolds-number flows. However, the relevance of the mathematical results obtained so far to turbulence remains unclear. Finally, we note that the concept of singularity in the context of turbulence is often discussed in relation to the approach originally proposed by Onsager (1949), in order to explain the dissipation anomaly in terms of local Hölder exponents $\leqslant 1/3$. We refer interested readers to the two recent perspective articles by Dubrulle (2019) and Eyink (2024).

3. Kolmogorov (1941) phenomenology

The previous section highlighted how dissipation anomaly naturally establishes a scale range in turbulence. Building upon this observation, Kolmogorov (1941) introduced a phenomenological approach to characterise the statistical structure of turbulence, which has since become the bedrock of modern turbulence theory. While his seminal work, commonly referred to as K41, is a staple of every turbulence textbook, we revisit it in this section with particular attention to aspects pertinent to velocity gradients that are less often emphasised.

3.1. *Kolmogorov (1941): background*

The central idea in K41 is that of the energy cascade and the emergence of universality at small scales. Kolmogorov postulated that turbulence sustains a dynamic equilibrium across scales, whereby energy is injected at large scales, transferred progressively to smaller scales (like a cascade), and ultimately gets dissipated into heat by viscosity at the smallest scales. Given the differing boundary conditions, geometries and forcing mechanisms between different turbulent flows, one expects the large scales to be inherently anisotropic and non-universal. However, Kolmogorov hypothesised that, as energy cascades to smaller scales, the influence of these large scales diminishes, and the small scales become increasingly isotropic (also termed 'locally isotropic') and universal, plausibly independent of the flow configuration. This idea forms the core of K41 phenomenology, endowing a special status on small scales, and enabling a major simplification Indeed, the K41 theory points to a general flow-independent description, which in itself is a major conceptual leap forward. Evidently, for small-scale isotropy to emerge, a large enough scale separation is necessary, which is equivalent to saying that *Re* must be sufficiently large (since the scale range increases with *Re*).

Kolmogorov (1941) goes further to quantify the small scales by assuming that the energy cascade is fully characterised by the mean dissipation rate $\langle \epsilon \rangle$. Since $\langle \epsilon \rangle$ remains finite and independent of viscosity at high *Re*, Kolmogorov postulated that small scales of turbulence can be uniquely prescribed by only ν and $\langle \epsilon \rangle$. From dimensional analysis, one can define the following characteristic scales, now known as the Kolmogorov scales

$$\eta_K = (\nu^3/\langle \epsilon \rangle)^{1/4}, \qquad \tau_K = (\nu/\langle \epsilon \rangle)^{1/2}, \qquad u_K = (\nu \langle \epsilon \rangle)^{1/4}, \tag{3.1}$$

respectively for length, time and velocity. Thus, K41 postulates that any statistical quantity characterising the small scales, when appropriately non-dimensionalised by the Kolmogorov scales, behaves universally. Using dissipation anomaly $\langle \epsilon \rangle \sim U^3/L$, one can obtain the ratios of Kolmogorov scales to the corresponding large scales, which turn out to be

$$\frac{L}{\eta_K} \sim Re^{3/4}, \qquad \frac{T_E}{\tau_K} \sim Re^{1/2}, \qquad \frac{U}{u_K} \sim Re^{1/4}, \tag{3.2}$$

where $T_E = L/U$ is the large-eddy time scale. The above relations also illustrate how the range of scales increases with Reynolds number.

3.2. *Velocity increments and gradients*

To analyse the implications of K41, we first consider the longitudinal velocity increment

$$\delta u_r = u_\alpha(x_\alpha + r) - u_\alpha(x_\alpha), \tag{3.3}$$

where the velocity component u_α and the separation distance r are both along x_α. The quantity δu_r essentially represents a coarse-grained gradient over a scale r, and can be related to energy transfer and flow structures at that scale. We will soon generalise the formalism to transverse increments and the velocity-gradient tensor.

The statistical behaviour of δu_r can be characterised by its distribution, or by its moments $S_n \equiv \langle (\delta u_r)^n \rangle$, also known as structure functions. If the scale r is sufficiently small, i.e. $r \ll L$, so the hypothesis of universality holds, then it follows from K41 that

$$\langle (\delta u_r)^n \rangle = F_n(\langle \epsilon \rangle, \nu, r), \qquad r \ll L. \tag{3.4}$$

After non-dimensionalisation, the above relation can be restated more simply as

$$\langle (\delta u_r)^n \rangle / u_K^n = F_n(r/\eta_K), \qquad r \ll L, \tag{3.5}$$

where the functions $F_n(\cdot)$ are postulated to be universal. Note that more generally, a universal characteristic function can be constructed for the distribution of δu_r (Monin & Yaglom 1975). While K41 does not explicitly provide the functions $F_n(\cdot)$, they could be empirically obtained from data if universality indeed holds. Nevertheless, K41 provides its two limiting behaviours. The first is when $r \to 0$ (or more precisely, $r/\eta_K \to 0$, since η_K is the smallest possible scale in K41 theory), in which case $\delta u_r / r$ approaches the true gradient. In this limit, it follows from a Taylor-series expansion that $(\delta u_r)^n \sim (\partial_x u)^n r^n$, which leads to the result that velocity-gradient moments, when normalised by Kolmogorov scales, are universal constants. More formally, considering the longitudinal component $A_{\alpha\alpha} = \partial_\alpha u_\alpha$ (no summation implied) of the velocity-gradient tensor, K41 implies that the non-dimensional moments

$$M_n^L \equiv \langle A_{\alpha\alpha}^n \rangle \tau_K^n, \tag{3.6}$$

are universal constants. This is equivalent to stating that $F_n(x) \simeq M_n^L \; x^n$ for $x \to 0$ in (3.5).

The second limit is obtained by additionally considering $\eta_K \ll r \ll L$, i.e. r is in the intermediate range of scales far from both large scales and viscous scales – also called the inertial range (since inertial forces dominate in this range). This is the well-known second hypothesis of K41, which postulates that in the inertial range, the effects of viscosity can be ignored. From simple dimensional arguments it follows that

$$\langle (\delta u_r)^n \rangle = C_n (\langle \epsilon \rangle r)^{n/3}, \qquad \eta_K \ll r \ll L, \tag{3.7}$$

which is equivalent to stating that $F_n(x) \simeq C_n x^{n/3}$ for $x \to \infty$ in (3.5). Evidently, even larger scale separation, and hence higher *Re*, would be required to observe this limiting behaviour. For $n = 2$, the above result is equivalent to the well-known scaling relation for the turbulent energy spectrum, formally defined later in (3.17).

It is worth emphasising that the scaling relations in (3.7) and (3.17) rely solely on dimensional arguments and cannot be directly derived from governing equations, with a single exception. For $n = 3$, starting from the INSE, one can derive the Kármán–Howarth equation (von Kármán & Howarth 1938)

$$\frac{3}{r^5} \int_0^r r'^4 \frac{\partial S_2(r')}{\partial t} dr' - 6\nu \frac{\partial S_2}{\partial r} + S_3 = -\frac{4}{5} \langle \epsilon \rangle r. \tag{3.8}$$

The first two terms on the left-hand side can be argued to be negligible in the range $\eta_K \ll r \ll L$ and assuming statistical stationarity, lead to the result: $S_3 = -(4/5)\langle\epsilon\rangle r$, which exactly corresponds to (3.7) for $n = 3$ with $C_3 = -(4/5)$. Interestingly, this implies that the third moment is non-vanishing in the high *Re* limit (due to dissipation anomaly) and also negative, which establishes that the average flux of energy is always from large to small scales, in agreement with the cascade picture (Frisch 1995).

It is straightforward to extend the results discussed in § 3.2 to transverse increments, defined as

$$\delta v_r = u_\alpha(x_\beta + r) - u_\alpha(x_\beta), \tag{3.9}$$

where the separation distance r is orthogonal to direction of velocity component. Since K41 is based on scale similarity and dimensional analysis, the scaling predictions for δv_r are identical to those for δu_r. In the inertial range, for instance, one expects $(\delta v_r)^n \sim (\langle\epsilon\rangle r)^{n/3}$, albeit with different proportionality constants. However, there are no exact relations derived from the INSE which involve only transverse increments. The 4/5th law for longitudinal increments can be generalised to the 4/3rd and 4/15th laws, which provide a third-order moment relation involving both longitudinal and transverse increments (Duchon & Robert 2000; Eyink 2003). In fact, rotational symmetry implies that the odd moments of δv_r are zero. On the other hand, for the moments of the transverse velocity gradients: $A_{\alpha\beta} = \partial_\beta u_\alpha$ $(\alpha \neq \beta)$, K41 predicts that the non-dimensionalised moments

$$M_n^T \equiv \langle A_{\alpha\beta}^n \rangle \tau_K^n, \quad \alpha \neq \beta, \tag{3.10}$$

are universal constants, in analogy with the longitudinal case. In this case also, the odd moments would be zero from rotational symmetry.

3.3. *Generalised tensorial correlations*

Since K41 posits isotropy at small scales, the longitudinal and transverse components of both velocity increments and gradients can be further related to one another. More generally, one can consider all tensorial correlations and obtain scaling relations for them. This leads naturally to the study of higher-order tensors, such as the fourth- and sixth-order velocity-gradient tensors

$$M_{ijkl} = \langle A_{ij} A_{kl} \rangle \tau_K^2, \quad M_{ijklmn} = \langle A_{ij} A_{kl} A_{mn} \rangle \tau_K^3. \tag{3.11}$$

While K41 scaling predicts that all components of these tensors are universal constants, isotropy imposes even stronger constraints on the tensor structure. For example, the fourth-order tensor M_{ijkl}, can be expressed in terms of a single reference component, typically taken to be $M_{1111} = \langle A_{11}^2 \rangle \tau_K^2$, according to

$$M_{ijkl} = M_{1111} \left(-\frac{1}{2}\delta_{ij}\delta_{kl} + 2\delta_{ik}\delta_{jl} - \frac{1}{2}\delta_{il}\delta_{jk} \right). \tag{3.12}$$

Using the definition of τ_K, a straightforward calculation gives $M_2^L = (1/2)M_2^T = M_{1111} = (1/15)$.

For the sixth-order tensor, a single component, $\langle A_{11}^3 \rangle \tau_K^3$, suffices to characterise the entire tensor under isotropy. This is the skewness of longitudinal gradients (up to a constant prefactor) and is known to be negative, similar to the skewness of velocity increments (see (3.8)). The expression of the sixth-order tensor additionally gives the relation for the two invariants $\langle \omega_i S_{ij} \omega_j \rangle$ and $\langle S_{ij} S_{ij} S_{ki} \rangle$ (Betchov 1956; Pope 2000)

$$\langle \omega_i \omega_j S_{ij} \rangle = -\frac{4}{3} \langle S_{ij} S_{ij} S_{ki} \rangle = -\frac{35}{2} \langle A_{11}^3 \rangle, \tag{3.13}$$

revealing the connection between gradient amplification and energy cascade.

In contrast, the expression of the eighth-order tensor corresponding to the fourth-order gradient moments requires four reference components (Siggia 1981)

$$F_1 = \langle A_{11}^4 \rangle, \quad F_2 = \langle A_{11}^2 A_{21}^2 \rangle, \quad F_3 = \langle A_{21}^4 \rangle, \quad F_4 = \langle A_{11}^2 A_{23}^2 \rangle, \tag{3.14}$$

where F_1 and F_3 respectively correspond to the flatness of longitudinal and transverse gradients. As shown in Siggia (1981), the four invariants can also be written in terms of strain and vorticity

$$I_1 = \frac{1}{4}\langle \Sigma^2 \rangle, \quad I_2 = \frac{1}{2}\langle \Sigma \Omega \rangle, \quad I_3 = \langle W_i W_i \rangle, \quad I_4 = \langle \Omega^2 \rangle, \tag{3.15}$$

where Σ and Ω are the square norms of strain and vorticity, defined earlier in (2.7) and $W_i = \omega_j S_{ij}$ is the vortex stretching vector. We will return to these quantities later in § 5, when the scaling of gradient moments is rigorously investigated.

Similar analysis can be performed by considering generalised tensors obtained from velocity increments. However, deriving isotropic relations for them is more involved as one also needs to factor in the dependence on scale size. We refer the reader to Monin & Yaglom (1975) and Pope (2000) for a detailed exposition. Here, we briefly discuss only the structure of the energy spectrum. In general, one can consider the velocity spectrum tensor $E_{ij}(\boldsymbol{k})$ defined by the Fourier transform of the two point correlation $R_{ij}(\boldsymbol{r}) = \langle u_i(\boldsymbol{x}) u_j(\boldsymbol{x}+\boldsymbol{r})\rangle$. Isotropy implies that $E_{ij}(\boldsymbol{k})$ can be expressed in terms of the energy spectrum $E(k)$ as

$$E_{ij}(\boldsymbol{k}) = \frac{E(k)}{4\pi k^2}\left(\delta_{ij} - \frac{k_i k_j}{k^2}\right) \ : \quad \langle u_i u_j \rangle = \int_{\boldsymbol{k}} E_{ij}(\boldsymbol{k}) \mathrm{d}\boldsymbol{k}, \tag{3.16}$$

where $\boldsymbol{k}$ is the wave vector and $k = |\boldsymbol{k}|$ is the wavenumber. It is easy to show the turbulent kinetic energy $(1/2)\langle u_i u_i \rangle = \int_0^\infty E(k)\mathrm{d}k$ (note that $\mathrm{d}\boldsymbol{k} = 4\pi k^2 \mathrm{d}k$). Finally, application of K41 scaling arguments in the inertial range leads to the well-known result

$$E(k) = C\langle \epsilon \rangle^{2/3} k^{-5/3}, \quad 1/L \ll k \ll 1/\eta_K. \tag{3.17}$$

3.4. *Kolmogorov (1941): successes and shortcomings*

3.4.1. *Energy spectrum*

Arguably the most celebrated confirmation of K41 comes from the scaling of the energy spectrum as predicted by (3.17). While DNS can provide the full 3-D spectrum, experiments often only provide the 1-D surrogate: $E_{11}(k_1)$ corresponding to the downstream velocity component u_1. Using (3.16) it is easy to show that $\langle u_1^2 \rangle = \int E_{11}(k_1)\mathrm{d}k_1$. It is easy to deduce that both 1-D and 3-D spectra share the same scaling exponent in the inertial range, which K41 predicts to be $-5/3$. Note that the presence of an inertial range requires high *Re*. As a result, earlier tests of K41 predominantly relied on 1-D surrogates measured in experiments, with high *Re* DNS data only becoming available more recently. Figure 4 shows a compilation of the 1-D spectra (non-dimensionalised by Kolmogorov variables) from experiments and DNS. The details pertaining to the data are provided later in § 4. Two observations stand out: (i) collapse of various spectra for higher wavenumbers, corresponding to scales smaller than the large scale; (ii) emergence and broadening of a $k^{-5/3}$ scaling at intermediate wavenumbers with increasing Reynolds number – both in remarkable agreement with K41 predictions. In addition to the 1-D spectrum $E_{11}(k_1)$, experiments have also measured other surrogates such as $E_{22}(k_1)$ and $E_{33}(k_1)$ (Saddhoughi & Veeravalli 1994), and more recently the full 3-D spectrum (Dubrulle 2019). In all cases, the results are broadly consistent with the $-5/3$ scaling.

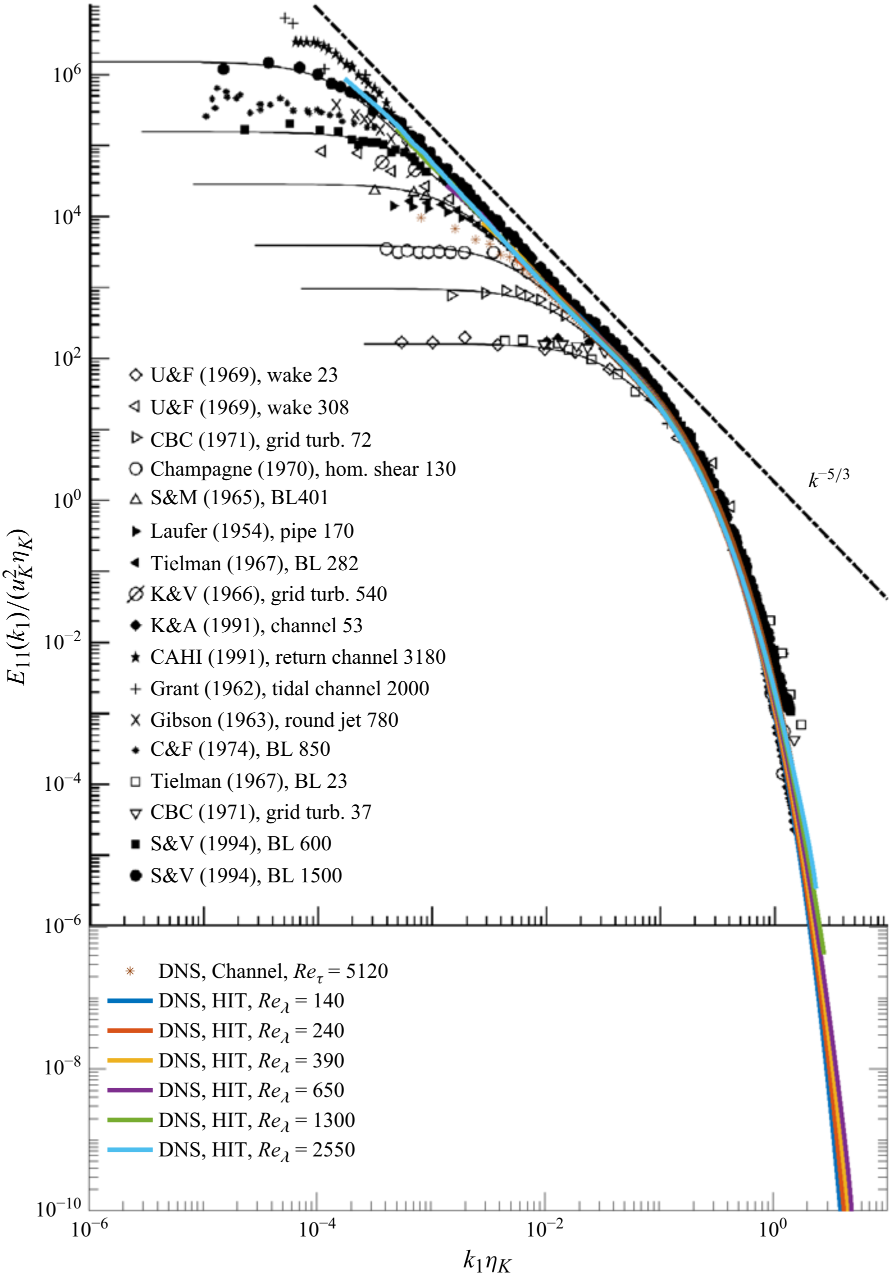

Figure 4. The one-dimensional energy spectrum $E_{11}(k_1)$, non-dimensionalised by Kolmogorov scales. The symbols in black correspond to experimental data as adapted from figure 6.14 of Pope (2000). The spectra from DNS are superposed on top, corresponding to isotropic turbulence over the range $140 \leqslant Re_\lambda \leqslant 1300$ (table 1) and $Re_\lambda = 2550$ (Yeung *et al.* 2025), and channel flow at $Re_\tau = 5200$ (Lee & Moser 2015), taken from the centre of the channel. The spectra for latter two are obtained from the Johns Hopkins turbulence database (Graham *et al.* 2016).

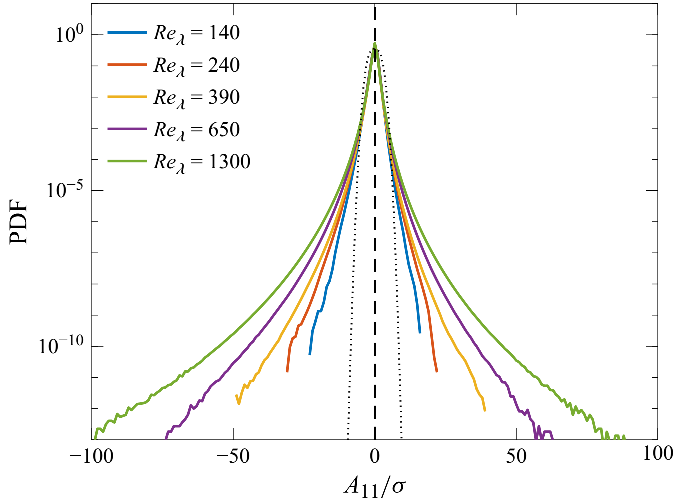

Figure 5. The PDF of the longitudinal velocity gradients, $A_{11} = \partial u_1/\partial x_1$, normalised by its r.m.s., $\sigma = \langle A_{11}^2 \rangle^{1/2}$ for the DNS runs listed in table 1. The dotted line corresponds to a standard Gaussian distribution.

3.4.2. *Intermittency and velocity gradients*

Given the success of K41 in predicting the energy spectrum, it is natural to investigate its implications for other statistical quantities. In this regard, we consider the statistics of velocity gradients and increments, as introduced earlier. Considering first the velocity gradients, K41 predicts that all non-dimensional moments as defined earlier are universal constants. Since these moments are non-dimensionalised using Kolmogorov time scale, which itself is defined from the variance of velocity gradients, it follows that K41 predicts a universal functional form for the standardised distribution of velocity gradients. Figure 5 shows the standardised PDF of the longitudinal component $A_{\alpha\alpha}$ for various Reynolds numbers. The data are obtained from DNS of isotropic turbulence (as outlined in § 4). Note that $\langle A_{ij} \rangle = 0$ by design and σ is the standard deviation satisfying $\sigma \tau_K = (1/\sqrt{15})$. According to K41, these PDFs should collapse onto a single curve (possibly Gaussian – shown as a dotted curve in figure 5 for reference). However, this prediction is clearly violated. The PDFs not only fail to collapse, but also exhibit long tails which strongly deviate from Gaussian behaviour. Moreover, with increasing Reynolds number, the tails become broader, indicating that extreme events become increasingly frequent.

The observation in figure 5 corresponds to the phenomena of small-scale intermittency, often also referred to as internal intermittency or simply intermittency. It loosely refers to the formation of rare and intense velocity gradients which fundamentally defy a mean-field description, such as that proposed by K41. In a mean-field framework, the entire distribution of a random variable is solely described by its mean amplitude, typically resulting in Gaussian statistics. The fat-tailed PDFs seen here clearly invalidate such a description. It is worth clarifying that development of stronger gradients with increasing Reynolds numbers is inherently expected due to dissipation anomaly. However, figure 5 shows that the intense gradients observed in turbulent flows are far stronger than predicted by dissipation anomaly alone. This behaviour lies at the heart of intermittency: the realisation that small scales of turbulence cannot be characterised by the mean dissipation rate alone, as assumed by K41. Instead, it requires a full spectrum of singularities, forming the basis for multifractality (which is formally discussed in § 5).

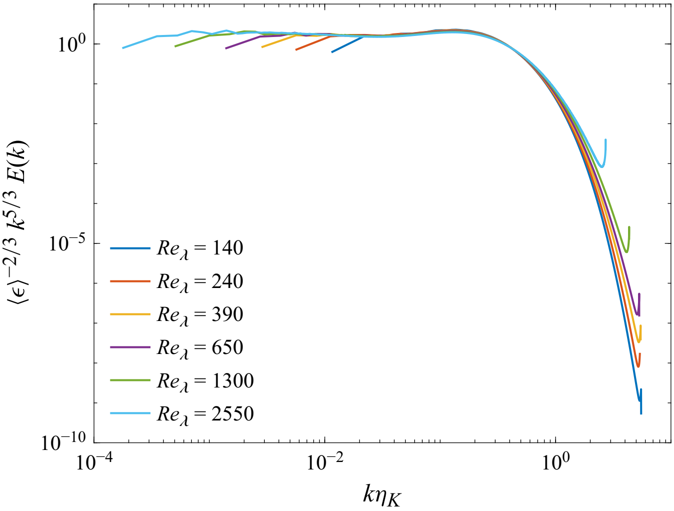

Figure 6. Compensated 3-D energy spectrum $E(k)$ from DNS of isotropic turbulence, at various Taylor-scale Reynolds numbers, Re_λ. The figure is adapted from Buaria & Sreenivasan (2020), with $Re_\lambda = 2550$ data added from the Johns Hopkins turbulence database.

Since the result in figure 5 clearly invalidates K41, one might wonder why K41 remains successful for the energy spectrum. The resolution to this apparent paradox lies in the fact that the energy spectrum reflects only the second moment of velocity differences. When considering second moments of velocity gradients, K41 predictions are also quite accurate. In fact, the definition of the Kolmogorov time scale ensures that the second moment of the velocity gradients aligns exactly with K41. Consequently, while K41 fails to capture the full distribution and extreme events of velocity gradients, it is still able to approximately represent the average energetics of turbulence.

To understand how K41 fails systematically, it is instructive to examine higher-order moments, which are increasingly sensitive to the extreme events in the PDF tails. As figure 5 indicates, higher-order moments of gradients exhibit strong Reynolds-number dependence (which we formally quantify in § 5). Hence, the effects of intermittency are weak on low-order statistics, but dominate higher-order statistics. Nevertheless, even the weak influence of intermittency on low-order statistics can be revealed, including the energy spectrum. Figure 6 shows the compensated 3-D energy spectra from DNS (Buaria & Sreenivasan 2020), where scales smaller than the Kolmogorov length scale are resolved. It can be observed that for $k\eta_K \geqslant 1$, the spectra do not actually collapse as hypothesised by K41. Such deviations have also been confirmed in experiments (Gorbunova *et al.* 2020). In fact, a closer inspection of the inertial range at high Reynolds numbers in DNS shows subtle deviations even from the $-5/3$ scaling in the inertial range (Ishihara *et al.* 2016).

3.4.3. *Structure functions*

Much like velocity gradients, velocity increments also reveal a strong influence of intermittency. In fact, velocity increments and structure functions have historically received more attention (Sreenivasan & Antonia 1997), as direct measurement of velocity gradients has always been very challenging in experiments; whereas DNS were early on restricted to low *Re*, precluding a clear inertial range. In recent years, however, DNS at high *Re* have become feasible, allowing precise determinations of high-order structure functions and their scaling exponents (Iyer, Sreenivasan & Yeung 2020; Buaria & Sreenivasan

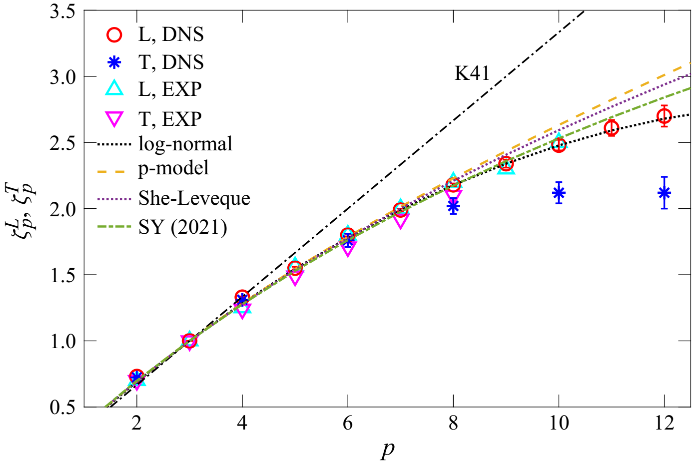

Figure 7. Scaling exponents of the structure functions, with L and T corresponding to longitudinal and transverse, respectively. The DNS data are from Iyer *et al.* (2020) and Buaria & Sreenivasan (2023*c*) and experimental data are from Sreenivasan & Antonia (1997), Dhruva *et al.* (1997) and Shen & Warhaft (2002). The data are compared with various theoretical predictions as indicated in the legend and also listed in table 2 in § 5.1. The longitudinal scaling exponents are seemingly best described by the log-normal model with intermittency exponent $\mu \approx 0.22$ (Buaria & Sreenivasan 2022*a*). The transverse exponents appear to saturate to a value close to 2.

2023*c*). Given their extensive treatment in the literature, we summarise here the key results most relevant to our discussion.

Recasting the notation used earlier, one can generally state that the structure functions follow a power-law scaling in the inertial range

$$S_p \equiv \langle (\delta u_r)^p \rangle \sim r^{\zeta_p}, \quad \eta_K \ll r \ll L, \tag{3.18}$$

with the K41 result given as $\zeta_p^{\mathrm{K41}} = p/3$. Analogous relations hold for transverse structure functions, so we differentiate the scaling exponents as ζ_p^L for longitudinal and ζ_p^{T} for transverse directions. Figure 7 shows the compilation of results from recent DNS (Iyer *et al.* 2020; Buaria & Sreenivasan 2023*c*) and classical wind-tunnel experiments at high *Re* (Sreenivasan & Antonia 1997; Dhruva, Tsuji & Sreenivasan 1997; Shen & Warhaft 2002).

Consistent with previous discussion, we notice that for smaller values of p, the exponents for low-order structure functions are in nominal agreement with the K41 prediction (with the result $\zeta_p^L = 1$ for $p = 3$ being exact). However, increasing deviations are visible at higher moment orders. In addition to the K41 prediction, figure 7 also includes predictions from several intermittency models that provide improved fits to the longitudinal exponents; these will be formally discussed in § 5. An important feature revealed by the data is the difference between longitudinal and transverse exponents. While both coincide at low orders, the transverse exponents show stronger departures from K41 at higher p, and remarkably appear to saturate beyond $p \geqslant 10$. Importantly, this asymmetry is not accounted for by prevailing intermittency models and remains an open problem. This will also be discussed in § 5.

4. A note on DNS

Before delving deeper into intermittency and dynamics of turbulence, a brief exposition of DNS is in order. As the name suggests, DNS refers to the direct computation of solutions of the INSE by explicitly resolving all dynamically relevant scales of motion. The simulation domain must therefore encompass the largest flow structures while the computational grid must be fine enough to capture the smallest scales of motion. When properly resolved, DNS provides an exact numerical representation of turbulence, giving complete access to the full 3-D velocity field $\boldsymbol{u}(\boldsymbol{x}, t)$, and enabling the computation of any desired flow property without any modelling assumption.

To quantify the turbulence intensity in DNS, as also done in classical grid turbulence experiments, it is customary to use the Taylor-scale Reynolds number, Re_λ, based on the Taylor length scale, λ. The corresponding quantities, which are also accessible via hot-wire measurements, are defined by

$$Re_\lambda = \frac{U\lambda}{\nu}, \quad \text{where} \quad \lambda = \left(\frac{U^2}{\langle A_{11}^2 \rangle} \right)^{1/2}, \tag{4.1}$$

where U represents the r.m.s. of velocity. Taking into account the dissipation anomaly, one finds, in homogeneous isotropic turbulence, that Re and Re_λ are related by: $Re_\lambda = (15 C_\epsilon Re)^{1/2}$ (Pope 2000), where $C_\epsilon = \langle \epsilon \rangle L/U^3 \approx 0.43$ as shown in figure 1.

However, the conceptual simplicity and unprecedented utility of DNS come with a high computational cost. The standard practice is to simulate the INSE with a fixed geometry, in a system of size L_0, with a large-scale velocity U, and to increase the Reynolds number by numerically decreasing viscosity ν. Assuming K41 phenomenology, the range of scales in a turbulent flow is given by $L/\eta_K \sim Re^{3/4}$, see (3.2). Taking the simulation domain to be L_0 and grid spacing to be Δx, it follows that the number of grid points in one spatial direction is $N = L_0/\Delta x \sim Re^{3/4}$. Thus, for a full 3-D simulation, the total number of grid points scales as $N^3 \sim Re^{9/4}$.

On the other hand, the time step size Δt in simulations is set by stability constraints, typically the Courant–Friedrichs–Lewy (CFL) condition, which requires $\Delta t \leqslant C \, \Delta x/||\boldsymbol{u}||_\infty$. The length of the simulation must be long enough to capture at least one large-eddy-turnover time $T_E = L/U$, which gives the total number of time steps $N_t \sim T_E/\Delta t$. It is easy to show that, in the standard set-up considered, $N_t \sim N$, resulting in a total computational cost of $N^4 \sim Re^3$. Note that the computational cost of DNS is slightly higher than the physical range of scales given by $(L/\eta_K)^3 \times (T_E/\tau_K) \sim Re^{11/4}$ (Pope 2000); evidently, this is due to the stability criteria just discussed.

The cost of DNS increases even further when additional physics, such as particles, scalars, are also included. Consequently, high Re encountered in nature and engineering, often of the order $\mathcal{O}(10^8)$ or higher, are far beyond the reach of present-day DNS capabilities. Instead, the practice is to perform DNS of idealised, canonical flows that serve as testbeds to analyse fundamental physics, validate theories and develop turbulence models for complex flows at higher Re (Moin & Mahesh 1998). Given the diversity in how turbulence can be generated, several canonical set-ups exist, primarily differing in their boundary conditions and the large-scale forcing mechanisms to sustain turbulence, see, e.g. Kim & Leonard (2024).

In principle, one needs to investigate the turbulent small scales for each individual flow condition, as different configurations emphasise different physical mechanisms. In this context, establishing the universality of the small-scale properties is a major stake, as it would imply a statistical description, independent of the specificity of the flow. It is also easy to reason that universality necessitates local isotropy at small scales, since any persistent anisotropy would be flow specific. For this reason, the canonical set-up of homogeneous isotropic turbulence (HIT) provides the simplest and best configuration to study the small scales. In DNS, HIT is simulated in a triply periodic domain, in the absence of any solid boundaries and shear. An isotropic large-scale forcing is applied at the lowest wavenumber to sustain a statistically stationary state. This allows one to generate turbulence which is isotropic at large scales (on average), in turn also realising a very high degree of isotropy at small scales – making it ideal for testing theoretical predictions and analysing intermittency. In this article, we will predominantly rely on data from DNS of HIT, but often compare it with data from DNS of other flows and also laboratory experiments (as done earlier in § 3).

4.1. *Intermittency and resolution requirements*

The classical estimate that the computational cost of DNS scales as Re^3 relies on K41 phenomenology, where the smallest scale in the flow is given by η_K, defined from the mean dissipation rate, see § 3 However, as we saw in § 3.4.2, intermittency implies that fluctuations of dissipation rate and gradients can be far more intense, suggesting the existence of dynamically relevant scales smaller than η_K (Paladin & Vulpiani 1987). Accordingly, a reliable DNS requires a finer grid resolution, resolving dynamically active scales $\eta_{min} < \eta_K$ in the flow. Unfortunately, this presents a challenging situation, as directly assessing η_{min} (or validating any theoretical prediction for it) requires accurate DNS data, but such an accurate DNS itself requires an *a priori* knowledge of η_{min}. Note that if η_{min} is appropriately resolved in DNS, then the CFL stability criterion automatically ensures that the smallest time scale is also resolved. Note that the challenge of resolving scales even smaller than η_K is even more demanding in experiments, since the measurement resolution at high Reynolds numbers falls substantially short of resolving η_K, let alone even smaller scales.

A pragmatic solution is to perform DNS at a given Re by resolving η_K and then to progressively refine the grid resolution until the statistics of relevant quantities become independent of further grid refinements. This approach is well known in the computational fluid dynamics community and has also been employed in turbulence simulations (Jiménez *et al.* 1993; Yeung, Sreenivasan & Pope 2018). Despite its apparent simplicity, this strategy remains challenging, as the most extreme events corresponding to the smallest scales are also very rare, and obtaining converged statistics also requires a large number of samples. We used the procedure outlined above to construct the DNS database discussed in the following subsection; but more information on convergence tests can be found in Yeung *et al.* (2018) and Buaria *et al.* (2020*a*,*b*).

The precise analysis to identify the smallest scales is discussed in § 6. However, we briefly introduce the relation connecting resolution and Reynolds number with the number of grid points, which will be helpful in better understanding the database presented in § 4.3. Following the string of arguments at the beginning of this section, we relate the number of grid points, N, to the size L_0 of the domain and to the grid spacing, Δx, via: $N = L_0/\Delta x \sim L/\Delta x$, which expresses that the computational domain must capture the largest flow length scale. With simple rearrangement, we get

$$N \sim \left(\frac{\Delta x}{\eta_K}\right)^{-1} Re^{3/4} \sim \left(\frac{\Delta x}{\eta_K}\right)^{-1} Re_\lambda^{3/2}, \tag{4.2}$$

where $\Delta x/\eta_K$ measures the small-scale resolution in DNS. When resolving η_K as suggested by K41 phenomenology, it is sufficient to keep this ratio fixed as Reynolds number increases. However, due to intermittency, $\Delta x/\eta_K$ has to depend on the Reynolds number, with the expectation that it must decreased with Re. Taking $\Delta x/\eta_K \sim Re_\lambda^{-\alpha}$, it follows that

$$N \sim Re^{3/4+\alpha/2} \sim Re_\lambda^{3/2+\alpha}, \tag{4.3}$$

meaning the total cost of DNS actually scales as $N^4 \sim Re_\lambda^{6+4\alpha} \sim Re^{3+2\alpha}$. A formal analysis to quantify this exponent α is presented in § 6, but it is evident that an accurate DNS to study intermittency is in fact even more expensive than expected from the use of K41 phenomenology.

4.2. *Statistical convergence and simulation length*

An important consideration for DNS and experiments alike is that of statistical convergence, particularly when investigating rare and extreme events, as required for studying intermittency. In DNS of HIT, since the flow is both statistically homogeneous and stationary, statistics are obtained by first averaging over the entire domain at a given instant (or a single snapshot) and subsequently averaging over multiple snapshots taken at different times. Care must be taken, however, to ensure that the snapshots are sufficiently separated in time so that they are statistically independent. Thus, the question of statistical convergence is tied to the total length of the simulation.

The simulation time is typically prescribed in terms of the large-eddy-turnover time T_E, which essentially characterises the decorrelation time of the largest eddies. The standard prescription is to perform a simulation spanning several eddy-turnover times. The simulations considered here largely adhere to this. Although for the largest grid sizes, the enormous computing cost can limit the total simulation time. However, this is not an issue in the present context, since our focus is on the small scales, which decorrelate on much faster time scales. Thus, their statistics can be accrued by averaging snapshots more frequently in time. In fact, for velocity gradients, the decorrelation time is governed by τ_K, which becomes progressively smaller compared with T_E as Reynolds number increases. Likewise, the characteristic length scale of spatial gradients is governed by η_K, which becomes increasingly smaller compared with L as the Reynolds number increases, implying that even a spatial average over one snapshot provides a larger number of statistically independent events.

The precise details regarding grid resolution and simulation lengths are summarised in the next subsection. Nevertheless, it is worth emphasising that, for all the results reported here, we have carefully established convergence with respect to both grid resolution and statistical sampling. In practice, this is verified by ensuring that the PDF $P(s)$ for a fluctuating quantity s remains unchanged with respect to improvements in grid resolution and sampling. Particular attention is paid to the convergence of higher-order moments $\langle s^n \rangle$, which are especially sensitive to rare and extreme events. Since these moments can be expressed as $\langle s^n \rangle = \int s^n \, P(s) \, \mathrm{d}s$, their accurate determination requires that the tails of integrand $s^n \, P(s)$ decay sufficiently as $|s|$ increases (such that the integral converges). All the results presented here have been verified to satisfy these convergence criteria. However, to keep the focus on the physical interpretation of the results, we do not reproduce the detailed convergence analyses here, but they can often be found in the prior studies where the results were originally reported.

4.3. *Direct numerical simulation database*

As mentioned previously, our analysis relies primarily on data from DNS of HIT. This allows us to use spectral methods based on a decomposition in Fourier modes, which is a particularly attractive choice for spatial discretisation. In the Fourier spectral method, the velocity and other relevant fields are represented as sums of discrete Fourier modes,

Re_λ	N^3	$k_{max}\eta$	T_E/τ_K	T_{sim}	N_s
140	1024^3	5.82	16.0	6.5 T_E	24
240	2048^3	5.70	30.3	6.0 T_E	24
390	4096^3	5.81	48.4	2.8 T_E	35
650	8192^3	5.65	74.4	2.0 T_E	40
1300	8192^3	1.95	147.4	4.0 T_E	—
1300	12288^3	2.95	147.4	20 τ_K	18

Table 1. Simulation parameters for the DNS runs used in the current work: the Taylor-scale Reynolds number (Re_λ), the number of grid points (N^3), spatial resolution ($k_{max}\eta$), ratio of large-eddy-turnover time (T_E) to Kolmogorov time scale (τ_K), length of simulation (T_{sim}) in statistically stationary state and the number of instantaneous snapshots (N_s) used for each run to obtain the statistics.

allowing one to utilise the exact differentiation properties of the Fourier basis. This allows one to compute the spatial derivative with unparalleled spectral accuracy, with the discretisation error decreasing exponentially with grid spacing (Orszag & Patterson 1972). The nonlinear terms are evaluated in physical space using a pseudospectral approach, with aliasing errors controlled by a combination of truncation and grid shifting (Patterson & Orszag 1971; Rogallo 1981). The resolution in spectral DNS is naturally expressed in terms of the maximum resolved wavenumber k_{max}, which is related to grid spacing as $k_{max} = 2\pi\sqrt{2}N/(3L_0) \approx 3/\Delta x$. It is typical to set $L_0 = 2\pi$ in DNS of HIT giving $k_{max} = \sqrt{2}N/3$. Thus, the small-scale resolution in HIT is also given by $k_{max}\eta_K$, with $\Delta x/\eta_K = 3/(k_{max}\eta_K)$. Thus, the grid size can be expressed as

$$N = const.\, (k_{max}\ \eta_K)\, Re_\lambda^{3/2}. \tag{4.4}$$

Historically, HIT simulations were performed with $k_{max}\eta_K = 1{-}1.5$, occasionally going up to $k_{max}\eta_K = 2$ (Jiménez *et al.* 1993; Gotoh, Fukayama & Nakano 2002; Ishihara *et al.* 2007). Such values correspond to $\Delta x/\eta_K > 1$, barely resolving even the Kolmogorov scale. The HIT database used here, summarised in table 1, adopts substantially higher resolution: for $Re_\lambda = 140$ to 650, we maintain an unprecedented resolution of $k_{max}\eta_K \approx 6$, whereas for $Re_\lambda = 1300$ the resolution is $k_{max}\eta_K \approx 3$. For $Re_\lambda \leqslant 650$, the runs span a few eddy-turnover times in the statistically stationary state. However, the run at $Re_\lambda = 1300$ is necessarily shorter due to the high computational cost. As noted earlier, this is not an issue when studying intermittency, as velocity increments and gradients decorrelate on a much shorter time scale than T_E, and more so when their extreme events are considered. We further note that the listed $Re_\lambda = 1300$ run was extended from a simulation of $Re_\lambda = 1300$ at 8192^3 with $k_{max}\eta_K \approx 2$ (Buaria & Sreenivasan 2023*c*; Iyer *et al.* 2020), which spans a few eddy-turnover times in the stationary state. Essentially, for all the runs listed in table 1, we have convincingly established convergence with respect to both resolution and statistical sampling, as supported by analyses and comparisons (with past results) in several recent works, see e.g. Buaria *et al.* (2019, 2020*a*), Buaria & Pumir (2022) and Buaria & Sreenivasan (2023*c*) and references therein.

To complement these data, we also analyse turbulent plane channel flow DNS from the Johns Hopkins Turbulence Database, corresponding to $Re_\tau = 1000$ and 5200 (Lee & Moser 2015; Graham *et al.* 2016). For comparison with HIT, we only analyse velocity-gradient statistics near the channel centre (far from wall effects). However, when it comes to small-scale resolution, these simulations are not that well resolved in the streamwise direction, with $\Delta x/\eta_K = 2.2$ and 1.5 (corresponding to $k_{max}\eta_K \approx 1.4$ and 2) for $Re_\tau = 1000$ and 5200, respectively, although resolution in the wall-normal and spanwise directions is slightly better (Buaria & Pumir 2025).

4.4. *A note on experiments*

While the results discussed in this work are obtained primarily from DNS, they are also compared with experiments whenever possible. In particular, two types of experimental data are used for comparison: hot-wire measurements in a wind tunnel, and particle image velocimetry (PIV) in a von Kármán mixing tank. Although these experiments were not directly performed by us, it is still worth briefly discussing their characteristics and limitations to place the comparisons in the proper context.

For several decades, well before the advent of modern DNS, our understanding of turbulent flows relied heavily on wind-tunnel experiments using hot-wire anemometry. Standard hot-wire measurements provide the streamwise velocity as a function of time, at a fixed point in a flow. The technique relies on measuring changes in the electrical resistance of a thin heated wire, which varies as the wire is cooled by the incoming flow; since the cooling rate depends on the local flow velocity, the resistance fluctuations can be calibrated to yield the instantaneous velocity signal. Thereafter, using Taylor's frozen-turbulence hypothesis, which requires the turbulence intensity to be small compared with the mean-flow velocity, the temporal signal can then be interpreted as a spatial record of the flow field. In its standard configuration, a hot-wire probe provides measurements of one velocity component along one spatial direction, typically denoted $u_1(x_1)$, and if the resolution of the signal is sufficiently fine ($\lesssim \eta_K$), also the longitudinal velocity gradient A_{11}. More sophisticated cross-wire probes can also measure the transverse component $u_2(x_1)$.

The primary advantage of wind-tunnel measurements is the ability to achieve high Reynolds numbers – arguably the highest attainable in controlled laboratory conditions – making them particularly valuable for validating intermittency theories and scaling laws in the inertial range. However, the scope of these measurements is inherently limited since they provide information only along a single spatial direction. As a result, many analyses rely on 1-D surrogates for quantities that are intrinsically three-dimensional, often presuming local isotropy without being able to actually test it.

For the wind-tunnel comparisons presented here, we rely primarily on the measurements reported by Sreenivasan & Antonia (1997), Shen & Warhaft (2002) and Gylfason, Ayyalasomayajula & Warhaft (2004). Although these datasets are not the most recent available, they remain among the most carefully documented wind-tunnel measurements which provide access to longitudinal and transverse statistics at high Reynolds numbers, and also with sufficient resolution to measure velocity-gradient statistics. Although not shown, tests are underway that compare new experiments at the Göttingen wind tunnel with DNS, and reaffirm the conclusions drawn in this work.

A complementary experimental approach is provided by PIV, which enables spatially resolved measurements of velocity fields. In PIV experiments, tracer particles are seeded into the flow and illuminated by a laser sheet, allowing velocity vectors to be reconstructed from successive images of the particle motion (as captured by high-speed cameras). In the present work, we utilise PIV data in a von Kármán mixing tank, a configuration consisting of counter-rotating disks that generate intense turbulent motion in a confined vessel. Measurements are made in a small volume around the centre of the vessel, where the symmetry of the flow ensures that the mean velocity is approximately zero.

Unlike hot-wire measurements, PIV provides simultaneous measurement of velocity over an extended spatial region, enabling measurement of the full 3-D velocity field on a 3-D grid, and if the grid resolution is small enough ($\lesssim \eta_K$), of the full velocity-gradient tensor – much in the same spirit as in DNS (Wallace & Vukoslavčević 2010; Lawson & Dawson 2014). Despite sustained progress, current PIV measurements remain restricted to lower Reynolds numbers compared with wind-tunnel experiments. Additionally, improving the resolution (with respect to η_K) comes at the expense of further reducing the Reynolds number. Consequently, PIV experiments capable of resolving η_K operate at substantially lower Reynolds numbers compared with both DNS and wind-tunnel experiments. In the present work, we use the PIV data reported by Knutsen *et al.* (2020), corresponding to $Re_\lambda = 200$, with a spatial resolution of $0.8\,\eta_K$, thus providing access to the full velocity-gradient tensor. More recent experiments using particle tracking velocimetry, are now able to reach higher Reynolds numbers, up to $Re_\lambda = 277$ (Musci *et al.* 2025), while resolving the Kolmogorov scale – with experiments at even higher Reynolds numbers underway. Although not shown, the results from Musci *et al.* (2025) also reaffirm the conclusions drawn in this work.

5. Intermittency: phenomenology and scaling

The self-similarity of K41, grounded in dissipation anomaly, presumes a constant rate of energy transfer across scales, ultimately leading to viscous dissipation. For an eddy of size r, with characteristic velocity increment δu_r, this implies: $\epsilon \sim u_r^3/r$, which is corroborated by the 4/5th law exactly derivable from the INSE. This can be restated as

$$\delta u_r \sim (\epsilon r)^{1/3}, \tag{5.1}$$

which, upon naively averaging for any moment order p, leads to the K41 result of $\zeta_p = p/3$. Such an averaging, however, is fundamentally tenuous for any p since both δu_r and ϵ are random variables. As noted in previous sections, the distributions of velocity gradients and dissipation rate are strongly non-Gaussian, with intermittent bursts far exceeding their mean amplitude. Essentially, the key shortcoming of the K41 argument can be expressed mathematically as $\langle \epsilon^{p/3} \rangle \neq \langle \epsilon \rangle^{p/3}$ for $p \neq 3$, highlighting that the mean dissipation alone cannot predict the scaling of higher moment orders.

This limitation was recognised early on (see e.g. Frisch 1995 for a historical exposition), and Kolmogorov himself proposed the refined similarity hypothesis in 1962 (Kolmogorov 1962) henceforth K62, introducing the concept of locally averaged dissipation rate ϵ_r, which accounts for spatial fluctuations of ϵ. The refined view posits that (5.1) be instead written as

$$\delta u_r \sim (\epsilon_r r)^{1/3}, \tag{5.2}$$

leading to the general result

$$\langle (\delta u_r)^p \rangle \sim \langle \epsilon_r^{p/3} \rangle \, r^{p/3}. \tag{5.3}$$

Owing to intermittency, the locally averaged dissipation exhibits anomalous scaling: $\langle \epsilon_r^p \rangle \sim r^{\tau_p}$, which in turn produces the refined similarity relation for exponents

$$\zeta_p = \frac{p}{3} + \tau_{p/3}. \tag{5.4}$$

This remarkably establishes a direct connection between the intermittency of gradients (averaged over scale r) and the scaling of structure functions: knowledge of one prescribes the other. However, predicting the precise form of either requires further modelling assumptions.

To that end, K62 assumes a log-normal distribution of ϵ_r to derive an analytical expression for τ_p and ζ_p, providing the first quantitative prediction of intermittency. While this simple model works reasonably well, it also has known limitations (Frisch 1995). With the development of modern mathematical tools rooted in fractal geometry, a more general formalism, the multifractal model, to characterise intermittency was established (Benzi *et al.* 1984; Parisi & Frisch 1985), which provides an encompassing view of all models (including K41 and K62). In the following subsection, we introduce this multifractal formalism and show how it extends and refines Kolmogorov's ideas, allowing us to predict anomalous scaling for both structure functions and gradients.

5.1. *Multifractal model: basic framework*

The underlying framework for the multifractal model can be presented in several ways, but the essence of them all is the same. For instance, one can directly build the framework around velocity increments (Benzi *et al.* 1984), or alternatively, around locally averaged dissipation (Meneveau & Sreenivasan 1987), both being equivalent through the relation in (5.4). Since our discussion has already been focused on velocity increments and gradients, we will use the former approach, mostly following the presentation of Frisch (1995). For a more refined exposition, we also refer the readers to recent work of Dubrulle (2019, 2022).

In the multifractal model, the global scale invariance of K41, characterised by a single scaling exponent (in (5.1)), is replaced by a local scale invariance, with a spectrum of scaling exponents. Formally, the velocity increment across a scale r is taken to be locally Hölder continuous

$$\delta u_r/U \sim (r/L)^h, \qquad r/L \to 0, \tag{5.5}$$

where the exponent h varies in the interval $h_{min} \leqslant h \leqslant h_{max}$. Each value of h is realised on a geometrical set with a fractal dimension $D(h)$, such that the probability to observe the exponent h for the scale r is $P_r(h) \sim r^{3-D(h)}$, with $3 - D(h)$ being the co-dimension. The function $D(h)$ is also called the multifractal spectrum and is presumed to be universal.

The structure functions can be obtained by integrating over the sets of exponents

$$\left\langle (\delta u_r)^p \right\rangle / U^p \sim \int_{h_{min}}^{h_{max}} \left(\frac{r}{L}\right)^{ph+3-D(h)} \mathrm{d}h. \tag{5.6}$$

From the steepest descent estimation, i.e. in the limit $r/L \to 0$, it is easy to deduce that

$$\left\langle (\delta u_r)^p \right\rangle / U^p \sim \left(\frac{r}{L}\right)^{\zeta_p} \tag{5.7}$$

with ζ_p, corresponding to the smallest possible scaling exponent (for a given value of p), defined as

$$\zeta_p = \inf_h \left[ph + 3 - D(h)\right] = h^* p + 3 - D(h^*), \tag{5.8}$$

where $h^* = h^*(p)$ is the critical point satisfying: $D'(h^*(p)) = p$. Thus, the scaling exponents ζ_p arise as the Legendre transform of the multifractal spectrum $D(h)$, with each moment order coming from a different value of h and $D(h)$, i.e. each exponent ζ_p comes from a unique fractal set. It is not difficult to assess that ζ_p for increasing p values come from smaller h values, corresponding to rarer and more intense events. Note that the K41 phenomenology corresponds to a single fractal set with $h = 1/3$, $D(h) = 3$.

A couple of important observations are in order. In K41, scaling relations and universality are formulated relative to Kolmogorov scales, defined using viscosity (see (3.1)) and the inertial range emerges as an asymptotic regime at larger Reynolds numbers. By contrast, the multifractal description of turbulence is formulated directly in the inertial range by assuming that the velocity increments are Hölder continuous. As we

model	$\zeta_p =$	$h_{min} =$
Log-normal (Kolmogorov (1962), Obukhov (1962))	$\frac{p}{3} - \frac{\mu}{18} p(p-3)$ $\mu \approx 0.22$	$-\infty$ (unphysical)
p-model (Meneveau & Sreenivasan, 1987)	$1 - \log_2[p_1^{p/3} + p_2^{p/3}]$ $p_1 = 0.7,\ p_2 = 1 - p_1$	$-\frac{1}{3}\log_2 p_1 \approx 0.17$
Log-Poisson (She & Leveque (1994), Dubrulle (1994))	$\frac{p}{9} + 2[1 - (\frac{2}{3})^{p/3}]$	$\frac{1}{9} \approx 0.11$
SY2021 (Sreenivasan & Yakhot (2021))	$p\zeta_\infty/(p - 3 + 3\zeta_\infty)$ $\zeta_\infty \approx 7.3$	0

Table 2. Theoretical predictions for scaling exponents ζ_p from notable intermittency models, along with the h_{min} value for each.

will see in the next subsection, the dissipation scale is later obtained as a cutoff that depends on the local value of h. Thus, the universality in the multifractal description of turbulence is fundamentally different. Since only $D(h)$ is presumed to be universal, only the scaling exponents can now be universal, whereas the proportionality constants could be flow-dependent.

It is worth emphasising that $D(h)$ has never been explicitly derived from the INSE, nor its presumed universality been formally established. In fact, such a derivation from the INSE might possibly be fundamentally out of reach. Consequently, one must again rely on phenomenological approaches to obtain $D(h)$ or even directly ζ_p. Since ζ_p and $D(h)$ form a Legendre transform pair, the knowledge of one uniquely determines the other. In particular, the relation in (5.8) can be inverted to express $D(h)$ as

$$D(h) = \inf_p \, [ph + 3 - \zeta_p], \tag{5.9}$$

with the critical point satisfying: $\partial\zeta_p/\partial p = h^*(p)$. In principle, one can also obtain $D(h)$ directly from the data using wavelet transforms (Muzy, Bacry & Arneodo 1991), which could be more reliable than using (5.9).

Several phenomenological models have been developed over the past few decades. A vast majority of them fall under the umbrella of so-called cascade models, which use multiplicative processes to model the energy cascade (Frisch 1995). The more recent model by Sreenivasan & Yakhot (2021) utilises ideas from functional renormalisation group to develop a prediction for ζ_p, but can easily be recast in the multifractal framework by obtaining $D(h)$ through a Legendre transform of ζ_p (Buaria & Sreenivasan 2023*c*). Given that these models have been extensively studied before, we will not go into their details. For comparison, we recount what we consider to be some landmark intermittency models in table 2, along with the relevant references.

The predictions from these models, alongside results from DNS and experiments, were presented earlier in figure 7. Focusing first on the longitudinal exponents, it is evident that all models reasonably capture the observed deviations from K41. Interestingly, the best prediction appears to be the log-normal model, with $\mu \approx 0.22$ (Buaria & Sreenivasan

2022*a*). However, it is well known that the log-normal model is untenable for large p, as incompressibility requires ζ_p to be a non-decreasing function of p, i.e. $\partial\zeta_p/\partial p \geqslant 0,\ \forall\ p$ (Frisch 1995). Since the solution to (5.9) is given as $\partial\zeta_p/\partial p = h^*(p)$, the previous condition also imposes that $h_{min} \geqslant 0$. It is easy to see that these constraints are violated by the log-normal model for high p values, beyond what is shown in figure 7. Given the practical difficulties in obtaining converged statistics for very high moment orders, the log-normal model still serves as a remarkably simple and practical model for capturing intermittency (see also Dubrulle 2019).

The above inconsistency is fixed in other models, namely the p-model (Meneveau & Sreenivasan 1987), the log-Poisson (She & Leveque 1994; Dubrulle 1994) and the more recent SY2021 model (Sreenivasan & Yakhot 2021). From figure 7 we see that they are essentially indistinguishable up to $p = 8$, but show conspicuous deviations from DNS data at higher orders, with SY2021 providing the closest prediction. A notable feature of the SY2021 model is that it also corresponds to the limiting case of $h_{min} = 0$. It readily follows from (5.8) that for $h_{min} = 0$, $\zeta_p = 3 - D(0)$, suggesting a saturation of exponents at large p. The SY2021 model predicts $\zeta_\infty = 7.3$, although observing this asymptotic saturation would require extremely high-order moments ($p \geqslant 100$), which is well beyond feasible statistical convergence (essentially making it impossible to verify). Thus, despite the empirical success and physical consistency of various models, the precise asymptotic form of ζ_p, and by extension the full hierarchy of singularities in turbulence, remains an open theoretical problem.

Interestingly, the transverse exponents shown in figure 7 already appear to saturate for $p \geqslant 10$, suggesting that the longitudinal exponents may eventually do the same. However, no predictions for scaling of transverse exponents are available in the literature, the classical presumption being that they would scale identically as their longitudinal counterpart. Remarkably, $\zeta_\infty^{\mathrm{T}} \approx 2$ for transverse exponents, in excellent agreement with saturation of Lagrangian scaling exponents (Buaria & Sreenivasan 2023*c*), affirming that this saturation is in fact a genuine dynamical feature of small scales (and not a statistical artefact). This also raises some important questions about the physical significance of this asymmetry and how to model it, challenging the current understanding of small-scale turbulence.

5.2. *Multifractal model: extension to gradients*

The multifractal framework, originally developed for velocity increments in the inertial range, can also be extended to describe velocity gradients (Nelkin 1990; Benzi *et al.* 1991; Frisch 1995). This extension raises subtle issues at the conceptual level, since gradients by definition reside at the smallest scales where viscous effects dominate and inertial assumptions are no longer valid. Despite this, the framework provides a systematic way to formulate predictions once suitable assumptions are made. Once again, we follow the framework used by Frisch (1995). Starting from (5.5), and defining gradient as $\partial_x u = \lim_{r\to 0} \delta u_r/r$, it follows that

$$\partial_x u \sim \frac{U}{L}\left(\frac{r}{L}\right)^{h-1}\Bigg|_{r=\eta(h)}, \tag{5.10}$$

where $\eta = \eta(h)$ marks the dissipative cutoff in the limit $r \to 0$. Following the same steps as for structure functions, the order-n moment of velocity gradient is given by

$$\langle(\partial_x u)^n\rangle \sim \left(\frac{U}{L}\right)^n \int_h \left(\frac{r}{L}\right)^{n(h-1)+3-D(h)} \mathrm{d}h\,\Bigg|_{r=\eta(h)}. \tag{5.11}$$

The dissipative cutoff must now be identified to determine the relevant scale η for the gradients. In K41, this scale is simply η_K defined from mean dissipation, but in the multifractal formalism, this scale fluctuates, depending on h. A correspondence to K41 can be drawn here, where the viscous scales correspond to a local Reynolds number of unity, i.e. $u_K \eta_K/\nu = 1$. For multifractals, this condition is imposed as (Paladin & Vulpiani 1987)

$$\frac{\delta u_r\, r}{\nu} = 1. \tag{5.12}$$

Combining the above condition with (5.5) and setting $r = \eta$, it follows that

$$\frac{\eta}{L} \sim Re^{-\frac{1}{(h+1)}}, \tag{5.13}$$

where we have also used $Re = UL/\nu$. It is easy to see that $\eta_K = \eta(h = (1/3))$, but for $h < (1/3)$, scales smaller than η_K will develop in the flow.

Combining the result in (5.13) with (5.10), and invoking the steepest descent argument for $Re \to \infty$ (or $\nu \to 0$) leads to the power-law dependence

$$\langle (\partial_x u)^n \rangle \sim (U/L)^n\, Re^{\rho_n}, \tag{5.14}$$

with scaling exponents given by

$$\rho_n = \sup_h \frac{n(1-h) - 3 + D(h)}{1+h}. \tag{5.15}$$

Since $D(h)$ is uniquely determined from ζ_p (given in (5.9)), it follows that ρ_n is also uniquely determined from ζ_p. This relation can be made explicit by using the relation $D'(h*) = p$ obtained from (5.8) and $D(h^*) = ph^* + 3 - \zeta_p$ from (5.9). Using these relations with maximisation of the right-hand side in (5.15) leads to the relation (Frisch 1995)

$$\zeta_p + p = 2n. \tag{5.16}$$

The solution $p(n)$ to the above equation for a given value of n provides the corresponding result

$$\rho_n = p(n) - n, \tag{5.17}$$

for the scaling exponents. Thus, instead of using $D(h)$, one can also directly use ζ_p to compute the Re-scaling exponents for velocity gradients. The above scaling result can also be rewritten in terms of central moments $\langle (\partial_x u)^n \rangle / \langle (\partial_x u)^2 \rangle^{n/2}$, which are equivalent to $M_n \equiv \langle (\partial_x u)^n \rangle \tau_K^n$ defined earlier in § 3.1. Using $Re \sim Re_\lambda^2$, the scaling relation for central moments in terms of Taylor-scale Reynolds number can be rewritten as

$$M_n = c_n Re_\lambda^{\xi_n}, \quad \xi_n \equiv 2\rho_n - n = 2p(n) - 3n, \tag{5.18}$$

with $p(n)$ being the solution of (5.16). Alternatively, one can also write $\xi_n = 3(p/3 - \zeta_p)/2$. Since $p/3 - \zeta_p$ increases as p increases (for $p > 3$), it follows that ξ_n (and also ρ_n) also increase with n. As before, it is straightforward to show that higher moment orders come from increasingly smaller values of h and $D(h)$, corresponding to rarer and extremer events.

It is easy to see that for $n = 2$, the solution to (5.16) corresponds to $p = 3$, $\zeta_p = 1$, giving $\rho_2 = 1$, $\xi_2 = 0$, consistent with scaling of the third-order structure function and dissipation anomaly. Additionally, the K41 result of $\zeta_p = p/3$, leads to the solution $p(n) = 3n/2$, giving $\xi_n = 0$, as also predicted by K41. Since intermittency leads to $\zeta_p < p/3$ for $p > 3$,

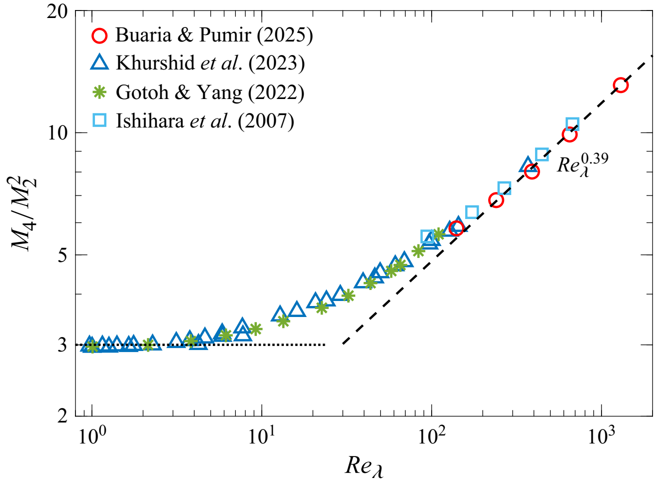

Figure 8. Flatness M_4/M_2^2 of longitudinal velocity gradients as a function of Re_λ over the range $1 \leqslant Re_\lambda \leqslant 1300$. The asymptotic power-law scaling of the moments appears to emerge only for $Re_\lambda \gtrsim 200$. All data correspond to DNS of isotropic turbulence, with sources indicated in the legend. A similar figure for the flatness of transverse velocity gradients can be found in Buaria (2026).

it implies that $p(n) > 3n/2$ and thus (ρ_n and) $\xi_n > 0$. Interestingly, it also follows from (5.16) that $p(n) < 2n$, thus giving the bound

$$3n/2 < p(n) < 2n, \quad n > 2, \;\; p > 3, \tag{5.19}$$

for relating nth moment of velocity gradient and pth-order structure function. In practice, since ζ_p are reliably obtained up to $p \leqslant 12$ (figure 7), the corresponding gradient exponents ξ_n can be accurately obtained up to $n \lesssim 8$. In the next subsection, we thus quantitatively compare the multifractal predictions for ξ_n up to $n = 8$, against results from DNS and experiments, to assess their accuracy and range of validity.

5.3. *Scaling of longitudinal gradients*

To assess the validity of multifractal predictions for longitudinal velocity-gradient moments $\langle(\partial_x u)^n\rangle$, it is first essential to establish the scaling regime where a clear power-law scaling emerges as a function of Re_λ. In the inertial range, the power-law scaling exponents describe the dependence of structure functions on the spatial separation r, and are expected to be independent of Re_λ – with only the extent of the scaling range increasing with Re_λ. By contrast, the moments of the velocity gradient depend explicitly on Re. Some recent studies (Schumacher *et al.* 2014; Sreenivasan & Yakhot 2021; Khurshid, Donzis & Sreenivasan 2023) have suggested that the scaling of the velocity-gradient moments emerges at very low Re_λ ($\gtrsim 10$), substantially lower than what is necessary to observe scalings in the inertial range. However, these studies were limited to low Reynolds number ($Re_\lambda \lesssim 200$), and therefore did not shed much light on the scaling regimes at large Re_λ.

To resolve this question, we compile HIT data from various sources (Ishihara *et al.* 2007; Gotoh & Yang 2022; Khurshid *et al.* 2023), including our own at higher Reynolds numbers (Buaria & Pumir 2025), and inspect the flatness (or kurtosis) of the longitudinal gradients in figure 8. The dataset spans three (six) orders of magnitude in Re_λ (Re), providing a comprehensive view of the scaling with respect to Re_λ. From this plot, the following observations can be made: (i) at very low Re_λ, the flatness is close to 3, corresponding to a

https://doi.org/10.1017/jfm.2026.11494 Published online by Cambridge University Press

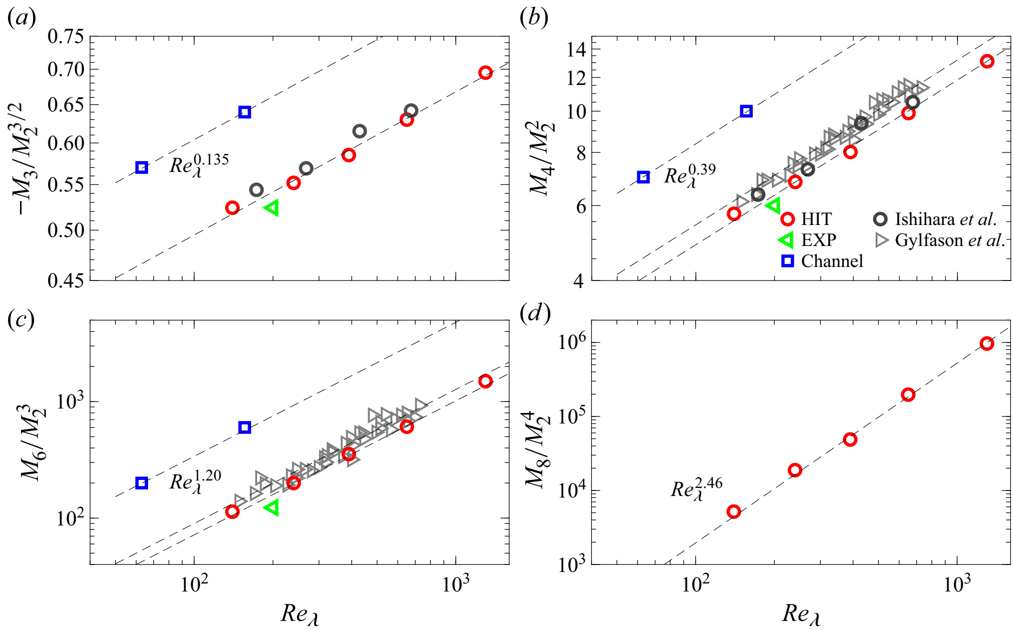

Figure 9. (*a*) Skewness, $M_3/M_2^{3/2}$, (*b*) flatness, M_4/M_2^2, (*c*) hyperflatness M_6/M_2^3 and (*d*) normalised eighth moment, M_8/M_2^4 of longitudinal velocity gradients as a function of Re_λ for different cases. The DNS data, shown by the black circles, are from Ishihara *et al.* (2007), and the experimental data shown as grey triangles are from Gylfason *et al.* (2004). All panels share the same legend.

Gaussian distribution, (ii) the flatness steadily increases with Re_λ, approaching a power law only at much higher Re_λ. It is evident that the transition from Gaussian to non-Gaussian is smooth and gradual, and not a sharp one – contrary to what was proposed in Sreenivasan & Yakhot (2021) and Khurshid *et al.* (2023). In particular, the range $Re_\lambda \lesssim 200$ (for HIT) corresponds to a transitional regime. Thus, any power laws extracted here, do not correspond to true asymptotic scaling of velocity-gradient moments. This analysis underscores that identifying power laws in velocity-gradient moments also requires high Re_λ, very much alike capturing inertial-range scalings. Hence, when extracting the scaling exponents for velocity gradients, we will henceforth ignore low-Re_λ data. Note that although not shown, similar transitional behaviour is obtained in other flows, with the asymptotic state reached at different Re_λ than for HIT.

Figure 9 shows the scaling of central moments for orders $n = 3$, 4, 6 and 8. In addition to our own HIT data reaching up to $Re_\lambda = 1300$, we also utilised data from other sources, including laboratory experiments, DNS of channel flows and other well-resolved HIT datasets previously reported in the literature. Remarkably, we observe that the scaling exponents are the same for all flows, with different proportionality constants. This is consistent with the expectation of universality in the multifractal framework.

To test the multifractal predictions outlined earlier, we extract the scaling exponents from DNS data and report the values in table 3. The predictions from various models, outlined previously in table 2, are also shown. These predictions are obtained using the ζ_p listed in table 2, and solving (5.16) and (5.18). It can be readily observed that all models provide good predictions for the low-order moments, but deviate at higher orders. Assuming the multifractal approach to be valid, any discrepancy in theoretical predictions for ξ_n exponents stems from discrepancies in the predictions for the values of

	ξ_3	ξ_4	ξ_6	ξ_8
Log-normal	0.137	0.38	1.21	2.50
p-model	0.135	0.35	0.94	1.67
Log-Poisson	0.141	0.36	1.00	1.83
Original SY2021	0.102	0.33	1.03	1.97
SY2021 with multifractal	0.153	0.39	1.10	2.04
DNS	0.138 ± 0.002	0.39 ± 0.006	1.20 ± 0.03	2.46 ± 0.10

Table 3. Scaling exponents for longitudinal gradient moments.

ζ_p themselves. In this sense, the deviations between the predictions of ξ_n and the measured values are not surprising since the model predictions of ζ_p itself deviate from the values obtained from DNS data at high p values, see figure 7. Interestingly, the best predictions are observed for the log-normal model. This is also not surprising since the log-normal model provides the best fit to ζ_p in the range of p considered, see figure 7. Naturally, the predictions of the log-normal model are not expected to be correct for moments much larger than those considered, given the known deficiencies of this model (Frisch 1995). Importantly, the values of the exponents ζ_p and ξ_n obtained from DNS are perfectly consistent with the multifractal description. In fact, the values of p and ζ_p deduced from the numerical value of ξ_n, using (5.16) and (5.18), agree very well with the dependence of ζ_p on p illustrated in figure 7.

As a side remark, we note that table 3 includes two distinct predictions based on the ζ_p values from Sreenivasan & Yakhot (2021). The first one (labelled 'original SY2021') follows the relation proposed by Yakhot & Sreenivasan (2005) and Sreenivasan & Yakhot (2021), which essentially postulates that the exponents ξ_n are related to ζ_p for $p = 2n$, that is, the moments of the gradients of order n come from structure functions of order $2n$. This approach differs from the multifractal one, which predicts that the moments of order n of the moments are related to pth-order structure function with $3n/2 < p < 2n$ as given in (5.19). However, as noted earlier, the extraction of ξ_n in their previous works (Schumacher *et al.* 2014; Sreenivasan & Yakhot 2021) relied on very low Re_λ, where the power law is still changing. This led to a fortuitous agreement between the data and theory. But as we can see in table 3, when ζ_p of Sreenivasan & Yakhot (2021) is utilised with the multifractal result, the predictions are in better agreement with the DNS results (keeping in mind the discrepancies for ζ_p at high p values).

5.4. *Universality*

The results in figure 9 clearly support the universality of scaling exponents. At the same time, they raise the natural question about how the flow Reynolds number should be interpreted in such comparisons, since the proportionality constants remain flow-dependent. It is worth pointing out that all definitions of flow Reynolds numbers are constructed from large-scale quantities: the r.m.s. velocity U together with the integral length scale L or the Taylor-scale λ. In contrast, the Reynolds number of smallest scales associated with the gradients is of order unity – as expressed by (5.12). This mismatch makes the flow Reynolds number an imperfect reference when comparing small-scale statistics. Instead, we posit that a more consistent approach would be to directly use a small-scale quantity to characterise the turbulence intensity, such as the skewness or flatness of velocity gradients, which vary monotonically with Re_λ. Thereafter, remaining gradient moments can be instead formulated in terms of this reference moment – akin to extended self-similarity (Benzi *et al.* 1993) for velocity gradients – with the hope that

https://doi.org/10.1017/jfm.2026.11494 Published online by Cambridge University Press

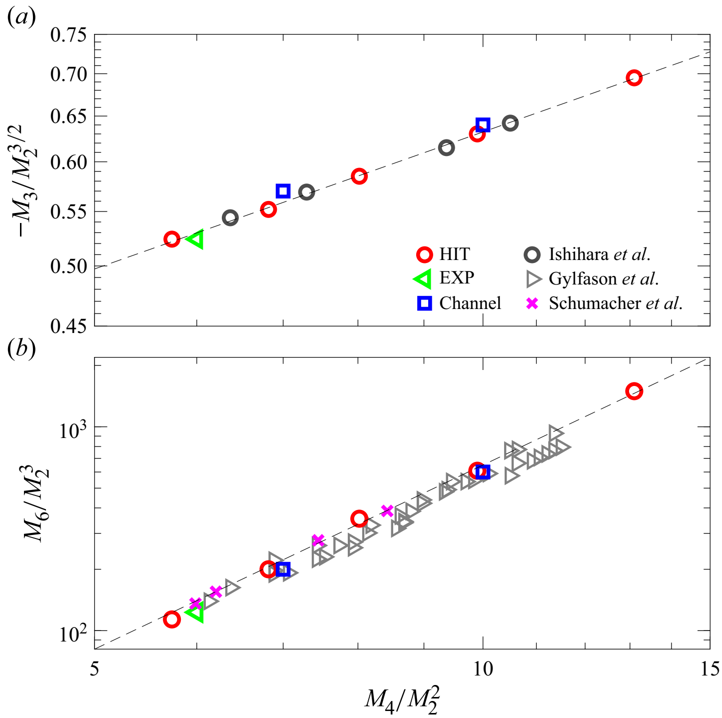

Figure 10. (*a*) Skewness, $M_3/M_2^{3/2}$ and (*b*) hyperflatness, M_6/M_2^3 as a function of flatness for different flows. The data from Schumacher *et al.* (2014) correspond to DNS of Rayleigh–Bénard convection. Figure adapted from Buaria & Pumir (2025).

proportionality constants now may become flow-independent as the scaling laws are no longer formulated in terms of Reynolds number (and large-scale quantities).

Using the available data in figure 9, this idea is illustrated in figure 10, which shows skewness vs. flatness (panel *a*) and sixth moment (hyperflatness) vs. flatness (panel *b*). In both cases, data from different flows collapse onto a single flow-independent curve. This constitutes a stronger demonstration of universality, beyond what is suggested by multifractals. Essentially, the results in figure 10 can be generally described as

$$M_n/M_2^{n/2} = K_n (M_4/M_2^2)^{\xi_n/\xi_4}, \tag{5.20}$$

where the proportionality constants K_n are also universal constants, just as the scaling exponents. Note that the choice of using flatness as the dependent variable is arbitrary and, in principle, one can use any other moment.

The results in figure 10 imply that the statistical properties of the velocity gradients in different flows (albeit in regions of weak or no mean shear) are identical to those obtained from HIT, once the turbulence intensity has been matched. Our results indicate that, instead of simply trying to match the large-scale or Taylor-scale Reynolds number, one needs to precisely match the small-scale statistics such as skewness or flatness of velocity gradients. Using this idea, one can easily infer an exact correspondence between two different flows. For instance, using channel flow and HIT as two reference flows, one can observe from figure 10 that the $Re_\tau = 1000$ and 5200 runs for channel flow are equivalent to $Re_\lambda = 240$ and 650 runs for HIT, respectively, and therefore differ significantly from estimates of Re_λ using classical methods. On the other hand, the estimate of $Re_\lambda = 200$

in the von Kármán flow experiment (Knutsen *et al.* 2020) is only slightly larger than $Re_\lambda = 140$ in HIT. Likewise, similar mappings can also be made for other flows, which an interested reader may wish to explore.

It is worth noting that Kolmogorov (1962) also predicts a form of universality consistent with that demonstrated above. Assuming log-normality of the locally averaged dissipation rate, ϵ_r, Kolmogorov (1962) showed that

$$\langle \epsilon_r^n \rangle / \langle \epsilon \rangle^n = \exp[\sigma^2 n(n-1)/2], \tag{5.21}$$

where σ^2 denotes the variance of the Gaussian variable $\log(\epsilon_r/\langle\epsilon\rangle)$. It is straightforward to see that the above expression is equivalent to stating

$$\langle \epsilon_r^n \rangle / \langle \epsilon \rangle^n = \left[\langle \epsilon_r^2 \rangle / \langle \epsilon \rangle^2 \right]^{n(n-1)/2}. \tag{5.22}$$

If one further assumes that for some $r = \eta$, $\epsilon_r \to \epsilon$, that is the same dissipative cutoff prescribes all gradient moments (note that K62 presumes $\eta = \eta_K$), then it can be seen that the above relation becomes equivalent to (5.20). The proportionality constants K_n are then prescribed by isotropic relations connecting moments of ϵ and $\partial u/\partial x$, and are therefore universal, while the exponents satisfy $\xi_{2n}/\xi_4 = n(n-1)/2$, or equivalently $\xi_n/\xi_4 = n(n-2)/8$. An inspection of the DNS results in table 3 shows that this prediction works reasonably well (within some small error).

Given that the log-normal model provided a reasonable description of both structure functions and gradient statistics, this agreement is perhaps not surprising. However, it is important to emphasise that the K62 prediction differs fundamentally from the multifractal framework. In the multifractal model, the dissipative cutoff η is different for each moment order, reflecting the presence of a hierarchy of singularities, whereas in K62 a single cutoff $\eta = \eta_K$ is assumed for all moments. In fact, Kolmogorov (1962) assumes a specific form for the variance $\sigma^2 = \log A + \mu \log(L/r)$, which results in $\xi_4 = 3\mu/2$, which for $\mu \approx 0.22$ underpredicts the observed result of $\xi_4 \approx 0.39$. However, using multifractals to relate inertial and dissipation ranges accurate predicts this result. This disparity raises an important question regarding the nature of the universality observed in figure 10. It is feasible that the apparent universality of K_n is only approximate, with discernible deviations only emerging at sufficiently high moment orders (beyond available here). Fully resolving this issue would require very high resolution DNS and experiments of various non-HIT flows at high Reynolds numbers, such that high moment orders can be accurately extracted.

5.5. *Scaling of transverse gradients*

The success of the multifractal framework in capturing the intermittency of longitudinal gradients from inertial-range exponents naturally motivates its application to the study of transverse gradients. As mentioned previously, from a purely phenomenological perspective, the multifractal model does not differentiate between longitudinal and transverse components. Essentially, one would expect identical scaling results for transverse increments and gradients as their longitudinal counterparts. However, we already saw in figure 7 that was not the case. While the scaling exponents for longitudinal and transverse structure functions are similar at low moment orders, systematic differences emerge at higher orders, with the transverse exponents consistently smaller, indicating stronger intermittency. Such differences have long been reported in the literature (Chen *et al.* 1997; Shen & Warhaft 2002; Gotoh *et al.* 2002), but have often been attributed to the low Reynolds numbers or experimental uncertainties in measuring high-order structure functions. With modern DNS now achieving both high Reynolds number and

https://doi.org/10.1017/jfm.2026.11494 Published online by Cambridge University Press

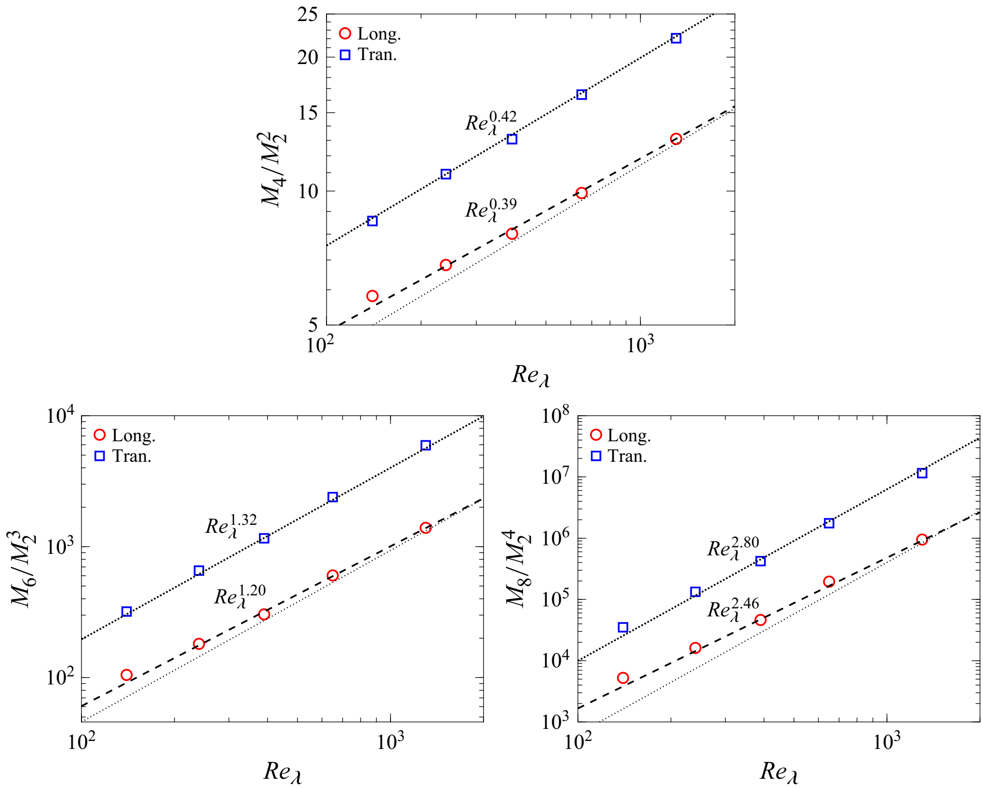

Figure 11. Dependence of the normalised moments of the longitudinal (circle) and transverse (squares) velocity gradients on Re_λ. Power laws are indicated for each set of data points.

finer resolution, it has become clear that the distinction is genuine: transverse exponents do differ from their longitudinal counterpart (Iyer *et al.* 2020; Buaria & Sreenivasan 2023*c*).

Given the differences in their inertial-range exponents, it is natural to expect that transverse and longitudinal gradient moments also scale differently. This is indeed the case, as illustrated in figure 11, which shows normalised fourth- and sixth-order moments for both. The dashed lines show the power laws for longitudinal moments, (with ξ_4 and ξ_6 reported earlier in table 3), while dotted lines show their transverse counterparts. The slopes differ slightly but systematically, indicating that transverse gradients grow more strongly with the Reynolds number.

To deduce the scaling of transverse moments, one can repeat the earlier steps for longitudinal counterpart, i.e. utilise ζ_p^{T} from figure 7, together with the relation in (5.18). However, since $\zeta_p^{\mathrm{T}} \approx 2.1$ beyond $p \geqslant 10$, it is easy to deduce that $\xi_n^{\mathrm{T}} = n - 2\,\zeta_\infty^{\mathrm{T}}$, beyond $n \gtrsim 6$. This leads to the expectation that $\xi_6^{\mathrm{T}} \approx 2$, whereas $\xi_8^{\mathrm{T}} \approx 4$, both of which are substantially higher than the values observed in figure 11. Hence, while the multifractal formalism successfully describes longitudinal gradients, it does not seem to work for transverse gradients (the predicted scaling being much steeper than actually observed).

Although the somewhat nominal Re_λ range over which clear scaling can be established introduces some uncertainty in the precise values of ξ_n, this is likely a minor issue in light of the overall consistency across datasets and models. The observed trends are robust and indicate that longitudinal and transverse gradients follow genuinely distinct scaling behaviours. Most phenomenological approaches do not explicitly differentiate between the two, yet the numerical results in figures 7 and 9 present evidence to the contrary. The persistence of these differences, even at the highest accessible Re_λ, therefore represents a key open challenge for turbulence theory – one that any comprehensive theory of intermittency and universality must ultimately resolve.

The somewhat limited Re_λ-range over which the scaling is identified introduces some uncertainty in the extracted ξ_n values. It remains conceivable that the longitudinal moments have not yet reached their fully asymptotic regime and might converge towards the larger observed exponents for transverse gradients at substantially high Re_λ. However, such a scenario would likely also require a corresponding change in the inertial-range scaling exponents at very high Re_λ. the inertial-range scaling exponents would also have to change noticeably at much high Re_λ. Given the robustness of the present results and the persistent lack of theoretical understanding of transverse scaling exponents, it appears more plausible that the underlying assumptions themselves need to be revisited. As will be shown in coming sections, the dynamics governing longitudinal and transverse gradients differs fundamentally and is unaccounted for in prevailing phenomenological approaches. This naturally calls for a reformulation of the theoretical framework to explicitly account for their distinct dynamical roles.

5.6. *Moments of dissipation and enstrophy*

Up to this point, our discussion has primarily focused on statistics of longitudinal and transverse gradients, because of their conceptual simplicity in representing the full tensorial picture under the assumption of local isotropy. Additionally, these 1-D quantities are more readily measurable in classical wind-tunnel experiments, using single or cross hot-wires. However, as discussed earlier in § 2.2, strain and vorticity, and their norms, $\varSigma = 2S_{ij}S_{ij}$, $\varOmega = \omega_i\omega_i$, contain richer information about the small-scale dynamics governing the mechanisms that underlie the energy cascade and gradient amplification. In fact, $\varSigma$ is essentially the dissipation rate, which plays a central role in intermittency theories. Accordingly, studying the moments of $\varSigma$ and $\varOmega$ provides a more comprehensive and physically grounded view of intermittency.

From a physical perspective, regions dominated by strong vorticity can be expected to produce large transverse gradients, while regions of strong strain give rise to large longitudinal gradients. From this standpoint, the individual gradient components could be viewed as statistical projections of the underlying fluctuations of $\varSigma$ and $\varOmega$, suggesting a natural relation between the scaling of the moments of order $2n$ of the longitudinal and transverse velocity derivatives and the moments of order n of $\varSigma$ and $\varOmega$. Note that isotropic relations (given earlier in § 3.3) already provide some exact results to that end. For instance, from the isotropic form of the fourth-order tensor in (3.12), the second-order gradient moments follow, $\langle\varOmega\rangle = \langle\varSigma\rangle = 15\langle A_{11}^2\rangle = (15/2)\langle A_{12}^2\rangle = 1/\tau_K^2$.

The relations for fourth-order gradient moments are more involved, since the eighth-order tensor involves four invariants, as given earlier. For that case, one can derive (Siggia 1981)

$$I_1 = \frac{105}{4}F_1, \qquad I_4 = 45F_1 - 480F_2 + 80F_3 + 120F_4, \tag{5.23}$$

where I_1 and I_4 are the second-order moments of dissipation and enstrophy, while F_1 and F_3 correspond to the fourth-order moments of the longitudinal and transverse moments, respectively, as defined earlier in § 3.3. Thus, in this case, while dissipation can be directly related to the longitudinal gradient, enstrophy in principle is connected to both longitudinal and transverse gradients.

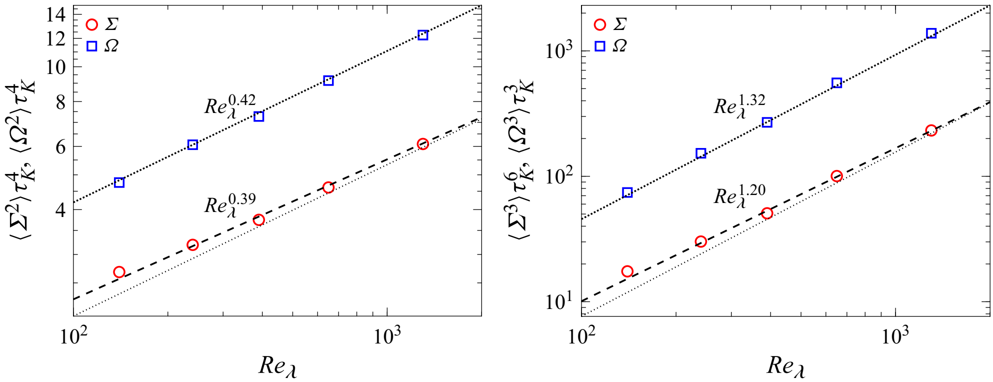

Figure 12. Normalised second and third moments of Ω and Σ as a function of Re_λ. The power-law exponents are identical to those of fourth and sixth moments of longitudinal and transverse gradients as shown in figure 8.

Nevertheless, when examining the scaling of dissipation and enstrophy moments, we empirically find that they are still prescribed solely by longitudinal and transverse velocity gradients, respectively. Figure 12 shows the scaling of normalised second- and third-order moments of Σ and Ω as functions of Re_λ. As anticipated, the power-law scalings for each moment order match perfectly with the observed scalings for respective gradients in figure 11. Quantitatively, the data yield

$$\frac{\langle A_{11}^4\rangle}{\langle A_{11}^2\rangle^2} = \frac{15}{7}\,\langle\Sigma^2\rangle\,\tau_K^4, \quad \frac{\langle A_{12}^4\rangle}{\langle A_{12}^2\rangle^2} \approx 1.8\,\langle\Omega^2\rangle\,\tau_K^4, \tag{5.24}$$

where the first relation is exact from isotropy, but the second one is empirical, suggesting the contribution to enstrophy is dominated by the transverse gradient (and conversely). Although isotropic relations for even higher moments are more involved (Boschung 2015), the comparison between figure 11(*b*) and figure 12(*b*) suggests that empirical relations could still be formulated between higher-order moments of dissipation and enstrophy and those of corresponding longitudinal and transverse gradients, respectively.

6. Extreme events and small-scale structure

6.1. *Smallest scales from multifractal*

As defined in (5.13), the viscous cutoff in the multifractal model is given by $\eta(h) = LRe^{-(1/1+h)}$. Since each gradient moment corresponds to a specific local Hölder exponent h, it follows that each moment corresponds to its own viscous cutoff. The K41 result for $h = 1/3$ corresponds to the second-order gradient moment with $\eta = \eta_K = LRe^{-3/4}$. Higher-order moments come from smaller values of h, implying increasingly smaller values of $\eta(h)$ than η_K. This naturally leads to the question of what the smallest scales in the flow are, corresponding to h_{min}.

Using (5.13), it is easy to show that the smallest length scale η_{min}, corresponding to h_{min} are given as

$$\eta_{min} \sim \eta_K\, Re_\lambda^{-\alpha}, \quad \text{where} \quad \alpha = \frac{1-3h_{min}}{2(1+h_{min})}, \tag{6.1}$$

where we have used $\eta_K = LRe^{-3/4}$ and $Re \sim Re_\lambda^2$. Since the time scale is the inverse of the gradient, the smallest time scale τ_{min} in the flow can be quantified using the infinity norm of gradients (i.e. the most extreme gradient)

$$\tau_{min} = \lim_{n\to\infty} \frac{1}{\langle(\partial_x u)^n\rangle^{1/n}}. \tag{6.2}$$

Using (5.14) and (5.15), with $\tau_K = (L/U)Re^{-1/2}$ (corresponding to $h = 1/3$), it can be easily shown that τ_{min} scales as

$$\tau_{min} \sim \tau_K \; Re_\lambda^{-\beta}, \quad \text{where} \quad \beta = 2\alpha. \tag{6.3}$$

Finally, using (5.12), we can also identify the velocity increment over the smallest scale as $\delta u|_{\eta_{min}} = \nu/\eta_{min}$, which can be shown to scale as

$$\delta u|_{\eta_{min}} \sim u_K Re_\lambda^{\alpha} \sim U Re_\lambda^{\alpha-\frac{1}{2}}, \tag{6.4}$$

where we have used $u_K = U\, Re_\lambda^{-1/2}$ Thus, by identifying h_{min}, the above relations can prescribe the scaling of the smallest scales in the flow.

As mentioned earlier, the multifractal framework itself does not prescribe a unique value for h_{min}. However, specific intermittency models, such as those discussed in the previous section, yield explicit predictions for h_{min}, as provided in table 2. As hinted earlier, physical consistency requires that $h_{min} \geqslant 0$ (Frisch 1995), making the log-normal predictions for moments of very high orders and negative h_{min} untenable. By contrast, other models predict physically admissible values of h_{min}; but only the SY2021 model prescribes $h_{min} = 0$, which has also been suggested before (Paladin & Vulpiani 1987). Despite its obvious importance, it must be noted that no direct evaluation of h_{min} has been made, since it explicitly requires measuring the infinity norm of gradients (or velocity increments).

Interestingly, the result $h_{min} = 0$ has a measurable effect on inertial-range exponents ζ_p. From (5.8), it is easy to argue that in the limit $p \to \infty$, $h_{min} = 0$ implies that the exponent $\zeta_\infty = 3 - D(0)$, i.e. they saturate when the moment order p goes to infinity. Thus, $h_{min} = 0$ is always accompanied by saturation of inertial-range exponents. Although the precise value of p at which such a saturation can be observed depends on the form of $D(h)$ While a saturation is not observed for longitudinal exponents, numerical results do point to a saturation for transverse moments – as seen in figure 7, and also for Lagrangian exponents, see Buaria & Sreenivasan (2023*c*). Given the other evidence presented here, it is reasonable to assume that $h_{min} = 0$, leading to $\alpha = 1/2$ and $\beta = 1$ in (6.1) and (6.3). This is also consistent with the expectation that $\delta u \sim U$ for the smallest scales. In the following subsection, we will try to characterise the most extreme velocity gradients in hope of confirming the above results.

6.2. *Characterising extreme events*

Capturing the most extreme events in turbulence – those associated with the strongest gradients, vorticity or strain – is notoriously challenging, both computationally and statistically. In this section, we restrict attention to data from our DNS of HIT described in § 4 and summarised in table 1. This choice allows a clear assessment of extreme fluctuations under the most controlled conditions (given the high resolution datasets for HIT). Nevertheless, questions of universality will be addressed soon after.

Since no theoretical bound exists for the extent of velocity-gradient distribution and convergence of such a measure for an unbounded distribution would in principle demand infinite statistics, a direct estimate is unattainable. Instead, we adopt a semi-explicit approach, where we directly characterise the tails of the distributions under the assumption

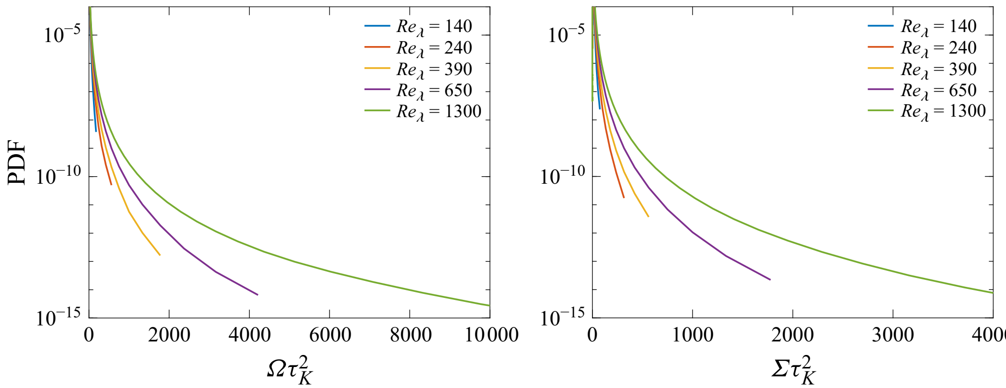

Figure 13. Probability density functions of $\Omega = \omega_i\omega_i$ and $\Sigma = 2S_{ij}S_{ij}$, both normalised by their mean $\langle\Omega\rangle = \langle\Sigma\rangle = 1/\tau_K^2$, for different Re_λ listed in table 1 (*a*) Ω; (*b*) Σ. Figure adapted from Buaria & Pumir (2022).

that they follow a preset functional form. Rather than examining the PDFs of velocity gradients (as shown earlier in figure 5), we will utilise the PDFs of strain and vorticity, as previously defined by their square-norms $\Sigma = 2S_{ij}S_{ij}$ and $\Omega = \omega_i\omega_i$ in (2.7). This choice has two important advantages. First, these quantities have the same mean value and also a clearer physical significance, which will allow us to identify and connect to the physical mechanisms underlying extreme events. Second, the square-norms are positive definite and extend the accessible tails of the PDFs, enabling more reliable functional fits.

Figure 13 shows the PDFs of Σ and Ω, normalised by their mean $1/\tau_K^2$, at different Re_λ. For any given Re_λ, the extent of the PDF of Ω is larger than that of Σ, consistent with a stronger intermittency of transverse components discussed earlier. It is readily evident that as Re_λ increases, extreme events (for both Σ and Ω) become more intense (going up to thousands of times the mean), and are also more frequent. In all cases, the extent of the tails shown is restricted on the basis of statistical convergence; essentially, the bins shown are converged with respect to both small-scale resolution and statistical sampling. Events more extreme and rare than shown are obviously expected, however, we will assume that they conform to a functional form capturing the tails shown.

To capture the Re_λ-dependence of the outmost part of the PDF tails, we propose a simple rescaling of the PDFs. We define the following time scale to rescale the extreme values:

$$\tau_{ext} = \tau_K \, Re_\lambda^{-\beta'}. \tag{6.5}$$

This scale mimics the one defined in (6.3), but for now we keep them separate, and will soon evaluate how τ_{ext} compares with τ_{min} from multifractal model. Denoting $f_\Omega(\Omega_e)$ and $f_\Sigma(\Sigma_e)$ as the PDFs of $\Omega_e = \Omega\tau_{ext}^2$ and $\Sigma_e = \Sigma\tau_{ext}^2$, respectively, figure 14 shows the rescaled PDFs, $Re_\lambda^\delta f_\Omega(\Omega_e)$ and $Re_\lambda^\delta f_\Sigma(\Sigma_e)$, where factor Re_λ^δ captures the likelihood of extreme events. The exponents β' and δ are empirically determined by assuming a functional form of the PDF tails. Remarkably, the same values of β' and δ collapse PDFs of both Ω and Σ indicating that their most extreme events scale similarly, even though their finite order moments do not.

The fitting procedure to obtain β' and δ is described in details in Buaria *et al.* (2019) and Buaria & Pumir (2022), but we summarise the essential aspects here. While several functional forms have been proposed in the literature, the stretched exponential form

$$f_X(x) = a\exp(-bx^c), \tag{6.6}$$

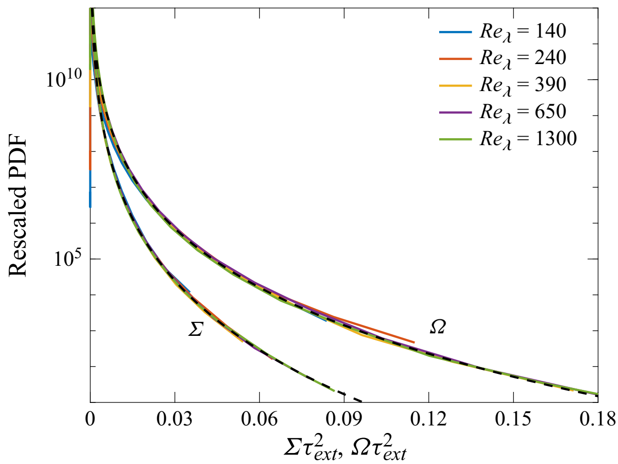

Figure 14. Rescaled PDFs of Ω and Σ, rescaled by τ_{ext}^2, where $\tau_{ext} = \tau_K Re_\lambda^{-\beta}$, with β increasing from approximately 0.7 to 0.8 with Re_λ. The PDFs have been rescaled by Re_λ^δ, with $\delta \approx 4$. The dashed black curves correspond to stretched exponential fits of the form given in (6.6). Figure adapted from Buaria & Pumir (2022).

where $x = \Omega\tau_K^2$ or $\Sigma\tau_K^2$, is particularly known to fit the PDF tails very accurately (Meneveau & Sreenivasan 1991; Zeff *et al.* 2003; Donzis, Yeung & Sreenivasan 2008; Buaria *et al.* 2019; Gotoh, Watanabe & Saito 2023). Applying a change of variables: $x_e = x \times (\tau_{ext}/\tau_K)^2$, where $x_e = \Omega_e$ or Σ_e, the collapse shown in figure 14 requires that

$$b\ Re_\lambda^{2\beta' c} = b', \quad a\ Re_\lambda^{(2\beta'+\delta)} = a', \tag{6.7}$$

such that b' and a' are constants independent of Re_λ. Thus, β' can be directly obtained from the dependence of $b^{1/c}$ on Re_λ.

To determine the fitting coefficients, one can simply fit the tails of the logarithm of the PDFs to the functional form ($\log a - bx^c$) of (6.6). However, a direct fit requires nonlinear regression, which can be very sensitive to initial seed, leading to large error bars. To mitigate that, we choose the value of c beforehand (in the range $0.19 \leqslant c \leqslant 0.29$ as dictated by initial nonlinear fits), reducing the fitting procedure to a linear regression problem, providing exact results for coefficients a and b. Figure 15 shows the variation of $b^{1/c}$ with Re_λ for different values of c chosen. The data points, corresponding to the fits for Ω and Σ, have been shifted for clarity, so that they coincide for $Re_\lambda = 1300$. Remarkably, we see that data points at other Re_λ also almost perfectly coincide with each other, implying that the slope of $b^{1/c}$ with Re_λ is essentially insensitive to the fitting procedure. Although not shown, the exponent δ is also extracted in a similar fashion.

It is worth noting from figure 15 that the slope of the data points (which gives β') is not constant, but rather changes slowly, with β' varying from approximately 0.71 to 0.8 in going from $Re_\lambda = 140$ to 1300. Thus, the collapse shown in figure 14 utilises this varying value of β'. Recall that for $h_{min} = 0$, the multifractal model gives $\beta = 1$ (for τ_{min} defined in (6.3)). Thus, based on the scaling of the PDF tails, we see that τ_{ext} does not quite match the expected τ_{min} from multifractals, but there is a tendency for τ_{ext} to slowly approach τ_{min} as Re_λ increases. A similar observation was also made by Elsinga, Ishihara & Hunt (2020) when considering the scaling of extreme dissipation events. The physical origin of β' is investigated in the next subsection, but we will return to the comparison with multifractal results soon after.

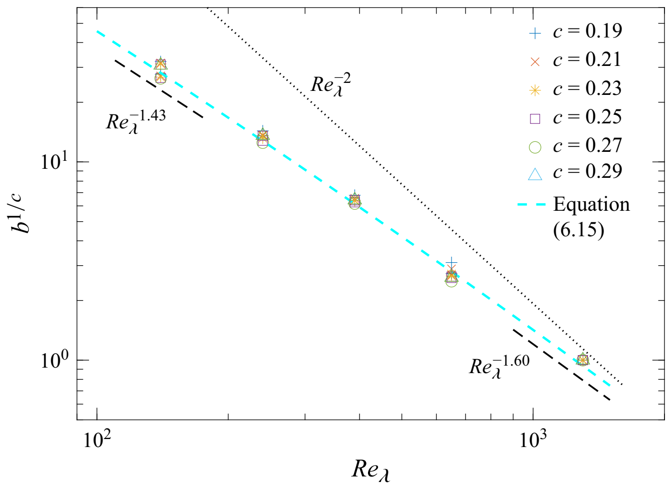

Figure 15. Plot of $b^{1/c}$ vs Re_λ corresponding to stretched exponential fits given in (6.6) to PDFs of $\varOmega$ and $\varSigma$ shown previously in figure 13. For clarity, we have rescaled the data points, so that points for $Re_\lambda = 1300$ exactly superpose. The dashed cyan curve corresponds to the prediction of β' as given in (6.15). Figure adapted from Buaria & Pumir (2022).

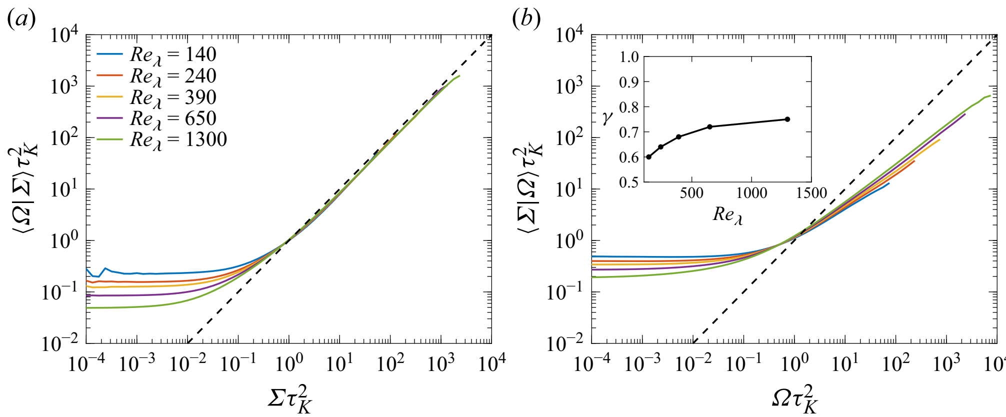

Figure 16. Conditional expectations (a) $\langle \varOmega | \varSigma \rangle$ and (b) $\langle \varSigma | \varOmega \rangle$. The dashed black line in each plot corresponds to a straight line of slope unity. Inset in panel b shows γ as a function of Re_λ, for a power-law fit $\langle \varSigma | \varOmega \rangle \sim \varOmega^\gamma$ applied in the region $\varOmega \tau_K^2 \gtrsim 1$. Figure adapted from Buaria & Pumir (2025).

6.3. *Relating scaling to flow dynamics*

To explain the scaling of PDF tails captured by the scale τ_{ext}, we utilise some key aspects of the flow dynamics arising from the interaction of strain and vorticity. The first is the observation that extreme gradients are organised in vortical filaments, surrounded by sheet-like regions of intense strain, as illustrated in figure 2. Although $\varOmega$ and $\varSigma$ have the same mean, we saw earlier that $\varOmega$ is more intermittent than $\varSigma$. Moreover, even though extreme events of $\varOmega$ and $\varSigma$ scale with τ_{ext}, they are not spatially co-located. This suggests a non-trivial interrelationship between strain and vorticity. To better understand it, we consider their mutual conditional expectations, as shown in figure 16. From figure 16(a), we observe that intense events of $\varSigma$ are locally accompanied by proportionately intense events of $\varOmega$, i.e. $\langle \varOmega | \varSigma \rangle \sim \varSigma$. However, the converse is not true.

From figure 16(*b*), we observe that strain in regions of intense vorticity is relatively weaker and empirically described by a power law

$$\langle \Sigma | \Omega \rangle \tau_K^2 \sim \left(\Omega \tau_K^2\right)^{\gamma}, \quad 0 < \gamma < 1, \tag{6.8}$$

where the exponent γ slowly increases with Re_λ, as shown in the inset of figure 16(*b*). More specifically, γ increases from approximately 0.6 at $Re_\lambda = 140$ to approximately 0.75 at $Re_\lambda = 1300$. Thus, there is an intrinsic asymmetry between vorticity and strain, which arises from the Navier–Stokes dynamics. This asymmetry can be understood by exploring the non-local relationship between strain and vorticity, as will be discussed in § 8. We next utilise this asymmetry (reflected in the exponent γ), along with the knowledge of vortical flow structures to quantify the scaling of extreme events.

From a physical standpoint, we can assert that the smallest length scale in the flow corresponds to the smallest dimension of the most intense vortical filaments, as also supported by visualisations in figure 2. This results from a balance between viscosity and some effective strain $S_e \simeq \Sigma_e^{1/2}$ acting on the filament (Burgers 1948): $\eta \simeq (\nu^2/\Sigma_e)^{1/4}$, which can be rewritten as

$$\eta/\eta_K \simeq \left(\Sigma_e \tau_K^2\right)^{-1/4}. \tag{6.9}$$

Note that this relation is essentially equivalent to the assumption that the local Reynolds number is unity, when defining the smallest scale – as also assumed in multifractals earlier in (5.12). It can be easily seen that the classical K41 result corresponds to $\Sigma_e = \langle \Sigma \rangle = \langle \epsilon \rangle / \nu$. Instead, based on the observation in figure 16(*b*), we utilise the conditional relation in (6.8), leading to

$$\eta/\eta_K = \left(\Omega \tau_K^2\right)^{-\gamma/4}. \tag{6.10}$$

Introducing the length scale η_{ext} as the size associated with vortex filaments corresponding to most Ω_{max}, which in turn corresponds to scale τ_{ext}, i.e. $\Omega_{max} \sim 1/\tau_{ext}^2$, we obtain

$$\eta_{ext}/\eta_K \simeq (\tau_{ext}/\tau_K)^{\gamma/2}. \tag{6.11}$$

We can define the scaling of η_{ext} as

$$\eta_{ext} \sim \eta_K \, Re_\lambda^{-\alpha'} \tag{6.12}$$

which combined with τ_{ext} from (6.5) leads to the relation

$$2\alpha' = \gamma \beta'. \tag{6.13}$$

Evidently, η_{ext} mimics the η_{min} from multifractals defined in (6.1), just as τ_{ext} mimics τ_{min}. However, the corresponding relation between the exponents for η_{min} and τ_{min} in multifractal model was $2\alpha = \beta$ (given in (6.3)).

An additional relation between α' and β' can be obtained by simply evaluating the largest velocity increment leading to the strongest gradient across the smallest length scale, i.e. $1/\tau_{ext} = \delta u_{max}/\eta_{ext}$. Several earlier works (Jiménez *et al.* 1993; Ishihara *et al.* 2007; Buaria *et al.* 2019) have established that velocity increments across vortex tubes are as large as the r.m.s. of velocity fluctuations, i.e. $\delta u_{max} \sim U$. This can also be observed in figure 17, which shows the PDFs of (transverse) velocity increments δu_r for $r/\eta_K \leqslant 1$. The PDFs extend all the way to $|\delta u_r|/U \sim 1$, for all Re_λ shown.

Thus, one can write $1/\tau_{ext} \sim U/\eta_{ext}$, which leads to the relation

$$\beta' = \alpha' + \frac{1}{2}. \tag{6.14}$$

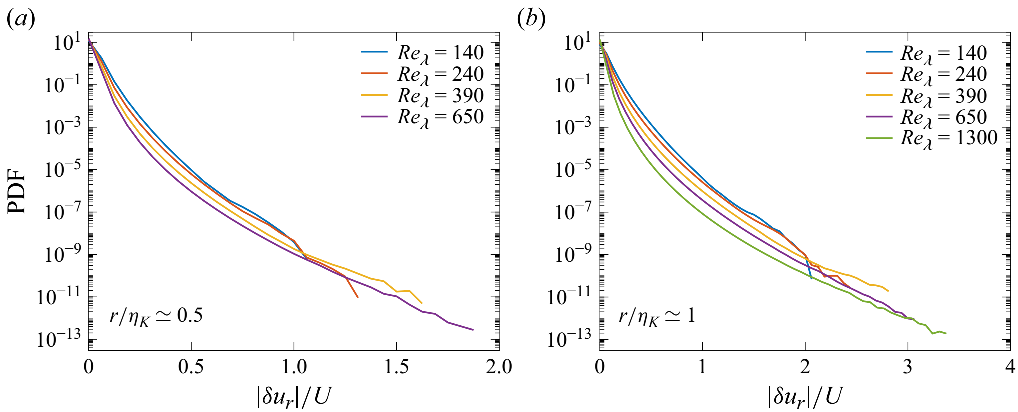

Figure 17. Probability density functions of transverse velocity increments, normalised by r.m.s. of velocity U, over distances (*a*) $r/\eta_K = 0.5$ and (*b*) $r/\eta_K = 1$, at various Re_λ. The PDFs highlight that strongest velocity increments over smallest scales are of the order of U. Figure adapted from Buaria & Pumir (2022).

Solving the above equation together with (6.13) then leads to

$$\beta' = \frac{1}{2-\gamma}, \quad \alpha' = \frac{1}{2(2-\gamma)}, \tag{6.15}$$

which provides the scaling of extreme events solely in terms of the exponent γ. As noted earlier, γ varies from 0.6 to 0.75 across the range of Re_λ available (see the inset of figure 16*b*). This implies that β' varies from approximately 0.714 to 0.80. This prediction was shown earlier in figure 15 (dashed cyan line), and compared with data points obtained from curve fitting procedure to collapse the PDF tails. It can be seen that the model prediction for β' is in perfect agreement with the data, providing strong justification for the collapse.

While the prediction for τ_{ext} (and β') was validated using PDF tails, validating the prediction for η_{ext} (and α') poses an inherent difficulty, as directly identifying the size of vortical filaments would be fraught with uncertainties. Another approach could be to evaluate the PDF of the coarse-grained gradient $\delta u_r/r$, over some scale r, and make it successively smaller until the PDF of $\delta u_r/r$ collapses to the PDF of velocity gradient for $r \leqslant \eta_{ext}$. However, this approach is also ambiguous since DNS provides discrete r values (in integer multiples of the grid spacing Δx). Instead, we devise an alternative approach by characterising the deviations of $\delta u_r/r$ from the actual gradient. Expressing the increment δu_r using a Taylor-series expansion leads to

$$\frac{\delta u_r}{r} = \frac{\partial u}{\partial x} + \frac{\partial^2 u}{\partial x^2}\frac{r}{2!} + \frac{\partial^3 u}{\partial x^3}\frac{r^2}{3!} + \ldots. \tag{6.16}$$

For $r \leqslant \eta_{ext}$, the right-hand side converges to $\partial_x u$, whereas for $r > \eta_{ext}$, deviations are expected due to higher-order derivatives. For the most extreme gradients, we can assert that $\partial^n u/\partial x^n \simeq c_n U/\eta_{ext}^n$, where c_n are independent of Re_λ. Together with $U \sim \eta_{ext}/\tau_{ext}$, this gives

$$\frac{\delta u_r \tau_{ext}}{r} \simeq c_1 + \frac{c_2}{2!}\left(\frac{r}{\eta_{ext}}\right) + \frac{c_3}{3!}\left(\frac{r}{\eta_{ext}}\right)^2 + \ldots, \tag{6.17}$$

leading to the expectation that the PDF tails of the quantity $\delta u_r \tau_{ext} r$ can be collapsed for different Re_λ by matching the r/η_{ext} values.

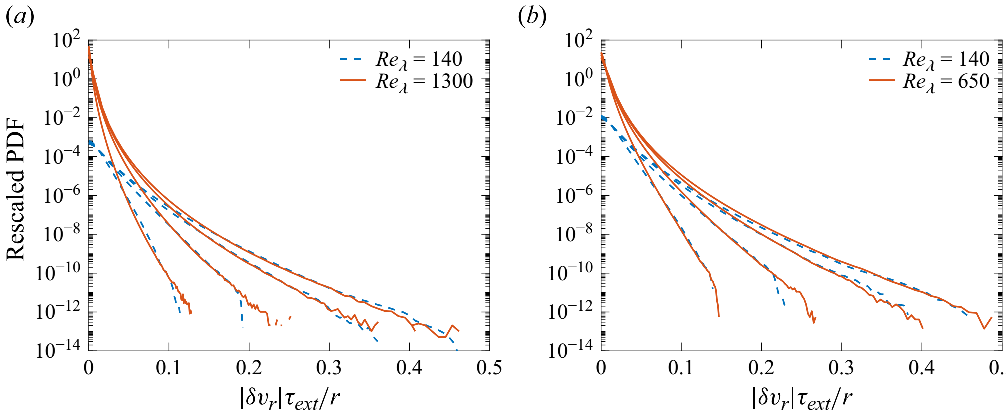

Figure 18. Comparison of rescaled PDFs of the transverse velocity increments, non-dimensionalised by τ_{ext}/r, between (*a*) $Re_\lambda = 140$ and $Re_\lambda = 1300$, and (*b*) $Re_\lambda = 140$ and $Re_\lambda = 650$. (*a*) Solid red lines for $Re_\lambda = 1300$, for $r/\eta_K = 1, 2, 4, 8$ and dashed blue line for $Re_\lambda = 140$ for $r/\eta = 2, 4, 8, 16$. (*b*) Solid red lines are for $Re_\lambda = 650$, showing $r/\eta_K = 1, 2, 4, 8$, and dashed blue lines are for $Re_\lambda = 140$, showing $r/\eta_K = 1.5, 3, 6, 12$. In each panel, curves for increasing r/η_K shift monotonically from right to left. Although not shown, the curves corresponding to the longitudinal increments exhibit similar behaviour. Figure adapted from Buaria & Pumir (2022).

From the values of γ and α', it turns out that η_K/η_{ext} at $Re_\lambda = 140$ is approximately twice larger than at $Re_\lambda = 1300$. Figure 18(*a*) shows the rescaled PDFs of the transverse velocity differences $\delta u_r \tau_{ext} r$ for $r/\eta_K = 1, 2, 4, 8$ at $Re_\lambda = 1300$ and $r/\eta_K = 2, 4, 8, 16$ at $Re_\lambda = 140$, showing an excellent collapse of the tails, and once again validating the results in (6.15). A similar comparison can be made for $Re_\lambda = 650$ and $Re_\lambda = 140$, with the ratio of their η_K/η_{ext} being approximately 1.5. This is shown in figure 18(*b*), further validating the prediction.

6.4. *Universality of vorticity–strain correlation*

The scaling of scales τ_{ext} and η_{ext} in the previous subsection relied exclusively on data from DNS of HIT. Central to this description is the conditional coupling between strain and vorticity, particularly the power-law dependence $\langle \Sigma | \Omega \rangle \sim \Omega^\gamma$. This naturally raises the question of the universality of this behaviour, especially the exponent γ and its dependence on Re_λ.

To address this, we extract the conditional expectations from other flows, including DNS for channel flow and tomographic-PIV experiments of Knutsen *et al.* (2020), where the full gradient tensor is available. Figure 19 shows the quantities (*a*) $\langle \Sigma | \Omega \rangle$ and (*b*) $\langle \Omega | \Sigma \rangle$ for all flows. We recall that the comparison between the moments of the longitudinal gradients, presented in § 5.3, led to the conclusion that the small-scale turbulence in the channel flow at $Re_\tau = 1000$ and 5200 is equivalent to HIT at $Re_\lambda = 240$ and 650, respectively. While the experiments at $Re_\lambda = 200$ align with HIT at Re_λ slightly larger than 140. The behaviour of $\langle \Sigma | \Omega \rangle$ in figure 19(*a*) shows a striking consistency across different flows, with the corresponding power-law exponents from channel flow and experiments almost perfectly matching with HIT data at corresponding Re_λ. Similarly, the behaviour of $\langle \Omega | \Sigma \rangle$ in figure 19(*b*) is also consistent across different flows – always adhering to the Σ^1 behaviour, independent of Reynolds number. Together, these results demonstrate a remarkable universality in the strain–vorticity coupling at small scales, implying that the underlying mechanisms driving the most extreme events are insensitive

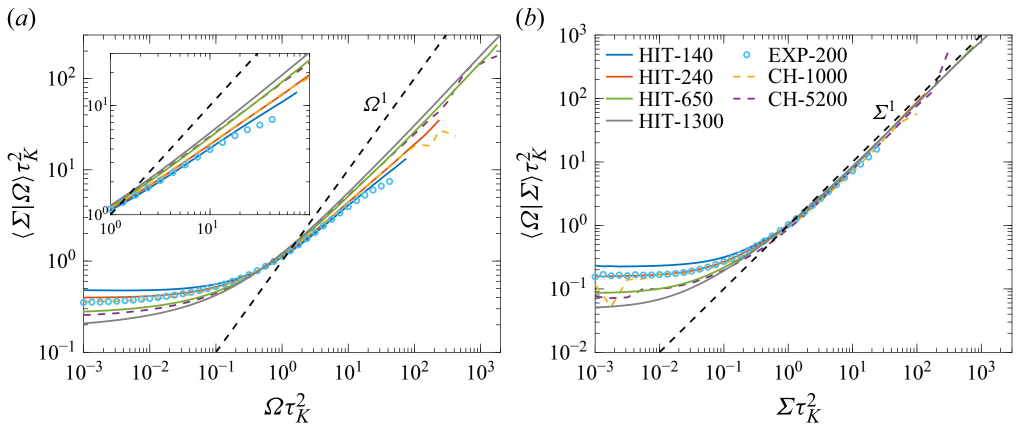

Figure 19. Conditional expectations (*a*) $\langle \Sigma | \Omega \rangle$ and (*b*) $\langle \Omega | \Sigma \rangle$, for different flows, as listed in the legend (shared by both panels). The inset in panel (*a*) shows a zoomed version of the curves. Figure adapted from Buaria & Pumir (2025).

to large scales. In the following sections, we will provide additional evidence supporting the universality of strain–vorticity dynamics across different turbulent flows and Reynolds numbers.

6.5. *Extreme events: a critical discussion*

The analysis in the previous subsections suggests the existence of two scales, τ_{ext} for time and η_{ext} for length, which characterise the most extreme events of $\Omega\tau_K^2$ and $\Sigma\tau_K^2$. The Reynolds dependence of these scales is given as

$$\tau_{ext} = \tau_K \, Re_\lambda^{-\beta'}, \qquad \beta' = \frac{1}{(2-\gamma)} \tag{6.18}$$

$$\eta_{ext} = \eta_K \, Re_\lambda^{-\alpha'}, \qquad \alpha' = \gamma\beta'/2 \tag{6.19}$$

where γ is the exponent characterising the relationship between strain and vorticity. In contrast, the smallest scales as described by the multifractal framework are given by

$$\tau_{min} = \tau_K Re_\lambda^{-\beta}, \qquad \beta = \frac{1-3h_{min}}{1+h_{min}}, \tag{6.20}$$

$$\eta_{min} = \eta_K Re_\lambda^{-\alpha}, \qquad \alpha = \beta/2, \tag{6.21}$$

where h_{min} is the smallest possible Hölder exponent in the flow. It is reasonable to infer from all the evidence that $h_{min} = 0$, suggesting $\beta = 2\alpha = 1$. This is equivalent to assuming that the largest velocity increments at the smallest scales are given by $\delta u_r \sim U$, which is well supported by data analysed here and also prior works (Paladin & Vulpiani 1987; Jiménez *et al.* 1993; Buaria *et al.* 2019; Sreenivasan & Yakhot 2021).

The trend for the exponent γ suggests $\gamma \to 1$ when $Re_\lambda \to \infty$. In this case, the two approaches provide identical results in the limit of $Re_\lambda \to \infty$. But at the finite Re_λ values currently available – which appear high enough to extract asymptotic scalings – these two results appear fundamentally different. Thus, one must reconcile them appropriately. Firstly, it is worth discussing whether these sets of scales are supposed to be identical. For the scales characterising the most extreme events, our focus was explicitly on vorticity and strain. Given that extreme vorticity resides in tube-like structures, and strain in sheet-like structures around these tubes, the 'extreme' scales identified by us simply correspond to geometric properties of such (most extreme) structures.

In contrast, the multifractal picture remains somewhat agnostic of the underlying dynamics stemming from the INSE. Its scaling predictions emerge statistically rather than dynamically by setting $h_{min} = 0$, supported by empirical observations that $\delta u_r \sim U$ and also from the plausible saturation of ζ_p at large p. Crucially, the multifractal model provides no direct prediction about the formation or role of vortex tubes, or other coherent structures shaping intermittency. Incidentally, the log-Poisson formulation of She & Leveque (1994), which was partly motivated by the notion of vortex filaments, predicts $h_{min} = (1/9)$, which is inconsistent with $h_{min} = 0$ inferred from the data, thus limiting its physical relevance.

Essentially, it remains unclear whether the smallest scales identified by the multifractal framework correspond in any way to the vortical structures observed in turbulence. This may be viewed as a shortcoming of multifractal model, since it does not necessarily provide any physical significance for the predicted smallest scales. Furthermore, the multifractal picture also offers no insight into how strain and vorticity correlate, specifically the asymmetry in their conditional expectations characterised by the exponent γ. A similar limitation was encountered earlier when comparing the scaling of longitudinal and transverse gradient moments. In this sense, one may conclude that the multifractal formalism, as it has been applied so far, is incomplete.

On the other hand, the analysis presented in this section also calls for caution. When identifying the extreme scales, our focus was on the outermost tails of the PDFs. We cannot rule out that events even more extreme and rare than those captured by the PDFs in figure 13 will appear if the statistical samples are dramatically increased, e.g. by extending the length of the simulations by orders of magnitude. Our assumption was that the functional form fitted to PDF tails would still capture such unresolved events; but it is entirely possible that the shape of the PDF experiences a sudden change for events much larger than the ones captured. To that end, one can argue that $\beta' = 0.8$ corresponding to observed PDF tails (and vortical structures), may simply correspond to $h_{min} > 0$ events. Specifically, substituting $\beta = 0.8$ in (6.3) gives $h_{min} \approx 0.05$, which corresponds to a high but finite order moment (and not the infinity norm). Thus, the disparity in the scaling of τ_{ext} and τ_{min} predicted by the multifractal model may not pose any contradiction. However, the value $h = 0.05$ also gives $\alpha = 0.4$ and $\delta u_r \sim U\ Re_\lambda^{0.1}$, which are not consistent with the collapse in figure 18 and the observation in figure 17, respectively.

Nevertheless, a few questions remain. The first is about the physical and dynamical relevance of η_{min} (and τ_{min}) predicted by the multifractal approach. If these are indeed the smallest scales in the flow, the DNS results suggest that they do not meaningfully contribute to the most extreme vorticity–strain events observed. Likely, their role will show up only when considering the highest moment orders of velocity gradients, higher than what can conceivably be determined statistically. Additionally, the derivation for η_{min} in the multifractal formalisms only required consideration of longitudinal gradients, and an explanation for the scaling of transverse components remains incomplete. In contrast, our focus on vortical structures to capture η_{ext} explicitly utilised both strain and vorticity. In fact, we note that in both cases the smallest scale identified corresponds to a local Reynolds number of unity, as identified by the longitudinal velocity increment. For a vortex tube, this is implicit in defining its radius by balancing viscosity and strain. In the multifractal framework, it is typically presumed that the Reynolds number based on the transverse component would also be unity. However, this does not bear out in practice. If we consider the circulation of a vortex tube Γ, then the local Reynolds number defined as $R_\Gamma = \Gamma/\nu$ is not unity; rather our results indicate $R_\Gamma = Re_\lambda^{1-\beta}$, which is consistent with the observations of Jiménez *et al.* (1993) (but instead of taking η_K as the relevant scale for the radius of tubes, we use η_{ext}). Note that for $Re_\lambda \to \infty$, the expectations that $\gamma, \beta \to 1$ imply that R_Γ tends to a constant value. Thus, all observations point to the fact that a consistent and correct theory of turbulence requires a joint description of longitudinal and transverse gradients (and increments), grounded in the dynamics of strain and vorticity.

7. Amplification dynamics

It is evident from the preceding sections that the amplification of strain and vorticity lies at the core of small-scale intermittency. In this section, we aim to elucidate how such an amplification arises dynamically and how it shapes the underlying flow structures responsible for intermittency. By jointly examining the dynamics of strain and vorticity, we seek to connect their amplification mechanisms to the emergence of coherent structures (vortex tubes and strain sheets). This dynamical viewpoint would provide a natural bridge between the statistical manifestations of intermittency and the fluid-mechanical processes that sustain them, hopefully paving the way towards a more unified physical description. It is worth noting that these nonlinear amplification mechanisms also engender the energy transfer from large to small scales, see e.g. Duchon & Robert (2000), Tsinober (2009), Carbone & Bragg (2020), Johnson (2020) and Vela-Martín (2022). Complementary to these works, our focus here will be to primarily understand the formation of extreme gradients.

To that end, we consider the transport equations for Ω and Σ, which can be derived from (2.5) and (2.6), respectively, by taking appropriate dot products. After standard manipulations, one obtains

$$\frac{1}{2}\frac{\mathrm{D}\Omega}{\mathrm{D}t} = \omega_i\omega_j S_{ij} + \nu\omega_i\nabla^2\omega_i, \tag{7.1}$$

$$\frac{1}{4}\frac{\mathrm{D}\Sigma}{\mathrm{D}t} = -S_{ij}S_{jk}S_{ki} - \frac{1}{4}\omega_i\omega_j S_{ij} - S_{ij}H_{ij} + \nu S_{ij}\nabla^2 S_{ij}. \tag{7.2}$$

These two equations encapsulate the essential physics of gradient amplification. Both involve the vortex stretching term, resulting from a coupling between vorticity and strain $\omega_i S_{ij}\omega_j$. The equation for Σ also involves the self-amplification term $-S_{ij}S_{jk}S_{ki}$. These two terms are local. In addition, (7.2) contains a coupling between strain and the pressure Hessian, H_{ij}, which is clearly a non-local term, as a consequence of (1.2). The absence of any explicitly non-local effect in the equation for vorticity makes (7.1) at first sight easier to study than (7.2). Note that (7.1) and (7.2) both involve viscous terms. In the following, we will not explicitly focus on those viscous terms, but refer the readers to Buaria *et al.* (2020*a*) for a more precise analysis of the viscous terms.

7.1. *Unconditional statistics*

We next focus on the local terms in (7.1) and (7.2), namely vortex stretching, $\omega_i\omega_j S_{ij}$ and $S_{ij}S_{jk}S_{ki}$. As commonly done, it is useful to analyse these terms in the eigenframe of the strain tensor: consisting of the three real eigenvalues λ_i, such that $\lambda_1 \geqslant \lambda_2 \geqslant \lambda_3$, and the corresponding eigenvectors $\boldsymbol{e}_i$. Incompressibility implies that

$$\lambda_1 + \lambda_2 + \lambda_3 = 0\,, \tag{7.3}$$

hence, $\lambda_1 > 0$ and $\lambda_3 < 0$. It is easy to show that $\Sigma = 2S_{ij}S_{ij} = 2(\lambda_1^2 + \lambda_2^2 + \lambda_3^2)$, and additionally

$$S_{ij}S_{jk}S_{ki} = \lambda_1^3 + \lambda_2^3 + \lambda_3^3 = 3\,\lambda_1\lambda_2\lambda_3. \tag{7.4}$$

For HIT, $\langle S_{ij}S_{jk}S_{ki}\rangle$ is simply related to the third moment of the longitudinal velocity derivative, A_{11} as $\langle S_{ij}S_{jk}S_{ki}\rangle = (105/8)\langle A_{11}^3\rangle$. For this reason, the observation that the third moment M_L^3 (defined by (3.6)) is negative, as shown in figure 9, also implies that $\langle S_{ij}S_{jk}S_{ki}\rangle < 0$, which further implies that the intermediate eigenvalue λ_2 is predominantly positive. Importantly, using (3.13), one immediately deduces that $\langle \omega_i\omega_j S_{ij}\rangle > 0$, so the term tends to amplify vorticity. Similarly, the average of the sum of the two local terms in (7.2) amounts to $-(4/3)\langle S_{ij}S_{jk}S_{ki}\rangle$, which is also positive, therefore leading to strain amplification. It is also easy to show, for homogeneous incompressible turbulence, that $\langle S_{ij}H_{ij}\rangle = 0$.

It is evident that the amplification of vorticity by strain depends not only on the magnitude of the strain and vorticity but also on the alignment between vorticity and strain eigenvectors $\boldsymbol{e}_i$. This can be seen by writing the vortex stretching term, $\omega_i\omega_j S_{ij}$ in the eigenframe of the strain tensor

$$\omega_i\omega_j S_{ij} = \lambda_i(\boldsymbol{e}_i\cdot\boldsymbol{\omega})^2 = \Omega\,\lambda_i(\boldsymbol{e}_i\cdot\hat{\boldsymbol{\omega}})^2, \tag{7.5}$$

where $\hat{\boldsymbol{\omega}}$ is the unit vector along vorticity. As a consequence of $S_{ii} = 0$, the vortex stretching term $\omega_i\omega_j S_{ij}$ is zero when the three components $(\boldsymbol{e}_i\cdot\hat{\boldsymbol{\omega}})^2$ are equal and very small when they are close to each other. The equation also shows that the distribution of eigenvalues of $\boldsymbol{S}$ plays an important role: a positive vortex stretching can be achieved when vorticity is preferentially aligned with positive eigendirections of strain, i.e. in the direction $\boldsymbol{e}_1$ or $\boldsymbol{e}_2$, since λ_2 is preferentially positive.

Empirically, one finds a remarkable alignment between vorticity and the intermediate eigenvalue of $\boldsymbol{e}_2$. This property, first noticed by Ashurst *et al.* (1987), has been amply confirmed in both DNS and experiments in different turbulent flows (Tsinober 2009; Wallace & Vukoslavčević 2010; Pumir, Xu & Siggia 2016; Musci *et al.* 2025). We illustrated the result in figure 20(a), which shows the PDF of $|\hat{\boldsymbol{\omega}}\cdot\boldsymbol{e}_i|$ for HIT, channel flow and experiments. Elementary geometrical considerations suggest that if $\hat{\boldsymbol{\omega}}$ were randomly aligned with respect to the three eigenvectors, $\boldsymbol{e}_i$, the PDF would be uniform. The very significant increase of $P(|\hat{\boldsymbol{\omega}}\cdot\boldsymbol{e}_2|)$ when $|\hat{\boldsymbol{\omega}}\cdot\boldsymbol{e}_2| \to 1$ implies a tendency of $\hat{\boldsymbol{\omega}}$ to align with $\boldsymbol{e}_2$. The PDF of $|\hat{\boldsymbol{\omega}}\cdot\boldsymbol{e}_3|$ has a maximum for $|\hat{\boldsymbol{\omega}}\cdot\boldsymbol{e}_3| \to 0$, implying that $\hat{\boldsymbol{\omega}}$ is predominantly perpendicular to $\boldsymbol{e}_3$. The average values of the cosines between $\hat{\boldsymbol{\omega}}$ and $\boldsymbol{e}_i$ provide a quantitative way to measure the alignment between the different vectors. We begin by noticing that when a vector $\boldsymbol{e}$ is randomly oriented with respect to $\boldsymbol{e}_i$, then $\langle(\boldsymbol{e}\cdot\boldsymbol{e}_i)^2\rangle = 1/3$ for $i = 1$, 2 and 3. The values of $\langle(\hat{\boldsymbol{\omega}}\cdot\boldsymbol{e}_i)^2\rangle$ are approximately independent of the specific flow, as well as of the Reynolds number, of the order of 0.320 : 0.523 : 0.157 (see also table II of Buaria *et al.* 2020a). The strong alignment between $\hat{\boldsymbol{\omega}}$ and $\boldsymbol{e}_2$, clearly visible in the panel (a) of figure 20 is reflected by the value $\langle(\boldsymbol{e}_2\cdot\hat{\boldsymbol{\omega}})^2\rangle \approx 0.523$, significantly larger than 1/3, and than the other values of $\langle(\hat{\boldsymbol{\omega}}\cdot\boldsymbol{e}_i)^2\rangle$ for $i = 1$ and $i = 3$.

To study the distribution of the intermediate eigenvalue of $\boldsymbol{S}$, we consider (Lund & Rogers 1994)

$$\lambda_2^* = \frac{\sqrt{6}\lambda_2}{\sqrt{||\boldsymbol{S}||^2}} = \frac{\sqrt{6}\lambda_2}{\sqrt{\lambda_1^2+\lambda_2^2+\lambda_3^2}}, \tag{7.6}$$

Re_λ	$\lambda_1 : \lambda_2 : \lambda_3$	$\lambda_1^2 : \lambda_2^2 : \lambda_3^2$	$\lambda_i (e_i \cdot \omega)^2$
140	0.379 : 0.089 : −0.468	0.183 : 0.024 : 0.293	0.115 : 0.101 : −0.056
240	0.372 : 0.088 : −0.460	0.183 : 0.024 : 0.293	0.123 : 0.106 : −0.061
390	0.367 : 0.086 : −0.453	0.184 : 0.024 : 0.292	0.131 : 0.110 : −0.066
650	0.357 : 0.083 : −0.440	0.184 : 0.024 : 0.292	0.144 : 0.118 : −0.074
1300	0.345 : 0.080 : −0.425	0.184 : 0.024 : 0.292	0.163 : 0.129 : −0.084

Table 4. Unconditional expectations of quantities related to vortex stretching, distinguishing the 3 eigendirections of the rate of strain tensor, $\boldsymbol{S}$. All quantities have been made dimensionless by the Kolmogorov time scale, τ_K.

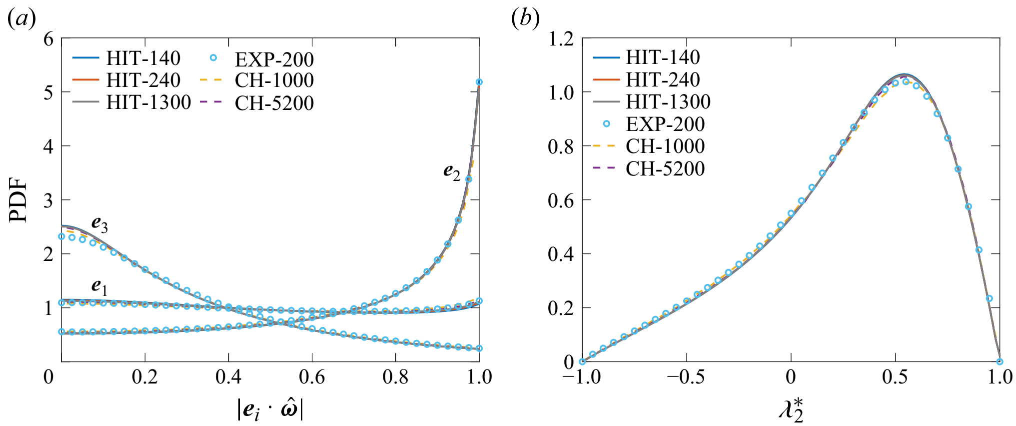

Figure 20. (*a*) The PDFs of the cosines of alignments between the vorticity unit vector $\hat{\boldsymbol{\omega}}$, and the eigenvectors $\boldsymbol{e}_i$ corresponding to the eigenvalues λ_i of the strain-rate tensor (with $\lambda_1 \geqslant \lambda_2 \geqslant \lambda_3$). (*b*) The PDF of λ_2^*, defined in (7.6), which measures the relative strength of the intermediate eigenvalue with respect to the overall strain amplitude. The curves shown include DNS, at $Re_\lambda = 140$, 240 and 1300, Channel flows and the experimental data of Knutsen *et al.* (2020), as indicated in the legend. All the curves shown superpose perfectly, demonstrating that the effect of Re_λ is minimal, and pointing to universality of the gradient statistics. Figure adapted from Buaria & Pumir (2025).

which satisfies $-1 \leqslant \lambda_2^* \leqslant 1$, the two extreme values being reached when $\lambda_2 = \lambda_3$ ($\lambda_2^* = -1$) and when $\lambda_2 = \lambda_1$ ($\lambda_2^* = 1$). Figure 20(*b*) shows the relative distribution of λ_2^*. Remarkably, all the curves shown in figure 20 for different flows superpose extremely well. There is almost perfect superposition of the PDFs in figure 20(*b*). This provides another piece of evidence for the universality of the properties of the velocity gradient in the flow. More specifically, figure 20(*b*) shows that the quantity λ_2^* is predominantly positive, which confirms the observation that $\langle S_{ij} S_{jk} S_{ki} \rangle < 0$. Additionally, the distribution of λ_2^* shows a clear maximum at $\lambda_2^* \approx 0.5$. This corresponds to a ratio of approximately $\lambda_2/\lambda_1 \approx (1/3)$ (Ashurst *et al.* 1987). From the PDF shown in figure 20(*b*), it is straightforward to determine the average values of λ_2^*, which are approximately constant: $\langle \lambda_2^* \rangle \approx 0.291$ (see also table II in Buaria *et al.* 2020*a*), essentially independent of Re_λ and to a large extent of the flow considered.

Table 4 list the expectations of $\langle \lambda_\alpha \rangle \tau_K$, $\langle \lambda_\alpha^2 \rangle \tau_K^2$ and $\langle \lambda_\alpha (\boldsymbol{e}_\alpha \cdot \hat{\boldsymbol{\omega}})^2 \rangle$, with the latter being the contribution of the αth eigendirection of strain to vortex stretching, as can be seen from (7.5). All quantities listed in table 4 have been made dimensionless by τ_K and correspond to HIT flows, over a range of Reynolds numbers from $Re_\lambda = 140$ to $Re_\lambda = 1300$. Interestingly, table 4 reveals that the values of $\langle \lambda_\alpha^2 \rangle \tau_K^2$ are essentially constant

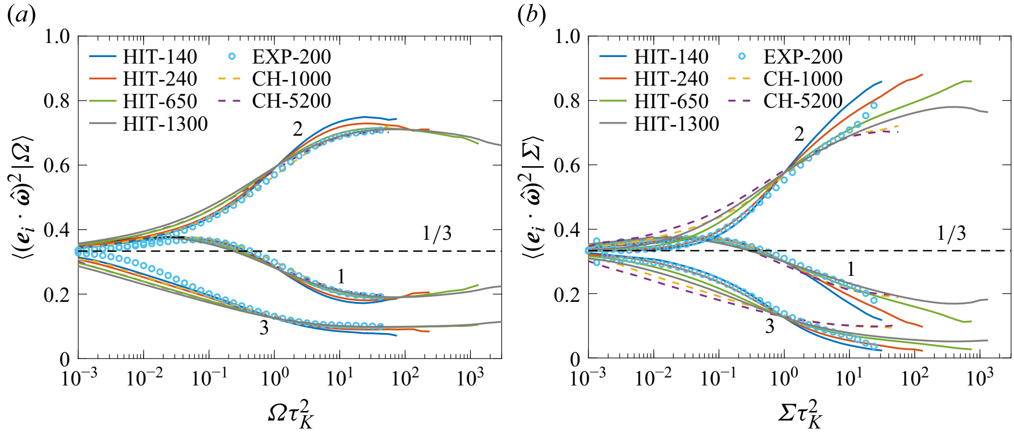

Figure 21. Conditional expectation of second moment of alignment cosines between vorticity and eigenvectors of strain, conditioned on (*a*) Ω, and (*b*) Σ. The horizontal dashed line at 1/3 marks the expectation for a uniform distribution of the alignment cosine. Figure adapted from Buaria & Pumir (2025).

over the range of values of Re_λ considered in our work (note that $\sum_\alpha \langle \lambda_\alpha^2 \rangle \tau_K^2 = (1/2)$). In comparison, the averaged values $\langle \lambda_\alpha \rangle \tau_K$ all slightly decrease in absolute values when Re_λ increases. On the other hand, the contributions to stretching from the three eigendirections of strain, $\langle \lambda_\alpha^2 (\boldsymbol{\omega} \cdot \boldsymbol{e}_\alpha)^2 \rangle \tau_K^3$, increase with Re_λ. We notice that the contribution of the largest strain eigenvalue is actually larger than the contribution of the intermediate strain eigenvalue: $\langle \lambda_1 (\boldsymbol{\omega} \cdot \boldsymbol{e}_1)^2 \rangle > \langle \lambda_2 (\boldsymbol{\omega} \cdot \boldsymbol{e}_2)^2 \rangle$. This is a result of the significantly larger value of $\langle \lambda_1 \rangle \tau_K$ compared with $\langle \lambda_2 \rangle \tau_K$, which compensates for the preferential alignment of $\boldsymbol{\omega}$ with $\boldsymbol{e}_2$ (Tsinober 2009; Buaria *et al.* 2020*a*).

7.2. *Conditional statistics*

The analysis presented in the previous subsection was based on unconditional statistics determined over the entire field. To get further insight into the nonlinear amplification acting on regions where vorticity or strain are very large, we now consider the averages of the various local quantities relevant to vortex and strain amplification, conditioned on $\Omega \tau_K^2$. To study vortex stretching conditioned on strain and vorticity, our starting point is (7.5), which clearly shows the role of both the alignment between $\hat{\boldsymbol{\omega}}$ and $\boldsymbol{e}_i$, and of the eigenvalues λ_i.

Figure 21 shows the alignment between vorticity and the strain eigenvectors $\boldsymbol{e}_i$, conditioned on $\Omega\ \tau_K^2$ (panel *a*) and on $\Sigma \tau_K^2$ (panel *b*), from various flows. We recall that a random orientation between $\hat{\boldsymbol{\omega}}$ and $\boldsymbol{e}_i$ implies $\langle (\hat{\boldsymbol{\omega}} \cdot \boldsymbol{e}_i)^2 \rangle = 1/3$. Consistent with figure 20, the numerical results confirm the preferential alignment between $\hat{\boldsymbol{\omega}}$ and $\boldsymbol{e}_2$. However, this preferential alignment between these two vectors is observable primarily when $\Omega \tau_K^2$ or $\Sigma \tau_K^2$ are much larger than 1; for small values of $\Omega \tau_K^2$ and $\Sigma \tau_K^2$, no particular alignment is observed. Figure 21 also shows that, as expected, the alignment between vorticity and the most compressible eigendirection of strain is very weak. More surprisingly, figure 21 also reveals a slight tendency of vorticity to be perpendicular to the most stretching eigendirection, $\boldsymbol{e}_1$, even when $\Omega \tau_K^2 \gg 1$. We observe at most a very moderate effect of Re_λ. The differences between the different flows considered are also very small.

Figure 22 shows the expectation of the first two eigenvalues of strain, λ_1 and λ_2, made dimensionless by τ_K, and conditioned on $\Omega \tau_K^2$ (panel *a*) and on $\Sigma \tau_K^2$ (panel *b*). The average values of the two eigenvalues, conditioned on Ω and Σ, are positive; the average

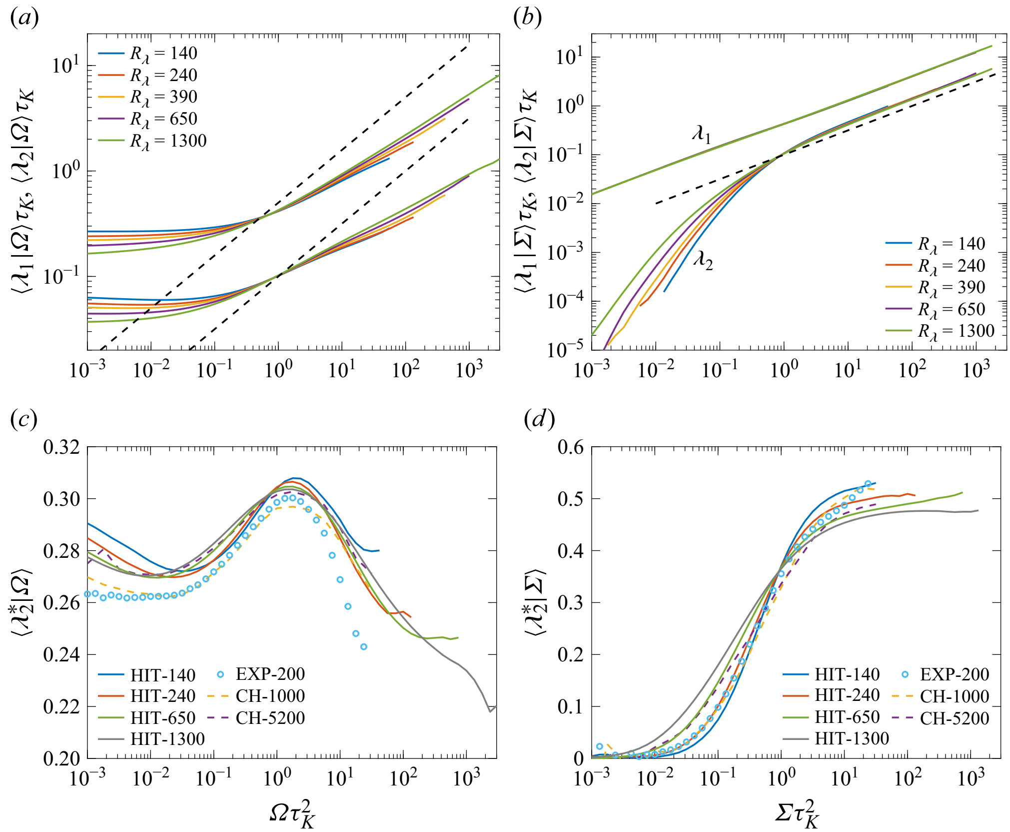

Figure 22. Conditional expectations of the first two eigenvalues of strain λ_1 and λ_2, conditioned on (*a*) Ω, and (*b*) Σ, for various Re_λ. The black dashed lines correspond to slope 1/2. Conditional expectation of the quantity λ_2^*, as defined in (7.6), conditioned on (*c*) Ω and (*d*) Σ. Panel a adapted from Buaria *et al.* (2020*a*) and panel *b* from Buaria, Pumir & Bodenschatz (2022). Panels c and d adapted from Buaria & Pumir (2025).

of the third eigenvalue, λ_3, can simply be deduced from the identity $\lambda_3 = -(\lambda_1 + \lambda_2)$. The value of $\langle \lambda_1 | \Omega \rangle$ grows slower than $\Omega^{1/2}$, shown by the dashed line, when $\Omega \tau_K^2 \gg 1$, consistent with the observation that strain $\langle \Sigma | \Omega \rangle$ itself grows slower than Ω. We observe that the ratio $\langle \lambda_1 | \Omega \rangle / \langle \lambda_2 | \Omega \rangle \sim 5{-}6$ over essentially the entire range of values of $\Omega \tau_K^2$ shown in figure 22(*a*). Alternatively, the average of λ_2^*, conditioned on Ω, see figure 22(*c*) varies only mildly with Ω in the range $0.26 \lesssim \lambda_2^* \lesssim 0.31$, consistent with a ratio $\langle \lambda_2 | \Omega \rangle / \langle \lambda_1 | \Omega \rangle \approx 5{-}6$ (Buaria *et al.* 2020*a*). In contrast, the mean values of λ_1 and λ_2 conditioned on Σ show a significantly different behaviour. Namely, figure 22(*b*) shows that $\langle \lambda_1 | \Sigma \rangle$ behaves as $\Sigma^{1/2}$ over the entire range of $\Sigma \tau_K^2$ studied. The intermediate eigenvalue, $\langle \lambda_2 | \Sigma \rangle$ is very small for $\Sigma \tau_K^2 \lesssim 0.1$, and grows as $\Sigma^{1/2}$, and is approximately 1/3 of $\langle \lambda_1 | \Sigma \rangle$ when $\Sigma \tau_K^2 \gtrsim 1$. This is confirmed by figure 22(*d*), which shows that $\langle \lambda_2^* | \Sigma \rangle$ strong changes from $\langle \lambda_2^* | \Sigma \rangle \approx 0$ when $\Sigma \tau_K^2 \to 0$, and $\to 1/2$ when $\Sigma \tau_K^2 \to \infty$.

Figure 23(*a*) shows the enstrophy production term conditioned on Ω, $\langle \omega_i S_{ij} \omega_j | \Omega \rangle$, while figure 23(*b*) shows the enstrophy production term $\langle (\omega_i S_{ij} \omega_j | \Sigma \rangle$, as well as the strain self-amplification term $-\langle S_{ij} S_{jk} S_{ki} | \Sigma \rangle$. In both panels, we have compensated the conditional enstrophy production term by the conditioning variable. Consistent with the observation that the strain intensity, $\langle \Sigma | \Omega \rangle$ grows slower than linearly with Ω, figure 23(*a*) shows that the dependence of $\langle \omega_i S_{ij} \omega_j | \Omega \rangle$ is slower than $\Omega^{1/2}$, shown as

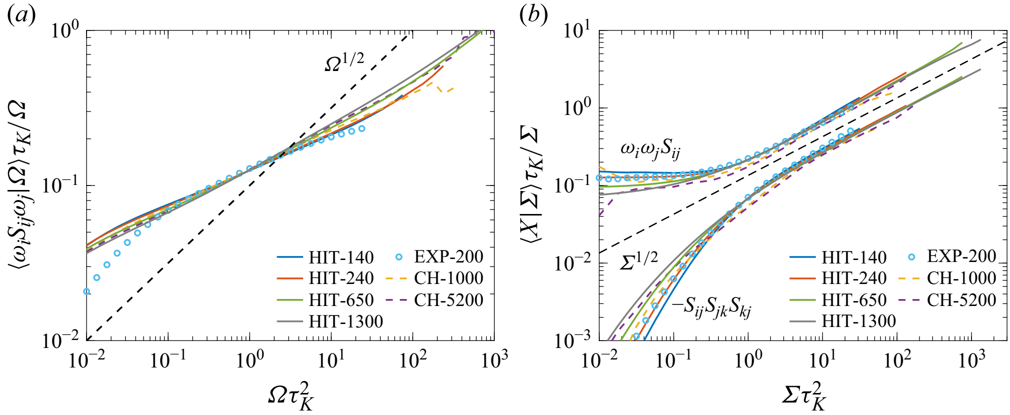

Figure 23. (*a*) Conditional expectation of the enstrophy production term, conditioned on Ω. (*b*) Conditional expectation of the enstrophy production and strain self-amplification terms conditioned on Σ. For clarity, the terms have been compensated by the conditioning variable. The black dashed line in each panel corresponds to a power law of 1/2, as expected from a purely dimensional scaling. Figure adapted from Buaria & Pumir (2025).

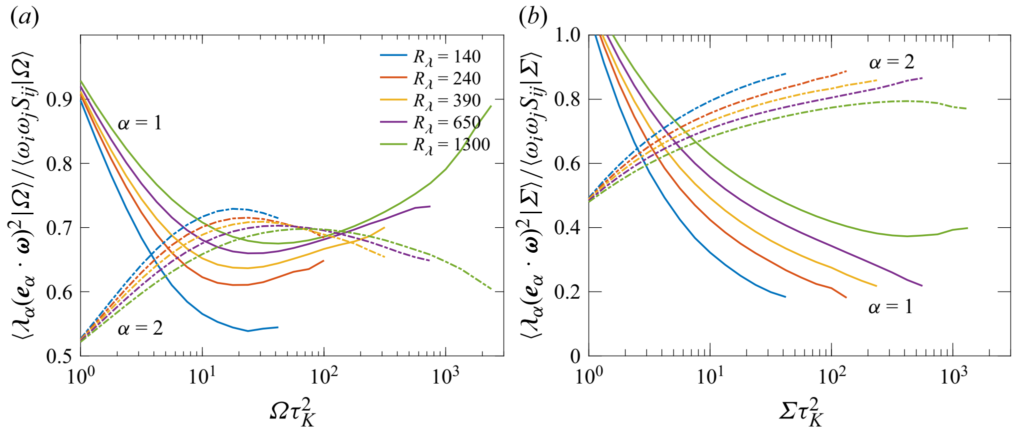

Figure 24. The fractional contributions from each eigendirection to the net production of enstrophy at various Re_λ, conditioned on a) Ω, and b) Σ. Solid and dashed lines correspond to $\alpha = 1$ and 2, respectively. Panel (*a*) is adapted from Buaria *et al.* (2020*a*) and panel (*b*) from Buaria *et al.* (2022).

a dashed line. The dependence is close to, but differs from, a power law. The curves corresponding to the channel flows at $Re_\tau = 1000$, respectively $Re_\tau = 5200$, are very close to those corresponding to HIT at $Re_\lambda = 240$, respectively $Re_\lambda = 650$, consistent with the comparisons discussed in § 5.4. In a similar spirit, figure 23(*b*),the two conditional averages have been divided by Σ. Both quantities grow as $\Sigma^{1/2}$ when $\Sigma \tau_K^2 \gtrsim 1$.

Figure 24 shows the relative contribution of the eigenvalues of strain to vortex stretching, following (7.5), conditioned on Ω (panel *a*) and on Σ (panel *b*). The preferential alignment of vorticity with the intermediate eigenvalue of strain may suggest that the main contribution to stretching originates primarily from $\boldsymbol{e}_2$. However, the large value of the ratio $\langle \lambda_1 | \Omega \rangle / \langle \lambda_2 | \Omega_2 \rangle \sim 6$ when $\Omega \tau_K^2 \gg 1$ ensures that the contributions of the two largest eigenvectors of strain to vortex stretching are actually comparable when $\Omega \tau_K \gg 1$. This is evident from figure 24(*a*). In comparison, in figure 24(*b*), the contribution to vortex

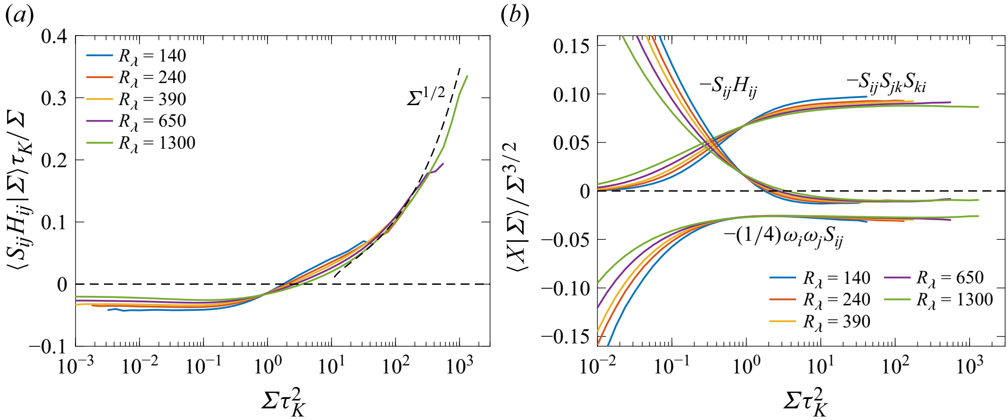

Figure 25. Conditional expectations on Σ of (*a*) strain and pressure-Hessian correlation, and b) various nonlinear (inviscid) terms on the right-hand side of (7.2). In panel *a*, the dashed black line corresponds to $0.01\ \Sigma^{3/2}$. In panel *b*, all curves have been compensated by $\Sigma^{3/2}$ revealing a plateau for $\Sigma\tau_K^2 > 1$. Figure adapted from Buaria *et al.* (2022).

stretching, conditioned on Σ due to $\boldsymbol{e}_1$ is smaller than the contribution due to $\boldsymbol{e}_2$ for large values of $\Sigma\tau_K^2$. This is a consequence of the stronger value of λ_2/λ_1 when $\Sigma\tau_K^2 \gg 1$.

7.3. *Role of pressure on strain amplification*

As clearly shown by (7.2), strain amplification is affected by non-local effects due to the pressure Hessian through the term $S_{ij}H_{ij}$ in (7.2). We recall that the average contribution due to pressure in (7.2), $\langle S_{ij}H_{ij}\rangle$, is 0 in a homogeneous flow. This leads to the identity $(\mathrm{D}\Sigma/\mathrm{D}t) = 2\langle\omega_i\omega_j S_{ij}\rangle > 0$ (up to viscous terms), which implies that $\Sigma = 2(\lambda_1^2 + \lambda_2^2 + \lambda_3^2)$ is also amplified by the nonlinear terms in the INSE.

Although the pressure-Hessian term in (7.2) does not provide a net contribution to the amplification of Σ, since $\langle H_{ij}S_{ij}\rangle = 0$, the average value of $H_{ij}S_{ij}$ conditioned on strain differs from zero and therefore may contribute to the amplification of strain. This is demonstrated by figure 25(*a*), which shows the dependence of $\langle S_{ij}H_{ij}|\Sigma\rangle$, divided by Σ, as a function of $\Sigma\tau_K^2$ for HIT runs at various Reynolds numbers, as indicated in the legend. For quantities stronger than the mean ($\Sigma\tau_K^2 \gtrsim 1$), the conditional average $\langle S_{ij}H_{ij}|\Sigma\rangle$ is positive, implying that pressure provides a negative contribution to the amplification of strain (due to the negative sign in (7.2)), i.e. it rather attenuates the growth of Σ. Interestingly, we observe that $\langle S_{ij}H_{ij}|\Sigma\rangle/\Sigma \sim \Sigma^{1/2}$ for large values of $\Sigma\tau_K^2$.

As the average $\langle H_{ij}S_{ij}\rangle = 0$, the conditional average of $H_{ij}S_{ij}$ has to change sign: the non-local effect of pressure leads to a redistribution of strain fluctuations towards the mean amplitude. Figure 25(*b*) compares the effect of the three inviscid terms on the right-hand side of (7.2), conditioned on Σ. All three terms have been divided by $\Sigma^{3/2}$, and show a plateau for $\Sigma\tau_K^2 \gg 1$. The dominant contribution comes from the self-amplification of strain, $S_{ij}S_{jk}S_{ki}$, the conditional value $-\langle S_{ij}S_{jk}S_{ki}|\Sigma\rangle \sim 0.089\ \Sigma^{3/2}$. In comparison, vortex stretching and the pressure Hessian both contribute negatively to the amplification of Σ: $-1/4\langle\omega_i\omega_j S_{ij}|\Sigma\rangle \sim -0.028\ \Sigma^{3/2}$ and $-\langle S_{ij}H_{ij}|\Sigma\rangle \sim -0.010\ \Sigma^{3/2}$. The sum of the three terms is positive, pointing to a nonlinear amplification by the inviscid terms. In the steady state, this amplifying effect is opposed by the action of the viscous terms.

Whereas the pressure Hessian H_{ij} plays a relatively simple role in strain amplification, it acts in a more unexpected way on the evolution of the individual eigenvalues of strain, λ_i^2.

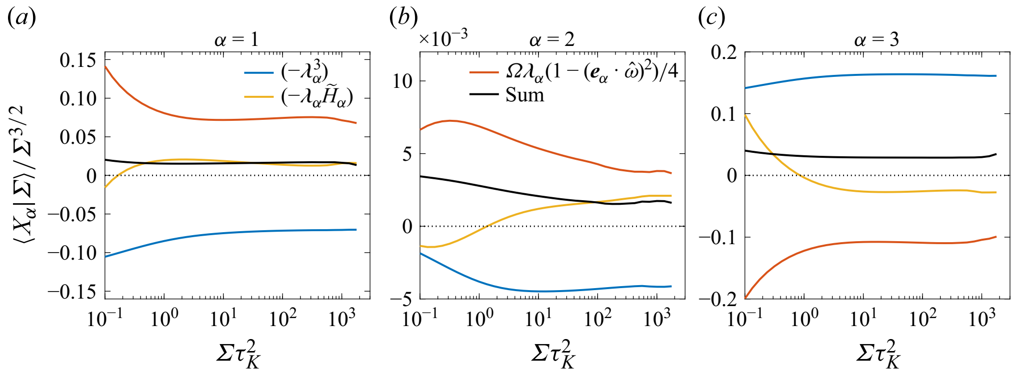

Figure 26. Conditional expectations of the various inviscid terms in (7.8) for different eigendirections of strain. All quantities are normalised by $\Sigma^{3/2}$. The legend is spread over panels *a* and *b*, but applies to all panels. Figure adapted from Buaria *et al.* (2022).

This can be seen by projecting the pressure Hessian along the eigendirections of strain, defined as $\tilde{H}_\alpha = \boldsymbol{e}_\alpha^T \boldsymbol{H}\, \boldsymbol{e}_\alpha$ for $\alpha = 1, 2, 3$ (no summation is assumed over Greek indices). This allows us to project (2.6) onto each strain eigenvector to obtain (Nomura & Post 1998)

$$\frac{\mathrm{D}\lambda_\alpha}{\mathrm{D}t} = -\lambda_\alpha^2 + \frac{\Omega}{4}\left[1 - (\boldsymbol{e}_\alpha \cdot \hat{\boldsymbol{\omega}})^2\right] - \tilde{H}_\alpha + \text{viscous terms}. \tag{7.7}$$

Multiplying (7.7) by λ_i leads to

$$\frac{1}{2}\frac{\mathrm{D}\lambda_\alpha^2}{\mathrm{D}t} = -\lambda_\alpha^3 + \frac{\Omega\lambda_\alpha}{4}\left[1 - (\boldsymbol{e}_\alpha \cdot \hat{\boldsymbol{\omega}})^2\right] - \lambda_\alpha \tilde{H}_\alpha + \text{viscous terms}. \tag{7.8}$$

Equation (7.8) indicates that the negative eigenvalue of strain, λ_3^2, is amplified by the nonlinear term since $-\lambda_3^3 > 0$, while, on the contrary, the positive eigenvalues are attenuated by the cubic term. We also notice that the term originating from vortex stretching, $1/4\Omega\lambda_i[1 - (\boldsymbol{e}_\alpha \cdot \hat{\boldsymbol{\omega}})^2]$, has the opposite sign compared with $-\lambda_\alpha^3$: vortex stretching contributes negatively to the growth of λ_3^2, and positively to the amplification of λ_1^2 and λ_2^2. To get a better understanding of the amplification of strain, one needs to fully understand not only the coupling with vorticity but also the pressure terms, the second and third terms in (7.8), respectively.

Figure 26 shows the contributions of the inviscid terms in (7.8), conditioned on the norm of strain, Σ. From left to right, the three panels respectively show the contributions corresponding to amplification of each eigenvalue. All quantities have been made dimensionless by dividing by $\Sigma^{3/2}$. Following (7.8), the sign convention used in the figure is that positive terms contribute to amplifying λ_α^2. We observe that the sums of all terms, shown in black in each panel of figure 26, are all positive, meaning that the overall effect of the nonlinearity is to amplify strain. Furthermore, as expected, the $-\lambda_\alpha^3$ term amplifies the most negative eigenvalue of $\boldsymbol{S}$, but leads to an attenuation of the intermediate eigenvalue, λ_2, and even more so of the most intense one, λ_1. For those two positive eigenvalues, λ_1 and λ_2, we observe that the vortex stretching term almost exactly cancels $-\lambda_\alpha^3$, so the sum of the three terms, for large enough values of $\Sigma\,\tau_K^2$, reduces to the contribution of the pressure term, which plays an amplifying role. The situation is different for λ_3, for which the amplifying effect of $-\lambda_3^2$ overwhelms the sum of the vorticity and pressure terms, the latter negatively contributing to the amplification of λ_3. Thus, the pressure Hessian plays an important role in the amplification of strain by

Re_λ	$\langle \omega_i \omega_j H^{\mathrm{D}}_{ij} \rangle$	$\langle \omega_i \omega_j H^{\mathrm{I}}_{ij} \rangle$	$\langle \omega_i \omega_j H_{ij} \rangle$	$\langle W_i W_i \rangle$	$\langle (\boldsymbol{e}_i^P \cdot \hat{\boldsymbol{\omega}})^2 \rangle$
140	−0.363	0.410	0.047	0.146	0.290:0.416:0.294
240	−0.483	0.549	0.066	0.180	0.292:0.418:0.290
390	−0.587	0.670	0.083	0.216	0.292:0.418:0.290
650	−0.746	0.853	0.107	0.269	0.293:0.418:0.289
1300	−1.010	1.153	0.146	0.360	0.293:0.418:0.289

Table 5. Unconditional averages of the quantities associated with correlation of vorticity and pressure Hessian, based on (7.12). All quantities were made dimensionless by the Kolmogorov time scale τ_K.

redistributing the amplification of the variances of the three eigenvalues of strain, but this effect does not provide a net contribution to the amplification of strain.

7.4. *Role of pressure on vorticity amplification*

Although the pressure Hessian does not appear explicitly in the equation describing the evolution of vorticity, its indirect effect on vorticity amplification can be assessed by writing the transport equation for the vortex stretching vector $W_i = \omega_j S_{ij}$, given as

$$\frac{\mathrm{D}W_i}{\mathrm{D}t} = -\omega_j H_{ij} + \text{viscous term}. \tag{7.9}$$

Disregarding the viscous terms, one can formally write $(\mathrm{D}W_i/\mathrm{D}t) = (D^2\omega_i/\mathrm{D}t^2)$, so the pressure Hessian appears in the second derivative of vorticity (Ohkitani & Kishiba 1995; Nomura & Post 1998). We further write the equation of evolution for the vortex stretching vector W_i as

$$\frac{\mathrm{D}\omega_i W_i}{\mathrm{D}t} = W_i W_i - \omega_i \omega_j H_{ij} + \text{viscous term}. \tag{7.10}$$

The formal solution of the Poisson equation (1.2) involves an integral formula relating P to $A_{ij}A_{ji}$. Expressing the second derivative of pressure with respect to spatial coordinates leads to an expression of the form

$$H_{ij} = H^I_{ij} + H^D_{ij} \quad \text{where} \quad H^I_{ij} = -\frac{1}{3} A_{mn} A_{nm} \delta_{ij}, \tag{7.11}$$

where H^D_{ij} is expressed as a convolution of $A_{ij}A_{ji}$ over space (Ohkitani & Kishiba 1995). We refer here to H^I and H^D as the isotropic and deviatoric contributions to the pressure Hessian, with the remark that the former is formally local, and the latter non-local, with the specific property that $H^D_{ii} = 0$. The isotropic term, which can be written as $H^I_{ij} = (1/6)(\varOmega - \varSigma)\delta_{ij}$, coincides with the RE term, already introduced in § 2. Introducing the decomposition of H_{ij} as a sum of the isotropic and deviatoric parts, (7.10) becomes

$$\frac{\mathrm{D}\omega_i\, W_i}{\mathrm{D}t} = W_i W_i - \omega_i \omega_j H^D_{ij} - \omega_i \omega_j H^I_{ij} + \text{viscous term}. \tag{7.12}$$

The role of the two components of the pressure Hessian, H^I_{ij} and H^D_{ij}, in vorticity amplification, as written on the right-hand side of (7.12), can be readily determined from DNS, by considering separately the averages $\langle \omega_i \omega_j H^{\mathrm{D}}_{ij} \rangle$ and $\langle \omega_i \omega_j H^{\mathrm{I}}_{ij} \rangle$. For HIT, the corresponding values, along with those of $\langle W_i W_i \rangle$, are listed in table 5.

Remarkably, the values of $\langle H^I_{ij} \omega_i \omega_j \rangle$ are positive, which implies that H^I_{ij} tends to attenuate vortex stretching. On the other hand, the contribution of the deviatoric term

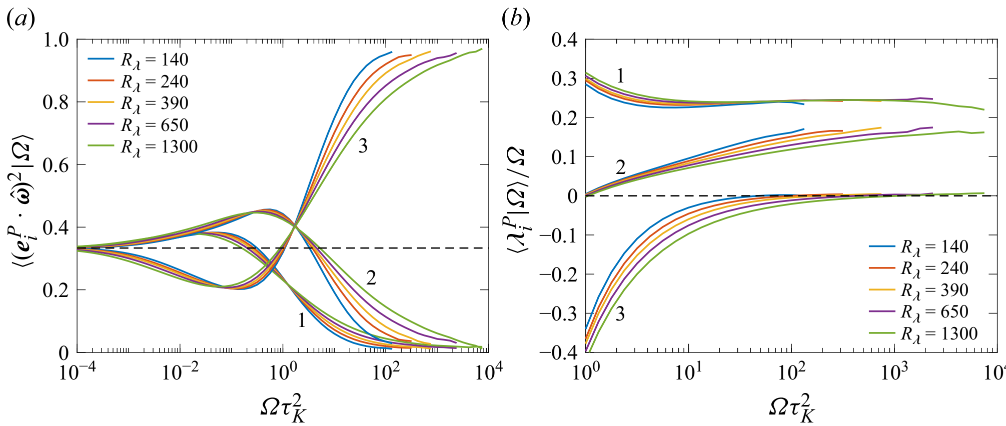

Figure 27. Conditional expectations (given enstrophy Ω), and at various Re_λ, of (*a*) the second moment of alignment cosines between vorticity and eigenvectors of pressure Hessian, and (*b*) the eigenvalues of pressure Hessian. Figure adapted from Buaria & Pumir (2023).

$\langle H_{ij}^D \omega_i \omega_j\rangle$ is always negative and therefore tends to oppose the effect of H_{ij}^{I}. Remarkably, the numerical results shown in table 5 point to a strong cancellation between the effect of H_{ij}^{I} and H_{ij}^{D}; the resulting effect of pressure $\langle H_{ij}\omega_i\omega_j\rangle$ being positive. This implies that pressure overall tends to reduce vortex stretching, It is important to notice that $\langle W_i W_i\rangle$ is large and overwhelms the inhibitory effect of pressure, therefore ensuring that the INSE dynamics generates vortex stretching in the flow.

To analyse the coupling between pressure Hessian and vorticity in (7.10), it is useful to diagonalise the pressure Hessian, H_{ij}, which is a symmetric, real matrix, and therefore has 3 real eigenvectors, λ_i^P associated with three eigenvectors, $\boldsymbol{e}_i^P$, such that $\boldsymbol{e}_i^P \cdot \boldsymbol{e}_j^P = \delta_{ij}$, where δ is the Kronecker delta tensor. As previously, we rank the eigenvalues of H_{ij} in decreasing order: $\lambda_1^P \geqslant \lambda_2^P \geqslant \lambda_3^P$. We notice that the eigenvalues of H_{ij} and H_{ij}^{I} coincide and that the average values of the eigenvalues of H_{ij} differ from those of H_{ij}^{D} by the constant quantity $A_{ij}A_{ji}$. In this text, we will focus on the eigenvalues of H_{ij}; a more complete discussion involving the eigenvalues of H_{ij}^{D} can be found in (Buaria & Pumir 2023). The investigation of the effect of the pressure Hessian on the evolution of vortex stretching, (7.10), is based on the decomposition

$$\omega_i \omega_j H_{ij} = \Omega\, \lambda_i^P\, (\hat{\boldsymbol{\omega}} \cdot \boldsymbol{e}_i^P)^2\,, \tag{7.13}$$

which is similar in spirit to (7.5). The numerical results for our HIT flows reveal that the mean values of the eigenvalues, $\langle\lambda_i^P\rangle$ scale as τ_K^{-2}, with a proportionality coefficient $\sim 0.300 : 0.025 : -0.325$ for the three eigenvalues, see (Buaria *et al.* 2022). The DNS do not reveal a very strong alignment between vorticity and the eigenvalues of H_{ij}, $\boldsymbol{e}_i^P$. This can be seen by the mean values of $\langle(\hat{\boldsymbol{\omega}} \cdot \boldsymbol{e}_\alpha)^2\rangle$ listed in table 5, which remain close to 1/3: $\sim 0.292 : 0.418 : 0.290$ for $i = 1, 2$ and 3 and only point to a mild alignment between $\hat{\boldsymbol{\omega}}$ and $\boldsymbol{e}_2^P$. As a point of comparison, the alignment between $\hat{\boldsymbol{\omega}}$ and $\boldsymbol{e}_2$ was comparatively much stronger $(\langle(\hat{\boldsymbol{\omega}} \cdot \boldsymbol{e}_2)^2\rangle \approx 0.523$. The dependence of these quantities on Re_λ is very weak.

To proceed with the study of the role of pressure in vorticity amplification using (7.10), we determined numerically the averages of $(\hat{\boldsymbol{\omega}} \cdot \boldsymbol{e}_i^P)^2$ and of λ_i^P conditioned on Ω. Figure 27(*a*) shows $\langle(\hat{\boldsymbol{\omega}} \cdot \boldsymbol{e}_i^P)^2|\Omega\rangle$ for our HIT runs, and reveals a strong alignment between $\hat{\boldsymbol{\omega}}$ and the eigenvector corresponding to the smallest eigenvector of H_{ij} – although

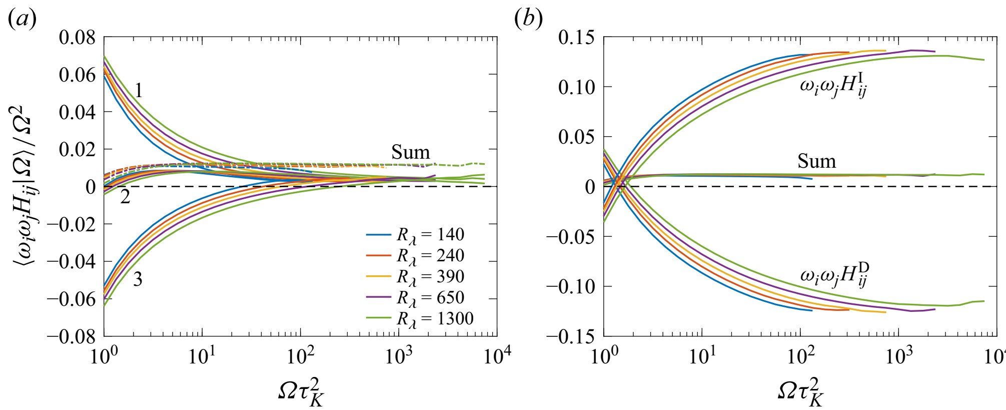

Figure 28. (*a*) Conditional expectation (given enstrophy Ω) of the term $\omega_i \omega_j H_{ij}$ (marked as sum) and the individual contributions from each eigendirection of pressure Hessian (in solid lines). (*b*) Conditional expectations (given enstrophy Ω) of the terms $\omega_i \omega_j H_{ij}^{\mathrm{I}}$ and $\omega_i \omega_j H_{ij}^{\mathrm{D}}$, as well as their sum, illustrating the large cancellation between the isotropic and deviatoric components of the pressure Hessian. All quantities are compensated by Ω^2, revealing a plateau for $\Omega \tau_K^2 \gg 1$. Figure adapted from Buaria & Pumir (2023).

this alignment is impossible to detect on the averaged quantities, such as $\langle(\hat{\boldsymbol{\omega}} \cdot \boldsymbol{e}_i^P)^2\rangle$. Furthermore, figure 27(*b*) shows the eigenvalue of the pressure Hessian, conditioned on Ω: $\langle \lambda_i^P | \Omega \rangle$. The largest eigenvalues, for $i = 1$ and 2 are positive, and are slightly negative for $i = 3$, but tend to 0 when $\Omega \tau_K^2 \gg 1$. The alignment properties, as well as the structure of the eigenvalues of H_{ij}, as shown in figure 27, can be qualitatively understood by drawing a comparison with Burgers' vortex (Burgers 1948), as also previously discussed in § 6. An elementary calculation shows that the smallest eigenvalue of H_{ij} is 0 for a Burgers' vortex, with the corresponding eigenvector being parallel to vorticity (Andreotti 1997). Evidently, the regions of intense vorticity in turbulence also demonstrate a similar behaviour (Nguyen, Laval & Dubrulle 2020; Buaria & Pumir 2023).

The resulting contributions to the amplification of vortex stretching, see (7.13), are shown in figure 28(*a*). The quantities $\langle \omega_i \omega_j H_{ij} | \Omega \rangle$ have been divided by Ω^2, which makes all the quantities shown dimensionless. We observe that all quantities are very small when $\Omega \tau_K^2 \gg 1$. Consistent with the results in figure 27, figure 28(*a*) shows that the contributions of the two largest eigenvalues of H_{ij}, λ_1^P and λ_2^P, are both positive. The contribution of the third one, λ_3^P is also very weak but appears to be slightly positive and, in fact, comparable to the contribution of the two other eigenvalues. The sum of the three contributions, shown by the dashed–dotted lines in figure 28(*a*), is positive and reaches a plateau at a small but finite value, which implies that $\langle \omega_i \omega_j H_{ij} | \Omega \rangle \sim 0.012\, \Omega^2$. This implies that the pressure Hessian opposes the growth of vortex stretching, the more so as the vorticity is more intense.

It is worth recalling the observation of table 5 that the effect of the pressure Hessian results from a strong cancellation between the isotropic part, H_{ij}^{I}, which opposes amplification, and H_{ij}^{D}, which favours it. This effect is also seen when separating the contribution of H_{ij}^{I} and H_{ij}^{D} in the term $\omega_i \omega_j H_{ij}$ conditioned on Ω, see figure 28(*b*). The cancellation is clearly visible when focusing on regions of most intense vorticity, $\Omega \tau_K^2 \gg 1$. In fact, the eigenvalues of H_{ij} are equal to the eigenvalues of H_{ij}^D, minus $A_{ij} A_{ji}/3$, whose average conditioned on Ω is equal to $\langle -A_{ij} A_{ji}/3 | \Omega \rangle = \langle \Omega(\Omega - \Sigma) | \Omega \rangle /6$. The empirical relation $\langle \Sigma | \Omega \rangle \sim \Omega^\gamma$, with $\gamma < 1$, implies that $\langle \omega_i \omega_j H_{ij}^I | \Omega \rangle / \Omega^2 \sim 1/6$ when $\Omega \tau_K^2 \to \infty$,

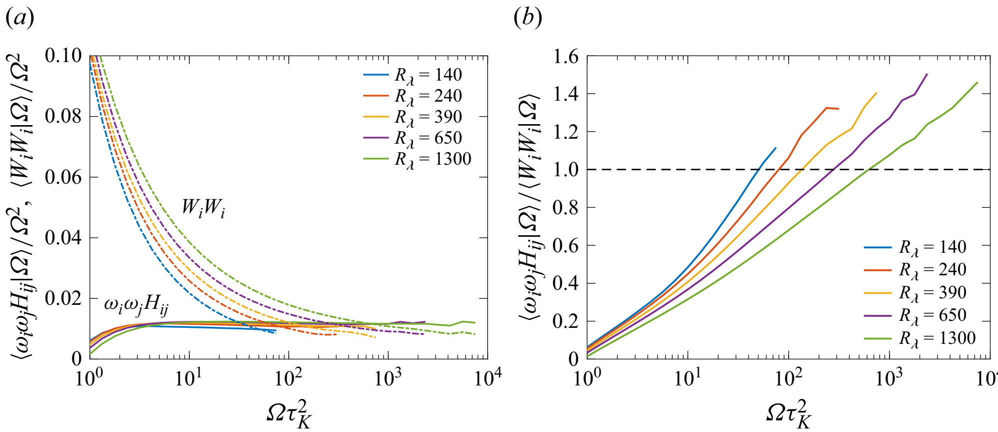

Figure 29. (*a*) Conditional expectations (given enstrophy Ω) of the nonlinear, $\langle W_i W_i|\Omega\rangle$, and pressure-Hessian contributions, $\langle \omega_i\omega_j H_{ij}|\Omega\rangle$, to the dynamics of the vortex stretching vector, as given in 7.12. (*b*) The ratio of two terms, demonstrating that the pressure-Hessian contribution overtakes the nonlinear contribution at large Ω. Figure adapted from Buaria & Pumir (2023).

a value $\gtrsim$ 10 times larger than the value found numerically for $\langle \omega_i\omega_j H_{ij}|\Omega\rangle$, see figure 28: $\langle \omega_i\omega_j H_{ij}|\Omega\rangle/\Omega^2 \approx 0.012$.

Whereas the pressure Hessian opposes amplification of vortex stretching when $\Omega\tau_K \gg 1$, the term $\boldsymbol{W}^2$ in (7.10) is positive, and therefore tends to amplify vortex stretching. This leads to a competition between the two inviscid effects. To gain further insight on the role of pressure in the dynamics leading to vortex stretching, figure 28(*a*) shows the averages of the various terms in (7.10), conditioned on Ω (Buaria & Pumir 2023): $\langle W_i W_i|\Omega\rangle$ (dashed lines) and $\langle \omega_i\omega_j H_i\, j|\Omega\rangle$ (full lines). Both quantities have been compensated by Ω^2, making them dimensionless. Figure 29(*a*) shows that $\langle W_i W_i|\Omega\rangle/\Omega^2$ is a decreasing function of Ω. This can be understood by writing $W_i W_i = \omega_i S_{ij} S_{jk}\omega_k$, and noticing that the strain grows slower than Ω in regions of intense vorticity, $\langle \Sigma|\Omega\rangle \sim \Omega^\gamma$, with $\gamma < 1$.

On the other hand, $\langle \omega_i\omega_j H_{ij}|\Omega\rangle/\Omega^2$ tends to a constant value when $\Omega\tau_K^2 \gg 1$. As a result, the positive term $W_i W_i$ in (7.10) eventually becomes smaller than $\omega_i\omega_j H_{ij}$, so the expectation $(\langle W_i W_i - \omega_i\omega_j H_{ij})|\Omega\rangle$ becomes negative when $\Omega\tau_K^2$ becomes large enough. To better illustrate the effect, the ratio between the pressure term and $\langle W_i W_i|\Omega\rangle$ is shown in the inset of figure 29(*b*): The ratio becomes larger than 1 when the vorticity is sufficiently intense, above a threshold value for $\Omega\tau_K^2$, which depends on Re_λ. Our numerical results therefore show that the pressure term dominates in regions where vorticity is most intense, i.e. for $\Omega\tau_K^2$. This suggests the existence of an inviscid mechanism, due to the non-local effect of pressure, which ultimately opposes amplification of vorticity in regions where Ω is the most intense. We will discuss a mechanism leading to attenuation of vortex amplification induced by non-local effects more thoroughly in the next section.

8. Non-locality

The analysis in § 7 focused on gradient dynamics from a local perspective, by examining single-point statistics to understand how nonlinear terms amplify vorticity and strain at a given point. We also analysed the role of pressure (Hessian) on gradient amplification, noting that its deviatoric part encapsulates the cumulative influence of non-local effects.

Nevertheless, this treatment was still local in scope, in the sense that only single-point statistics of pressure Hessian were taken into consideration. Given the inherent multiscale nature of turbulence, a true and complete picture of non-locality requires examining how gradient amplification is influenced by flow structures at different distances and scales.

In § 7, we investigated how vorticity undergoing amplification at any point is locally stretched or compressed by the strain and pressure (Hessian) at the same location. However, given that the entire gradient field is non-locally coupled, a key aspect to understand is how amplification at one point is shaped by the surrounding flow configuration. This requires moving beyond a local description and considering how amplification at one location depends on another separated by some distance R, representing the influence of an eddy of size R. To that end, we adopt a complementary framework that bypasses the explicit use of the pressure field and utilises the Biot–Savart relation to directly determine strain from the vorticity field. From a phenomenological standpoint, such non-local coupling is already implicit in classical structure function analysis, where the longitudinal and transverse increments encode interactions between scales and contribute to the energy cascade. Here, however, we seek to examine non-locality more explicitly in the context of gradient dynamics, which may be regarded as the dynamical counterpart to the cascade picture.

8.1. *Local and non-local strain*

Starting from the definition $\boldsymbol{\omega} = \nabla \times \boldsymbol{u}$, and taking its curl, we obtain: $\nabla \times \boldsymbol{\omega} = \nabla(\nabla \cdot \boldsymbol{u}) - \nabla^2 \boldsymbol{u}$, which after using the incompressibility condition gives the following Poisson equation in $\boldsymbol{u}$:

$$\nabla^2 \boldsymbol{u} = -\nabla \times \boldsymbol{\omega} \,. \tag{8.1}$$

The solution to this equation is given by the Biot–Savart relation

$$\boldsymbol{u}(\boldsymbol{x}) = \frac{1}{4\pi} \int_{\Lambda} \frac{\boldsymbol{r}}{|\boldsymbol{r}|^3} \times \boldsymbol{\omega}(\boldsymbol{x}+\boldsymbol{r}) \, \mathrm{d}\boldsymbol{r} \,, \tag{8.2}$$

where the integration domain Λ can be assumed to be infinite or periodic (as in the case of DNS of HIT). Taking the gradient of (8.2), one obtains (Ohkitani 1994)

$$S_{ij}(\boldsymbol{x}) = PV \int \frac{3}{8\pi} (\epsilon_{ikl} r_j + \epsilon_{jkl} r_i) \, \omega_l(\boldsymbol{x}+\boldsymbol{r}) \, \frac{r_k}{r^5} \, d^3\boldsymbol{r} \,, \tag{8.3}$$

which gives a direct non-local expression for the strain tensor in terms of entire vorticity field. The above integral essentially couples all the scales and provides an alternative means to understand the non-locality of gradient amplification, without involving the pressure field.

The Biot–Savart formulation also emphasises that the dynamics of incompressible turbulence can be entirely described by the vorticity equation (given in (2.5)), which also does not involve the pressure field. Indeed, this perspective has been central in the mathematical literature (Doering 2009). From this viewpoint, the central quantity governing small-scale dynamics is the vortex stretching vector ($W_i = \omega_j S_{ij}$), the strain being prescribed by (8.3). Although the Biot–Savart integral is analytically intractable, it can be directly evaluated from DNS data, allowing quantitative analysis of how vorticity amplification is influenced by the surrounding vorticity field across multiple scales.

To analyse the degree of non-locality with respect to a scale size R, the integration domain in (8.3) is separated into a spherical neighbourhood of radius $r \leqslant R$ and the remaining outer domain (Hamlington *et al.* 2008*b*; Buaria *et al.* 2020*b*)

$$S_{ij}(\boldsymbol{x}) = \underbrace{\int_{r>R} [\cdots]\, d^3\boldsymbol{x}'}_{=S_{ij}^{NL}(\boldsymbol{x},R)} + \underbrace{\int_{r\leqslant R} [\cdots]\, d^3\boldsymbol{x}'}_{=S_{ij}^{L}(\boldsymbol{x},R)} . \tag{8.4}$$

Here, S_{ij}^{NL} represents the non-local strain acting at $\boldsymbol{x}$, induced by vorticity at distances $r > R$ from the point, and S_{ij}^{L} is the local strain induced in the neighbourhood ($r \leqslant R$) of the vorticity at $\boldsymbol{x}$. One can loosely interpret S_{ij}^{NL} as the background strain responsible for vortex stretching, whereas S_{ij}^{L} reflects the locally induced strain in response to stretching – which can further self-amplify or attenuate vorticity.

Although vorticity and strain fields are directly accessible in DNS, explicitly evaluating the integrals in (8.4) is computationally expensive (and also error prone due to grid data being available on a Cartesian grid). Instead, as shown in Buaria *et al.* (2020*b*), the non-local strain can be efficiently obtained for any R by applying a transfer function to the total strain in Fourier space

$$\hat{S}_{ij}^{NL}(\boldsymbol{k},\, R) = f(kR)\ \hat{S}_{ij}(\boldsymbol{k}), \quad \text{where} \quad f(kR) = \frac{3\,[\sin(kR) - kR\cos(kR)]}{(kR)^3}, \tag{8.5}$$

where $(\hat{\cdot})$ denotes the Fourier coefficient and $\boldsymbol{k}$ is the wave vector. Incidentally, the transfer function $f(kR)$ corresponds to the 3-D sinc function, which is the Fourier transform of a box or top-hat filter. Consequently, the non-local strain is equivalent to the spatially filtered or locally averaged strain tensor over a sphere of radius R (see also Buaria & Sreenivasan 2022*a*). Since the DNS of isotropic turbulence is performed using the Fourier spectral method, obtaining the non-local strain for any value of R is straightforward. Therefore, the results presented in this section are again based on DNS of HIT.

Before analysing the role of non-local, and local, strain in vorticity amplification, it is instructive to first examine their dependence on scale size R. Figure 30 shows their square-norm, as a function of R, with all quantities non-dimensionalised by τ_K. The solid (red) lines correspond to $Re_\lambda = 1300$ and the dashed (blue) lines correspond to $Re_\lambda = 140$. The numerical results demonstrate that the dependence on the Reynolds number is very weak. From their definitions, it is evident that for $R = 0$: $\boldsymbol{S}^{NL} = \boldsymbol{S}$ and $\boldsymbol{S}^{L} = \boldsymbol{0}$, whereas for $R \to \infty$: $\boldsymbol{S}^{NL} = \boldsymbol{0}$ and $\boldsymbol{S}^{L} = \boldsymbol{S}$. Accordingly, the non-local strain decays monotonically from unity at $R = 0$ to zero as R increases, with local strain doing the opposite. Note that

$$S_{ij}S_{ij} = S_{ij}^{NL}S_{ij}^{NL} + S_{ij}^{L}S_{ij}^{L} + 2S_{ij}^{NL}S_{ij}^{L}. \tag{8.6}$$

The mean of the cross-correlation term, shown in the inset of figure 30, vanishes at $R = 0$ and ∞, but remains finite and non-zero at any intermediate R – with a maximum around $R \simeq 8\eta_K$. A similar scale is obtained from the cross-over of two curves in the main plot of figure 30. As suggested in Hamlington *et al.* (2008*a*), this scale can be loosely interpreted as the characteristic radius of the vortex tubes, consistent with the earlier analysis of Jiménez *et al.* (1993). As discussed next, a direct analysis of the vortex stretching can be performed using non-local strain to identify the size of vortical structures corresponding to extreme events.

8.2. *Non-locality of vortex stretching*

To investigate the role of non-local (and local) strain in the amplification of vorticity, we perform here an analysis similar to that done in § 7, considering the quantities relevant

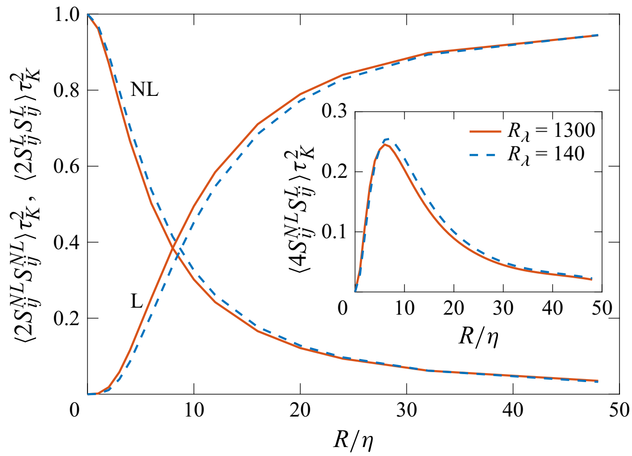

Figure 30. The square norms of the local and non-local contributions of strain, normalised by τ_K^2, at $Re_\lambda = 140$ (dashed line) and $Re_\lambda = 1300$ (full lines). The inset shows the cross-correlation term $4\langle S_{ij}^{NL} S_{ij}^{L}\rangle$. Note that all three terms add to unity by definition.

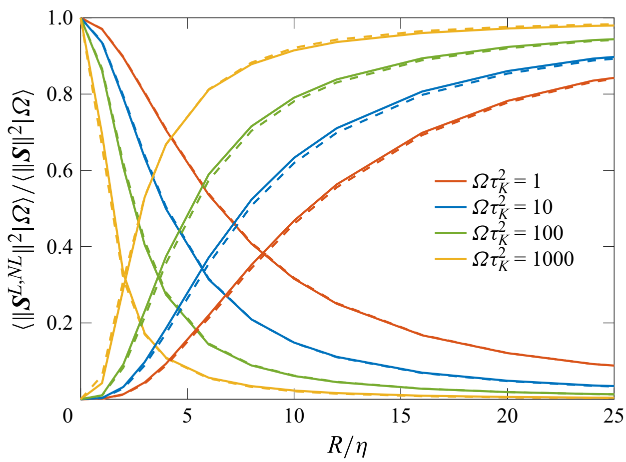

Figure 31. Conditional expectation of the square-norm of the local (L) and non-local (NL) strain, normalised by the corresponding expectation of total strain, as a function of R/η, at $Re_\lambda = 1300$ (solid lines) and $Re_\lambda = 650$ (dashed lines). Figure adapted from Buaria & Pumir (2021).

to the dynamics of vorticity conditioned on Ω. Additionally, we now also consider the explicit dependence on the spatial scale R. Extending the result shown in figure 30, figure 31 shows the dependence of the norms of the local and non-local components of strain as a function of R/η, conditioned on enstrophy with $\Omega\tau_K^2$ ranging from 1 to 1000, as indicated by the legend. Each quantity is normalised by the corresponding conditional expectation of the total strain, constraining the curves between 0 and 1 as before. The result for $\Omega\tau_K^2 = 1$ is similar to the unconditional result shown in figure 30. However, as Ω increases, we observe a faster decay (rise) for non-local (local) strain, such that the characteristic distance, say $R^*(\Omega)/\eta_K$, at which they intersect, decreases with increasing Ω. If this intersection is interpreted as a characteristic vortex radius, it follows that regions of stronger vorticity correspond to thinner, more localised vortex tubes (which is consistent with the observations in figure 2).

To further assess the efficacy of vortex stretching, we examine the alignment of vorticity within the eigenframe of non-local and local strain. The same notation is used as before to identify the respective eigenframes, with appropriate superscripts NL and L for non-local and local strain, respectively. We extract the second moment of the directional cosines: $\langle(\boldsymbol{e}_i^{\mathrm{L},NL} \boldsymbol{\cdot} \hat{\boldsymbol{\omega}})^2\rangle$, to quantify the alignments between vorticity and the eigenvectors of non-local/local strain. Note that these moments are individually bounded between 0 and 1 (with $1/3$ corresponding to uniform distribution), and also that their combined sum is unity, i.e. $\sum_{i=1}^{3}(\boldsymbol{e}_i^{\mathrm{L},NL} \boldsymbol{\cdot} \hat{\boldsymbol{\omega}})^2 = 1$.

Figure 32 shows the second moment of directional cosines as a function of scale size R/η_K, conditioned on $\varOmega\tau_K^2$. Panels (*a*) and (*b*) correspond to alignments for non-local and local strain, respectively, for $\varOmega\tau_K^2 = 1$. Focusing first on figure 32(*a*), we observe that at $R = 0$ (where $\boldsymbol{S}^{NL} = \boldsymbol{S}$), the well-known result is recovered: vorticity preferentially aligns with the intermediate (second) eigenvector and tends to be orthogonal to the most compressive (third) eigenvector. However, as R/η_K increases, the alignment of vorticity with the most extensive (first) eigenvector $\boldsymbol{e}_1^{NL}$ strengthens, while that with the intermediate one (second) weakens. The two become equal at $R/\eta_K \approx 10$, beyond which vorticity increasingly aligns with $\boldsymbol{e}_1^{NL}$, whereas its alignment with $\boldsymbol{e}_2^{NL}$ tends towards the uniform limit of $1/3$.

Next, looking at figure 32(*b*), we observe that vorticity preferentially aligns with the second eigenvector of local strain $\boldsymbol{e}_2^{L}$, for small R/η_K. (Note that the eigenframe of local strain is not defined for $R = 0$.) As R/η_K increases, this preferential alignment remains n-early constant, and the known result for total strain recovered for large R/η_K. Interestingly, for small R/η_K, vorticity appears somewhat more orthogonal to $\boldsymbol{e}_1^{L}$, with a switch to $\boldsymbol{e}_3^{L}$ occurring around the same distance as the switch for non-local strain in figure 32(*a*).

The alignment results for $\varOmega\tau_K^2 = 100$ are shown in figure 32(*c*–*d*), and for $\varOmega\tau_K^2 = 1000$ in figure 32(*e*,*f*). In these cases, similar trends are observed, although alignment tendencies become increasingly pronounced with higher $\varOmega$. Consequently, the characteristic distance at which the preferential alignment of vorticity switches from the second to the first eigenvector of $\boldsymbol{S}^{NL}$ occurs (as seen in figure 32*a*,*c*,*d*) decreases systematically with increasing $\varOmega$ – consistent with the trend observed in figure 31.

The above results indicate that vorticity is predominantly stretched by non-local strain in a manner similar to passive material lines, with vorticity preferentially aligning with the most extensive eigenvector. However, in response to this stretching, the locally induced strain in the vicinity of these vortices acts to reorient the vorticity towards the intermediate eigenvector, effectively moderating the stretching. Since vortex stretching is the mechanism through which small scales are produced in the flow, the observation that vortex stretching is mainly driven by non-local strain suggests an intriguing parallel to triadic energy transfers in spectral space, where the energy transfers are local, but mediated non-locally by large scales (Domaradzki & Rogallo 1990). However, it is worth noting that triadic interactions only describe an averaged, mode-based view of energy cascade, whereas the present framework captures the spatial structure and dynamics of extreme events, which are directly responsible for intermittency.

Figures 31 and 32 allowed us to identify a characteristic distance $R^*(\varOmega)/\eta_K$, decreasing with increasing $\varOmega$. This distance can be related to the size of vortex tubes associated with a given enstrophy, $\varOmega$. The connection can be made very explicit by revisiting our earlier analysis in § 6. In (6.10), we established a relation between the size (radius) of a vortex, η, and its enstrophy. Recasting η in (6.10) as $R^*(\varOmega)$ yields

$$R^*/\eta_K \simeq (\varOmega\tau_K^2)^{-\gamma/4}, \tag{8.7}$$

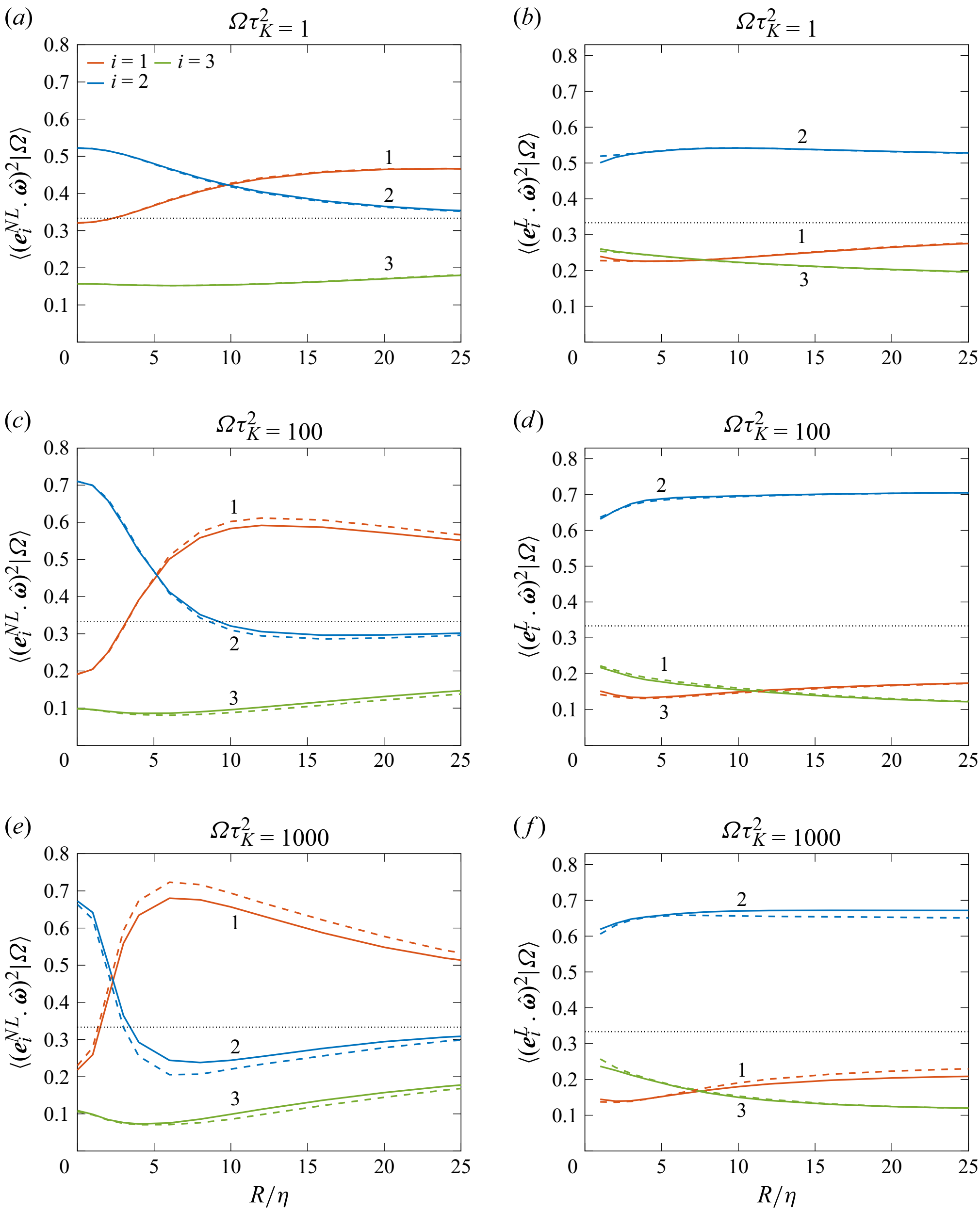

Figure 32. The conditional second moments of the alignment cosines between $\hat{\omega}$ and the eigenvectors of the local (L) and non-local (NL) strain tensors at $Re_\lambda = 1300$ (solid lines) and 650 (dashed lines), conditioned on the three value of enstrophy: $\Omega/\langle\Omega\rangle = 1$ (panels *a* and *b*), $\Omega/\langle\Omega\rangle = 100$ (panels *c* and *d*) and $\Omega/\langle\Omega\rangle = 1000$ (panels *e* and *f*). The dotted line at 1/3 in each panel corresponds to a uniform distribution of the cosines. Figure adapted from Buaria & Pumir (2021).

where the exponent γ corresponds to the power-law dependence of the effective strain acting on vorticity: $\langle \Sigma | \Omega \rangle \sim \Omega^\gamma$.

We extract the distance R^*/η_K at which the norms of S^{NL} and S^L are identical, as seen in figure 31, and plot it as a function of $\Omega\tau_K^2$ in figure 33. Given the smaller range of Ω at

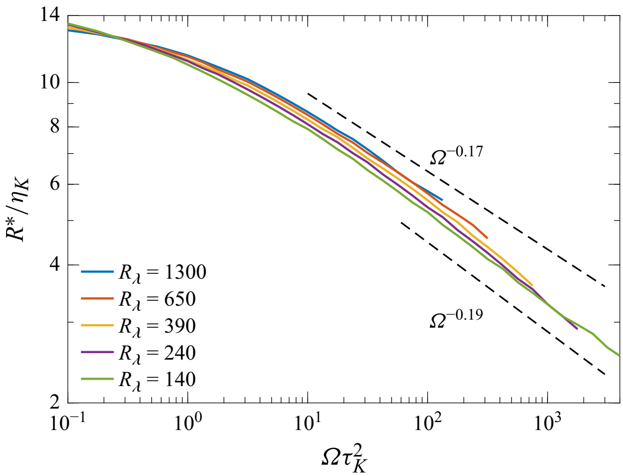

Figure 33. The critical distance R^*/η_K as a function of $\Omega/\langle\Omega\rangle$ corresponding to the distance obtained from figure 31 where magnitude of conditional local and non-local strain are equal. The black dotted line corresponds to the power law $\sim \Omega^{-0.19}$, based on (8.7), with $\gamma = 0.76$ for $Re_\lambda = 1300$.

lower Re_λ, we only show results for $Re_\lambda = 390$ to 1300. The power laws corresponding to $\gamma/4$ are also shown for the lowest and highest Re_λ. Note that $\gamma/4$ only varies from 0.17 to 0.19 for the range of Re_λ, but this small change can still be made out. More importantly, we see that the characteristic distance R^*/η_K agrees almost perfectly with the power-law prediction deduced in § 6, confirming our ansatz that it corresponds to the radius of vortex tubes. The distance at which the alignment of vorticity switches from the second to the first eigenvector of non-local strain is comparable but differs slightly from R^* (Buaria & Pumir 2021). The dependence of this length scale on Ω exhibits a much smaller range of power law, which relates to the breakdown of scale invariance. We refer the interested readers to Buaria & Pumir (2021) for details.

The conditional expectation of non-local production $P_\Omega^{NL} = \langle\omega_i\omega_j S_{ij}^{NL}|\Omega\rangle$ normalised by total production $P_\Omega = \langle\omega_i\omega_j S_{ij}|\Omega\rangle$ is shown in figure 34. For moderate conditioning values ($\Omega\tau_K^2 \simeq 1{-}10$), the normalised production term exhibits behaviour similar to that of the non-local strain term in figure 31 – it begins at unity for $R = 0$ and decreases monotonically to zero as $R \to \infty$. However, at most extreme conditioning values ($\Omega\tau_K^2 \simeq 100{-}1000$), a qualitatively different behaviour is observed, with the normalised value of P_Ω^{NL} overshooting unity at small R, before decreasing more sharply at larger R. Since $P_\Omega = P_\Omega^{NL} + P_\Omega^{L}$, the observed overshoot implies that the local production term P_Ω^{L} becomes negative for small R, and essentially counteracts the amplification of vorticity when it becomes very large. Remarkably, this suggests the existence of an inviscid self-attenuating mechanism embedded within the nonlinear term itself – one that possibly acts to limit unbounded vorticity growth. The nature and implications of this mechanism are explored in detail in the next subsection.

8.3. *Self-attenuation of extreme events*

Earlier in figure 34, we observed that the local enstrophy production term $\langle\omega_i\omega_j S_{ij}^{L}|\Omega\rangle$ becomes negative in the vicinity of large Ω. This behaviour has important implications for the dynamics of extreme vorticity events and, more broadly, for the regularity of the INSE. To provide some context, recall that the evolution of vorticity is governed by two

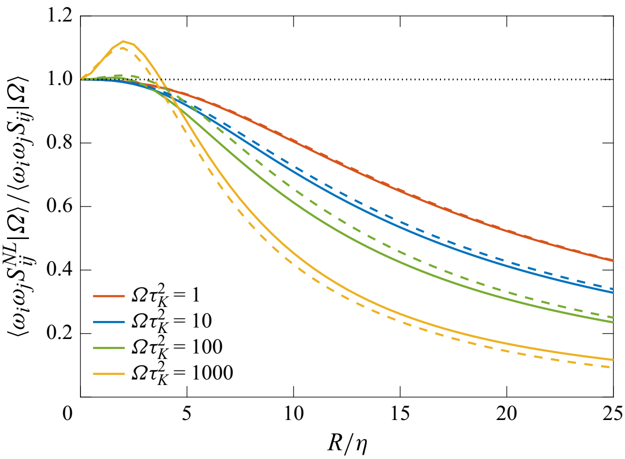

Figure 34. Dependence on R/η_K of the conditional expectation of the enstrophy production based on non-local strain, $\langle \omega_i \omega_j S_{ij}^{NL} | \Omega \rangle$, normalised by the total enstrophy production $\langle \omega_i \omega_j S_{ij} | \Omega \rangle$ at $Re_\lambda = 1300$ (solid lines) and 650 (dashed lines). Figure adapted from Buaria & Pumir (2021).

competing mechanisms: amplification through vortex stretching and attenuation through viscous diffusion. The enstrophy production term $\omega_i \omega_j S_{ij}$ quantifies the nonlinear self-amplification of vorticity, whereas the viscous term always counteracts it.

Thus, for a potential finite-time blow up of vorticity (leading to a singularity), the enstrophy production term $\omega_i \omega_j S_{ij}$ must also diverge (Beale *et al.* 1984). Since the production term can be decomposed into non-local and local contributions: $\omega_i \omega_j S_{ij} = \omega_i \omega_j S_{ij}^{NL} + \omega_i \omega_j S_{ij}^{L}$, any such blow up must originate from one of these components. However, Constantin *et al.* (1996) demonstrated that the non-local contribution can be bounded in terms of the total kinetic energy of the flow, implying that any singular behaviour must stem from the local term.

The observation in figure 34 is therefore striking: for large Ω, the local production term is negative and thus acts to attenuate vorticity. To examine this more directly, we next present a supporting visualisation. Figure 35 shows vortex tubes around one of the most extreme vorticity events in the flow, with the maxima of the enstrophy located at the centre of the domain. Panels (*a*) and (*b*) show isosurfaces of enstrophy respectively, at 100 and 1000 times the mean value corresponding to moderate and intense events, and illustrate the characteristic vortex-tube structure. Panel (*c*) shows the enstrophy field in the mid-plane slice of the domain. Figure 35(*d–f*) shows the corresponding result for the total enstrophy production, P_Ω whereas figure 35(*g-i*) shows it for the local enstrophy production term, P_Ω^L. (corresponding to $R = 2\eta$). Evidently, P_Ω is overwhelmingly positive, which is anticipated given the large enstrophy in these tubes, and also from the dynamical constraints of turbulence (Betchov 1956).

However, unlike P_Ω which is always positive for intense vorticity, the mean of P_Ω^L does not have such constraints. For moderate values shown in figure 35(*g*), we find that the volumes occupied by positive and negative values are comparable. However, for the intense value shown in figure 35(*h*), negative stretching rate is more prevalent, especially around the centre where vorticity is maximum. This is corroborated by figure 35(*i*), which shows the 2-D contour level of P_Ω^L at the mid-plane and reveals that both negative and positive values occur in the outer regions of the tubes where vorticity is not very intense, whereas large negative values occur inside the tubes, where vorticity is most intense.

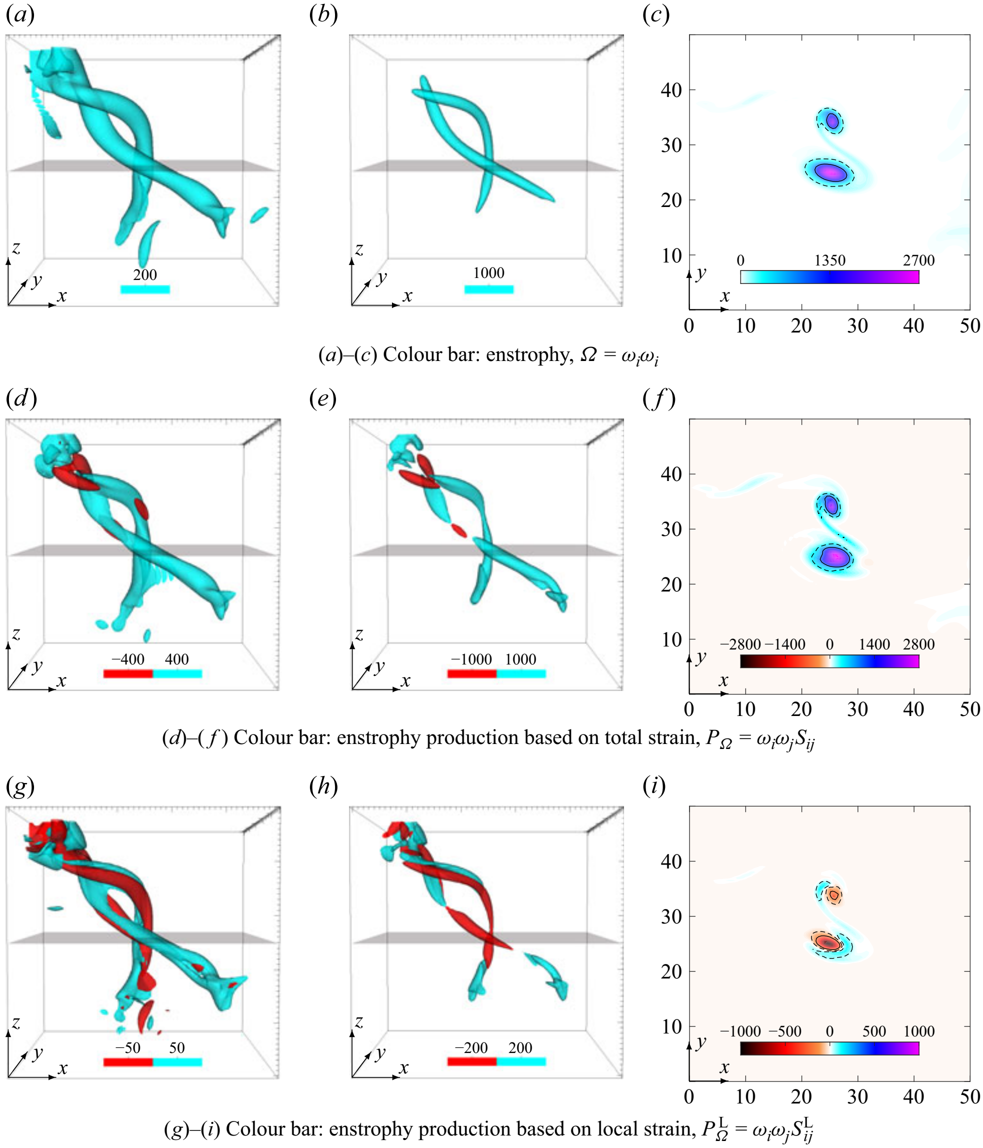

Figure 35. The panels illustrate how local stretching attenuates vortex amplification in a representative region of intense vorticity. The views are from DNS at $Re_\lambda = 650$, see table 1. The maximum enstrophy, Ω, is at the centre of the domain shown, whose edges are $50\eta_K$ in each direction (in each panel successive major ticks are 10η apart). Top row: Isosurfaces of Ω at thresholds of (*a*) 200 and (*b*) 1000 (times the mean value). (*c*) Two-dimensional contours of $\Omega\tau_K^2$ at the mid-plane of the domain, shown in grey in (*a*) and (*b*). Middle row: enstrophy production based on total strain, P_Ω, suitably non-dimensionalised by mean of enstrophy, at thresholds of (*d*) ±400, and (*e*) ±1000, which approximately correspond to moderate and intense enstrophy, shown in (*a*) and (*b*) respectively. (*f*) Two-dimensional contours at the mid-plane. The production terms based on total strain is overwhelmingly positive. Bottom row: enstrophy production based on local strain, P_Ω^L, with $R = 2\eta_K$, once again suitably non-dimensionalised by mean enstrophy, at thresholds of (*h*) ±50 and (*g*) ±200, and also corresponding to moderate and intense enstrophy shown in (*a*) and (*b*) respectively. (*i*) Two-dimensional contours at the mid-plane, revealing that the production term based on local strain is strongly negative in the regions of intense vorticity. For each row, the thresholds shown in the first two isosurfaces plots are marked by dashed and solid lines respectively in the last 2-D contour field plot. Figure adapted from Buaria *et al.* (2020*b*).

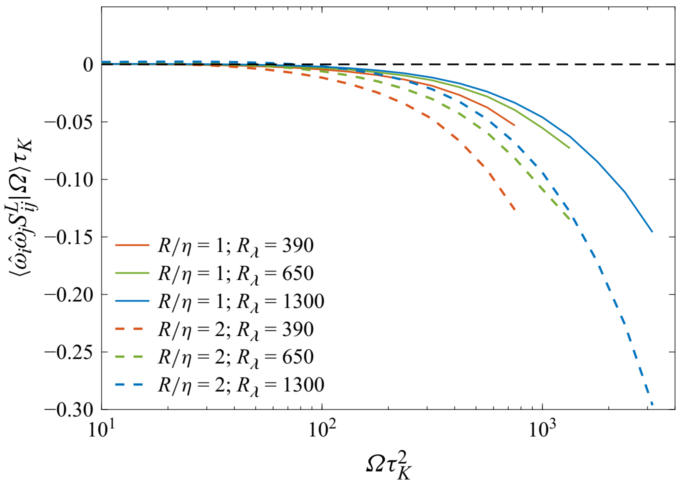

Figure 36. Conditional expectation of the enstrophy production due to the local strain: $P^L_\Omega = \omega_i \omega_j S^L_{ij}$. The curves shown correspond to $R/\eta = 1$ and 2, at $Re_\lambda = 390{-}1300$. Although not shown here, a similar result is also obtained in experiments (Buaria, Lawson & Wilczek 2024).

Figure 36 shows the conditional expectation $\langle P^L_\Omega | \Omega \rangle / \Omega$, for $R/\eta_K = 1$ and 2, at various Re_λ, complementing the previous figure, and highlighting the behaviour of P^L_Ω as a function of Ω. It can be seen that the conditional production term is essentially zero for small and moderate Ω. However, as $\Omega \tau_K^2$ grows, local production becomes negative and increases strongly in magnitude with Ω. We note that the values of P^L_Ω are overwhelmingly negative for large Ω, corroborated by the observation (not shown in the figure) that the conditional expectations of $|P^L_\Omega|$ and $-P^L_\Omega$ are virtually identical.

The observations in figures 35 and 36 (and also figure 34) clearly indicate that the local strain induced by vorticity acts to suppress further enstrophy growth. In other words, the nonlinear term itself encodes a self-attenuating mechanism which mitigates vorticity amplification even as viscosity decreases. As seen in figure 36, the onset of attenuation simply shifts to slightly higher Ω with decreasing viscosity (or increasing Re_λ). Thus, a careful mathematical analysis of this mechanism and determination of the bounds on P^L_Ω could possibly reveal a path to establish the regularity of the INSE.

The property of self-attenuation further implies a distinct structural organisation of the vorticity and velocity fields in regions of extreme enstrophy. In particular, elementary arguments show the importance of the twisting of vortex lines in generating the effect of self-attenuation (Buaria *et al.* 2020*b*). The recent analysis of Buaria *et al.* (2024) provides further evidence of this mechanism and its connection to the absence of singularity in the INSE under conditions typical of fully developed turbulence. A key consequence of such twisting is the local alignment of velocity and vorticity (Buaria *et al.* 2020*b*), a property often referred to as Beltramisation (Moffatt & Tsinober 1992). This alignment weakens the nonlinear term $\nabla \times (\boldsymbol{u} \times \boldsymbol{\omega})$, thereby reducing the efficiency of vortex stretching in the most intense regions of the flow.

8.4. *Discussion*

The Biot–Savart framework employed throughout this section offers a powerful tool to analyse the inherently non-local relationship between strain and vorticity – one of the central difficulties in understanding gradient amplification. Using this formulation, we reaffirmed the relation between the size of vortices and their amplitude, consistent with the phenomenological arguments developed earlier in § 6.3. Moreover, the non-local Biot–Savart analysis also highlights the role of inviscid self-attenuation mechanism, possibly underpinning the regularity of the INSE.

However, some open issues remain to be understood. The chief among them is the empirical scaling relation $\langle \Sigma | \Omega \rangle \sim \Omega^{\gamma}$, whose physical origin is not fully understood. How does the vorticity field, as shown exemplarily in figure 2, contribute to generating a strain field Σ, with specific scaling properties identified here, remains a key challenge. In particular, understanding the dependence of the exponent γ on Re_λ shown in figure 16, is essential in describing small-scale turbulence at high but finite Re_λ. Resolving these questions would help bridge the gap between phenomenological scaling arguments and dynamical, structure-based descriptions of small-scale turbulence.

9. Concluding remarks and open questions

Turbulence remains one of the most enduring and challenging frontiers in science and engineering. Its defining traits: nonlinearity, non-locality and a vast hierarchy of interacting scales, generate a dynamical richness that has long eluded a comprehensive understanding. Yet, turbulence is far from a singular challenge; much like the mythical Hydra, it presents itself as a multifaceted problem, with each head often demanding a distinct approach. Among the many facets, the dynamics of small scales occupy a uniquely central role in developing a fundamental picture of turbulence, serving as the backbone of turbulence theory and modelling.

Decades of investigations have unveiled deep insights into small-scale turbulence, from dissipation anomaly and Kolmogorov's statistical framework to the more recent understanding of intermittency, multifractality and coherent structures such as vortex tubes. Yet, despite these advances, a predictive and unified description of small scales remains elusive. The results reviewed in this article illustrate that while classical frameworks, particularly the multifractal formalism, capture several aspects of small-scale statistics with remarkable accuracy, they fail to fully account for the observed asymmetries and structural intricacies of the flow, especially the disparate behaviours of longitudinal and transverse statistics.

The description of velocity gradients stems from the INSE, whose defining features – nonlinearity and non-locality – also make them analytically intractable. The statistical framework introduced by Kolmogorov (1941), reviewed in § 3, remains one of the most profound ideas in turbulence theory. It postulates that at sufficiently large Reynolds numbers, small-scale statistics become independent of large-scale flow properties, leading to universality and scaling laws that continue to guide theoretical and modelling developments. The simple mean-field description of K41 works remarkably well in capturing the overall energetics of turbulence, for instance, when predicting low-order statistics such as the energy spectrum. Experimental and numerical evidence, however, has led to the unambiguous conclusion that energy transfers in turbulence are highly sporadic and localised, accompanied by the formation of extreme velocity gradients.

While intermittency marks the breakdown of Kolmogorov's mean-field picture, the core tenet of universality still endures in modern intermittency theories – discussed in § 5. Theories based on multifractality provide a statistical description of intermittency by treating turbulence as an ensemble of locally self-similar regions with a spectrum of scaling exponents from which anomalous scaling laws emerge. Although some discrepancies remain regarding the highest moment orders, the multifractal description appears to provide an accurate and self-consistent statistical description of the longitudinal velocity increments and gradients. However, extension of the framework to transverse components appears to fail in several essential aspects. The observed differences between longitudinal and transverse gradients serve as a clear reminder that these quantities probe distinct physical structures in the flow, highlighting the limitations of existing statistical approaches that overlook the structural and dynamical context.

Motivated by this, the structural analyses discussed in § 6 explored the regions giving rise to the most intense gradients, showing that the small-scale dynamics is closely tied to how strain and vorticity interact. The conditional coupling between these quantities reveals robust asymmetries that underpin the formation of extreme events. These results also emphasise that intermittency emerges not just from statistical variability but also from concrete amplification mechanisms shaped by the organisation of vortical and straining structures.

To gain deeper insight into these mechanisms, §§ 7 and 8 examined the amplification dynamics of vorticity and strain, and the role of non-local interactions using the Biot–Savart framework. These analyses revealed how regions of intense vorticity and strain arise from the nonlinear coupling between stretching, rotation and pressure effects, highlighting an intrinsic organisation of the small-scale flow. The Biot–Savart formulation, in particular, made it possible to disentangle the local and non-local contributions to vortex stretching and to quantify how surrounding vorticity fields induce strain. Remarkably, the results showed excellent consistency with the phenomenological results obtained earlier in § 6, reinforcing the view that non-locality plays a critical role in understanding extreme events. As an aside, the study of non-local effects led to the identification of an inviscid self-attenuation effect, which appears to prevent an unbounded amplification of vorticity, and could potentially help establish regularity of the INSE.

Beyond traditional scaling laws, the small-scale structure of turbulence reveals a remarkable coherency that cannot be captured by statistical theories alone. The amplification dynamics expose how small scales organise into distinct structures such as vortex tubes and strain sheets. These structures embody the nonlinear mechanisms rooted in vortex stretching and strain self-amplification that drive intermittency and energy transfers. Recognising this structure–dynamics connection would be central to developing a comprehensive, physically grounded predictive description of turbulence. In that regard, we isolate some pressing open problems which deserve further attention.

9.1. *Longitudinal vs. transverse statistics*

Since the moments of the velocity increments (and gradients) provide an essential way to characterise intermittency, the disparities between longitudinal and transverse statistics constitute a major unresolved issue. Historically, the longitudinal statistics have been the centre of attention, likely because only the 1-D longitudinal increment was accessible in early wind-tunnel experiments utilising hot-wire anemometry. In fact, despite the very significant progress in experimental methods, wind-tunnel experiments at the highest Reynolds numbers still rely on hot-wire anemometry. Additionally, the 4/5th law, which can be directly derived from the INSE, requires the knowledge of longitudinal increments only. In contrast, the corresponding 4/3rd and 4/15th laws (Eyink 2003), also exactly derivable from the INSE, require both longitudinal and transverse increments. Interestingly, they all demonstrate identical scalings, prompting a generalised assumption that transverse statistics follow identical scaling laws as their longitudinal counterparts for all moment orders. Once more sophisticated data from experiments and DNS became available, it was apparent that there are potential differences between the two. However, these early observations were often attributed to low-Reynolds-number effects or experimental uncertainties. Recent results have now clearly established that there are persistent differences between them, reflected in different scaling exponents of structure functions and also of the moments of velocity gradients, with transverse statistics displaying stronger intermittency.

The likely origin of this disparity lies in the differences between the dynamics governing vortical and straining motions. As remarked earlier, longitudinal and transverse quantities are related, in a loose way, to strain and vorticity, respectively. In this regard, the mechanisms concerning amplification of strain and vorticity provide a natural framework to understand the differences between them. The non-local effects also act very differently on vorticity and strain; when vorticity is non-locally amplified by strain (vortex stretching), it leads to local depletion of strain. In contrast, strain locally self-amplifies itself, but is non-locally attenuated by the pressure field. This complex interaction also seems to generate geometric organisation of vorticity into tubes and strain into sheets. However, these underlying dynamical differences are not taken into account in statistical approaches, including the multifractal model.

As it stands, all available theoretical predictions for inertial-range scaling laws have been derived for longitudinal statistics. While the generally capture the overall trend, some discrepancies seem to persist for high moment orders ($p > 8$). Moreover, as we saw in § 5, the multifractal extension from the inertial range to dissipation range works remarkably well in predicting the scaling of longitudinal gradient moments – see in particular table 3. This is to be contrasted with the case of transverse scaling exponents, for which such a correspondence does not work. The transverse scaling exponents exhibit saturation with respect to moment order (as seen in figure 7), approaching a limiting value of $\zeta_p^T \approx 2$ beyond $p \geqslant 10$. A similar saturation has also been observed for Lagrangian structure functions (Buaria & Sreenivasan 2023*c*), suggesting that this behaviour reflects a fundamental aspect of the underlying flow structure. Interestingly, a saturation exponent of 2 corresponds to a codimension of unity, which aligns with the presence of thin vortical filaments, hinting at a geometric underpinning of transverse intermittency originating in the vorticity–strain dynamics.

These results suggest that rather than describing longitudinal or transverse statistics separately, one must describe them jointly for a complete and accurate description of intermittency. Incidentally, such a perspective has once been considered within the multifractal framework, although only in the inertial range and also purely adopting a conventional cascade approach without any direct consideration of the Navier–Stokes dynamics (Meneveau *et al.* 1990). More recently, Buaria (2026) revisited this idea and extended the analysis to velocity gradients, demonstrating that the scaling of longitudinal gradients is solely prescribed by longitudinal structure functions – consistent with the results discussed earlier in § 5 – whereas, transverse gradient scaling is prescribed by mixed longitudinal–transverse structure functions. This finding essentially reinforces that a solution to the intermittency problem requires a general theoretical prediction for the scaling of mixed structure functions. Such a prediction would essentially capture both longitudinal and transverse statistics in inertial and dissipation ranges.

9.2. *The scope of universality*

While the results in this article were primarily derived from DNS of HIT, on numerous occasions we presented comparisons with other flows, including laboratory experiments in a wind tunnel, von Kármán mixing tank and also DNS of plane channel flow. Generally, results from these different configurations were in excellent agreement with each other – both for scaling laws and for statistics pertaining to structure of the velocity-gradient tensor. As discussed in § 5.4, the proportionality constants in the scaling laws can be matched across different flows. In fact, even the structure of the velocity-gradient tensor compares well quantitatively, as revealed by various conditional statistics in § 7. Essential to these comparisons is to quantify the intensity of turbulence by using small-scale statistical properties (as measured e.g. by the skewness of flatness of the velocity gradients), rather than Reynolds number, which necessarily relies on large-scale velocity, with clearly flow-dependent features (Buaria & Pumir 2025). Thus, as far as we could verify, small-scale universality as a core tenet of turbulence theory holds to a remarkable degree. It is also worth mentioning that although not directly considered here, some works have also shown various other aspects of the small-scale structure of turbulence to be universal, see e.g. Tsinober (2009), Elsinga & Marusic (2010), Zecchetto & Da Silva (2021) and Das & Girimaji (2022).

Nonetheless, it is important to delineate the scope of that universality. It is easy to argue that universality necessarily follows from local isotropy, as also originally hypothesised by Kolmogorov. In this sense, all the flows considered in this work reasonably satisfied local isotropy, by virtue of being far from any solid boundaries, and in regions of very weak to zero mean large-scale gradient. For instance, in wall-bounded turbulence, we considered statistics only near the centre of the channel, or the centre of a Rayleigh–Bénard cell, and likewise in wind-tunnel or mixing tank experiments. It is worth noticing that even in the flows investigated in this work, some anisotropies appear to diminish very slowly. This in particular is the case for the third moments (skewness), which appear as different in the three spatial directions (Buaria & Pumir 2025). In fact, in various flows, the presence of persistent large-scale shear appears to persistently violate local isotropy and hence universality, even when the Reynolds number increases (Shen & Warhaft 2000; Biferale & Procaccia 2005; Pumir *et al.* 2016; Tang, Antonia & Djenidi 2022).

A similar breakdown also occurs in passive-scalar turbulence, where the presence of a large-scale scalar gradient is known to persistently violate local isotropy (Sreenivasan 1991; Buaria *et al.* 2021*a*). Note that an effect of scalar gradients on the anisotropy of the flow features is also expected in the case of stably stratified turbulence, where the large-scale buoyancy gradient persists. This should be contrasted with the classical Rayleigh–Bénard set-up, where mixing confines the (unstable) temperature gradient to narrow boundary layers. In flows subject to sizable large-scale gradients, or close to the boundaries, universal features identified here would invariably break down, and leading-order corrections are required to capture the influence of shear or large-scale anisotropy on the small scales. Indeed, this has recently received some attention in various flows (Kaneda & Yamamoto 2021; Tang *et al.* 2022; Gong *et al.* 2025), but much more work is needed to develop a complete picture. This is obviously a challenging task as anisotropic corrections to small-scale description are likely to be flow specific.

9.3. *Related intermittency problems*

In this article, our focus has been entirely on the intermittency of the velocity field. However, intermittency is a far more general phenomenon in turbulent flows, manifesting also in the transport of scalars and in the Lagrangian dynamics of fluid particles. Both scalar and Lagrangian intermittency share deep connections with the velocity field, but also have their own distinct behaviour and challenges.

Lagrangian intermittency is, at least conceptually, the more direct extension of Eulerian intermittency (Borgas 1993; Chevillard *et al.* 2003; Biferale *et al.* 2004). This connection is most apparent when considering Lagrangian structure functions (moments of temporal velocity increments: $S_p^L(\tau) = \langle |u(t+\tau) - u(t)|^p \rangle$, whose inertial-range exponents can also be obtained from the Eulerian multifractal spectrum $D(h)$. Historically, it has been presumed that the $D(h)$ corresponding to longitudinal Eulerian statistics also prescribe the Lagrangian exponents (Biferale *et al.* 2004). However, recently it was shown that Lagrangian exponents in fact almost perfectly align with those of transverse Eulerian structure functions – with both saturating at 2 at high moment orders (Buaria & Sreenivasan 2023*c*). This further accentuates the urgent need to understand transverse Eulerian intermittency and its role in establishing a unified description of small-scale intermittency (for the velocity field in general). Nevertheless, this analogy seemingly breaks down when considering the statistics of acceleration (which represents the temporal velocity gradient). In this case, a naive extension of longitudinal or transverse intermittency fails to explain the observed statistics of acceleration (Buaria & Sreenivasan 2022*b*), including the strong correlations between different acceleration components (Buaria & Sreenivasan 2023*b*). These discrepancies underscore the urgent need for a complete framework that consistently links Eulerian and Lagrangian intermittency in both inertial and dissipation ranges.

The intermittency of scalar fields poses a different but equally rich set of questions. For passive scalars advected by the velocity field, the observed scalar intermittency is much stronger than that of velocity, as seen, for instance, in the scaling exponents of scalar increments and gradients (Warhaft 2000). The physical origin of this intermittency lies in the formation of characteristic ramp-cliff structures, where smooth regions of weak scalar gradients are punctuated by thin, intense gradients (Sreenivasan 1991; Shraiman & Siggia 2000; Falkovich, Gawędzki & Vergassola 2001). These cliffs arise from the compressive action of the velocity field on scalar field and seemingly transmit large-scale anisotropy, imposed for instance by a mean scalar gradient, down to the smallest dissipative scales. As a consequence, passive-scalar turbulence (in presence of a mean-gradient) exhibits a persistent violation of local isotropy across all scales. Although these structures have long been observed and studied, only recent advances in high-resolution DNS have enabled a a systematic and quantitative characterisation, particularly in the regime of high Schmidt number $Sc \gg 1$ (Buaria *et al.* 2021*a*,*b*), the Schmidt number being the non-dimensional ratio of kinematic viscosity and scalar diffusivity. For high Sc, the scalar field develops scales far smaller than those of the velocity field, making both experimental measurements and DNS extremely challenging.

Even the scalar increment statistics in the inertial range reveal a marked dependence of the scalar scaling exponents on Sc, with high-order moments exhibiting saturation at values that decrease as Sc increases (Buaria *et al.* 2021*b*). This behaviour highlights the intrinsically non-universal character of passive-scalar intermittency, in contrast to the more robust universality often assumed for velocity fluctuations. The breakdown of universality is of course also apparent from persistent anisotropy at small scales: strong scalar fronts preferentially align with the imposed mean gradient, leading to persistent skewness and directional dependence of scalar gradient statistics (Sreenivasan 1991; Shraiman & Siggia 2000; Warhaft 2000). Remarkably, the presence of ramp-cliff structures allows for a simple and geometric description of scalar gradient statistics (Buaria *et al.* 2021*a*). Extensions of this approach have recently been shown to capture extreme fluctuations of velocity gradients in flows in the presence of a mean shear, both in homogeneous shear-turbulence and in the log-layer of the turbulent boundary layer (Gong *et al.* 2025). Thus, the apparent lack of universality in passive-scalar intermittency not only poses an important problem in itself, but also offers valuable clues toward understanding velocity-gradient fluctuations – linking the physics of scalar mixing and small-scale intermittency in a broader, unifying framework.

In addition to passive scalar and tracer particles, intense gradients also play a direct and dominant role on the motion of inertial particles and bubbles in turbulent flows. Unlike tracers, such particles do not exactly follow the flow, but are strongly influenced by the local flow structures and topology. For instance, regions of intense vorticity associated with low-pressure cores attract lighter particles and bubbles. In contrast, heavier particles experience centrifugal effects and are expelled from vortical regions. Thus, intense fluctuations of dissipation and enstrophy directly control the distribution of inertial particles, leading to strong spatial inhomogeneities and clustering and also impact their collision and coalescence rates (Squires & Eaton 1991; Shaw 2003; Pumir & Wilkinson 2016). The situation becomes more complex in realistic settings, where additional physical processes come into play. For instance, in clouds phase change due to condensation and evaporation introduces thermal feedback which can alter both the particle dynamics and the underlying turbulent flow (Mellado 2017; Makwana *et al.* 2025). Similar considerations apply in multiphase flows or reacting flows where intermittency and the particle dynamics are two-way coupled. While steady progress has been made in these areas (Marchioli *et al.* 2025), understanding the coupling between intense gradients and the particle dynamics remains a pressing open problem, with broad implications for various natural and engineering flows.

9.4. *Importance of thermal fluctuations*

In this work, and more generally throughout the literature, turbulence intermittency has been investigated within the framework of the INSE. The foundational assumption being that the INSE, as a deterministic continuum model, fully captures the essential physics of turbulent motion down to the smallest scales. Under this view, the chaoticity and unpredictability of turbulence arises purely from the nonlinearity, rather than from any intrinsic stochasticity. This assertion has guided both theory and DNS, which have proven remarkably successful in reproducing experimental observations across a wide range of flows.

Recently, the role of thermal fluctuations arising from random molecular motion has been revisited, raising questions about the completeness and accuracy of the deterministic continuum description. Traditional arguments maintain that because the smallest scales of turbulence are still several orders of magnitude larger than the molecular mean-free path, thermal fluctuations can be neglected. However, refining earlier work of Betchov (1957), Bandak *et al.* (2022) have suggested that thermal fluctuations may become significant at scales just below the Kolmogorov scale. The essential argument relies on equating the exponentially decaying turbulent energy spectrum: $E(k) \sim u_K^2 \eta_K \exp(-k\eta_K)$, to the equipartition energy spectrum of thermal fluctuations: $E_{th}(k) \sim (k_B T/\rho)k^2$, where k_B is the Boltzmann constant and T the temperature. Balancing these expressions yields the condition

$$\theta_\eta (k\eta_K)^2 \exp(k\eta_K) \simeq 1, \quad \text{where} \quad \theta_\eta = \frac{k_B T}{\rho u_K^2 \eta_K^3}\,. \tag{9.1}$$

Estimates for θ_η in typical flows range from 10^{-6}–10^{-9}, and hence the solution to the above equation suggests that thermal fluctuations could become relevant for scales $k\eta_K \gtrsim 5$–10. Another analysis by Bell *et al.* (2022) suggests an even lower threshold, $k\eta_K \gtrsim 3$. Thus, from this perspective, thermal fluctuations could significantly alter the small-scale dynamics of turbulence.

However, no measurable influence of thermal fluctuations has yet been detected in turbulence experiments. This in part reflects the limits of present diagnostic capabilities, since given the estimate in (9.1), one needs to accurately resolve an exponentially decaying energy spectrum beyond $k\eta_K \gtrsim 3{-}5$, which is a daunting task in turbulence experiments. Nevertheless, direct comparisons between high-resolution DNS and precision laboratory experiments, made throughout this article, show striking quantitative agreement without requiring incorporation of thermal fluctuations. Thus, the evidence so far appears to suggest that the standard INSE (without thermal fluctuations) provide a faithful description of small-scale turbulence.

At the same time, when considering the dynamics of extreme events, another plausible argument can be made against the relevance of thermal fluctuations. As discussed earlier, extreme velocity gradients correspond to fluctuations as large as the r.m.s. of velocity, far exceeding the characteristic Kolmogorov velocity scale u_K that enters (9.1). Indeed, the spectral balance underlying that equation reflects the average energetics of the flow, not the strongly amplified gradients that underlie intermittency. These extreme events are directly governed by the deterministic nonlinearity, with their magnitude far exceeding the stochastic contributions that would arise from thermal fluctuations. Consequently, the statistical tails of velocity gradients that encode intermittency are unlikely to be affected by thermal fluctuations. Although not shown here, ongoing comparisons between DNS and new experiments in the Göttingen wind tunnel, which now resolve energy spectra beyond $k\eta_K > 1$, seem to affirm this expectation.

Nevertheless, the role of thermal fluctuations warrants further investigation – both in experimental attempts to detect them at sub-Kolmogorov scales and in numerical efforts to precisely quantify their dynamical impact on small scales. Their influence would clearly be relevant in regimes where the continuum description itself begins to falter, such as in very low-density flows, strongly compressible flows, or near critical transitions marked by strong coupling between hydrodynamics and thermodynamic fluctuations. As George Box famously remarked, 'All models are wrong, but some are useful.' The INSE have so far proven to be remarkably accurate and useful in describing a wide range of flows, faithfully capturing small-scale intermittency. Nevertheless, exploring the precise limits of this deterministic framework is important, particularly as DNS and experiments become more refined in probing increasingly smaller scales.

9.5. *Some lessons for turbulence modelling*

While this article focuses on the theoretical understanding of turbulence, the insights gained inevitably raise questions about their implications for turbulence modelling. In most real-world applications, DNS remains computationally infeasible, making reduced descriptions such as Reynolds-averaged Navier–Stokes (RANS) and large-eddy simulation (LES) indispensable. In RANS, only mean-flow quantities are evolved, with the entire range of turbulent scales represented through closure models. In contrast, LES resolves the large scales while modelling the entire range of small scales, relying on their presumed universality. Given that the mean flow is directly governed by the geometry and large-scale forcing, it is perhaps fair to say that RANS closures have little prospect of being generalisable across different flow configurations. In contrast, LES naturally offers significantly higher fidelity – albeit at a higher computational cost – by resolving the flow-specific large scales and invoking universality to model the small scales.

While the results discussed here provide strong support for small-scale universality in certain flows, they also warrant caution for more complex flows not covered here. As emphasised earlier, local isotropy is a prerequisite for universality, yet it is realised only far from boundaries and in regions with very weak or negligible mean gradients. The presence of persistent shear or strain can lead to significant departures from local isotropy, thereby invalidating the universality assumption that underpins LES closures. This suggests that different flow configurations may require different modelling strategies, even within the LES framework. One possible direction is to move beyond the classical LES paradigm and consider approaches that resolve not only the large scales, but also some portion of the small-scale dynamics – effectively bridging the gap between LES and DNS (Donzis & Sajeev 2024; Moitro, Dammati & Poludnenko 2024). Such hybrid or multiscale approaches could also allow a more direct representation of the gradient dynamics and intermittency, and may be especially beneficial in flows where backscatter effects are prominent, such as reacting flows, particle-laden turbulence. In these situations, the local transfer of energy from small to large scales – often poorly captured by traditional closures – plays a significant role, and a more faithful representation of the small-scale dynamics is of critical importance.

Even in situations where universality is nominally satisfied, the presence of strong intermittency and observed asymmetries between longitudinal and transverse fluctuations clearly indicate that the small scales are not adequately described by simple, isotropic or local models. Conventional LES closures such as eddy-viscosity and cascade-based models are designed primarily to reproduce the average energy transfer and spectral behaviour, without accounting for the local structure and dynamics (Sagaut 2006). In fact, such models may even misrepresent the amplification mechanisms and geometric organisation that underpin the small scales.

This points towards new opportunities for improving turbulence modelling by incorporating insights from the velocity-gradient dynamics. In recent years, reduced-order modelling of velocity gradients has seen significant advances, with newer approaches accurately reproducing key DNS results at an insignificant cost (Buaria & Sreenivasan 2023; Johnson & Wilczek 2024*a*; Carbone *et al.* 2024; Das & Girimaji 2024). By explicitly accounting for nonlinear amplification mechanisms and statistical constraints, such models could provide a more physically grounded description of small scales. When coupled with LES, such approaches could improve the prediction of dissipation, intermittency and backscatter across different flow configurations, while retaining computational tractability. While some efforts have been made in this direction (Johnson & Meneveau 2018), much work remains to systematically integrate such dynamical models into practical subgrid-scale closures.

With the improved understanding of small-scale physics and the continued growth of computational power, it is becoming increasingly clear that LES and related approaches will play a central role in turbulence simulations of real-world flows. However, realising their full potential will require significant advances in subgrid-scale modelling. In particular, progress will depend on moving beyond simplified phenomenological closures and toward approaches that combine statistical descriptions with insights from flow structure and dynamics. The challenge is to translate the increasingly detailed understanding of small-scale turbulence into models that remain predictive across a wide range of flows while retaining computational efficiency. At the same time, the importance of small-scale intermittency extends beyond its role in the dynamics of turbulence itself. As discussed earlier in § 9.3, extreme events play a central role in a variety of applications, including mixing, combustion and multiphase flows, where they often control rates of transport, reaction and phase interaction. Developing refined models that can reliably capture these effects is therefore not only of fundamental interest but also of considerable practical importance It is our hope that that the understanding synthesised in this article will help inform and guide future research and modelling efforts across a wide range of turbulent flows.

9.6. *Final remarks*

Given its complexity and ubiquity, turbulence continues to challenge our theoretical insight and test the limits of our computational and experimental capabilities, with the study of small scales remaining one of its most elusive aspects. The mathematical intractability of the INSE suggests that a complete theory of turbulence may never be realised. Nevertheless, remarkable progress has been achieved through a synthesis of phenomenology, high-resolution simulations and increasingly refined laboratory measurements.

The results reviewed in this article underscore both the progress and limitations of the prevailing approaches. The multifractal formalism provides a compelling statistical scaffold, yet glaring shortcomings remain, particularly in explaining the asymmetries between longitudinal and transverse fluctuations, and between strain and the vorticity dynamics. The emerging view is that intermittency has to be understood holistically, linking statistics to the joint dynamics and the geometry of strain and vorticity.

It is instructive to recall that nearly three decades ago, the review by Sreenivasan & Antonia (1997) posed a number of open questions concerning universality, anisotropy, role of structures, a careful study of distributions of velocity gradients and increments, and the need for reliable data at high Reynolds numbers. Most of these issues have since been addressed. Direct numerical simulations now access regimes that were once deemed unattainable, laboratory experiments can measure the full velocity-gradient tensor; and our understanding of small-scale organisation and non-local interactions has grown immensely. Yet, as so often in turbulence and science in general, the resolution of old questions has revealed new layers of complexity. Explaining the asymmetry between longitudinal and transverse statistics, understanding the coupling of strain and the vorticity dynamics, clarifying the potential role of thermal fluctuations, and assessing the impact of intermittency on mixing and transport processes now stand as the next frontiers.

It should of course be kept in mind that turbulence is profoundly a multifaceted problem, and progress necessarily must be pursued on several fronts simultaneously. Given the present focus on small scales, we have necessarily left aside the vast range of other problems: from large-scale anisotropy and compressibility to scalar mixing, wall-bounded turbulence and modelling applications that continue to present their own challenges. Ultimately, progress on any one front will continue to rely on the interplay between theory, DNS and experiments. While recent advances in DNS and experiments seem to continue to outpace theory, the field now possesses a wealth of detailed data that demand deeper theoretical interpretation. Pushing the limits of DNS and experiments will obviously remain essential, but renewed effort in theoretical development now appears to be equally critical to transform these empirical insights into predictive frameworks.

Finally, it is worth stressing that even in the most favourable case, the remarkably complex subject of turbulent flow is unlikely to be regarded as 'solved' merely from a better understanding of intermittency. As history in other scientific disciplines has shown, the resolution of fundamental questions often opens new avenues of inquiry. Likewise, a deeper understanding of intermittency will not exhaust the richness of turbulence, but it will provide the foundation for confronting even broader challenges (as also embodied by the quotation at the very beginning).

Acknowledgements. The authors gratefully acknowledge their collaborators for numerous insightful discussions and contributions over the years that have also informed this work. The authors thank R. Benzi, L. Biferale, G. Eyink, G. Falkovich, N. Goldenfeld, T. Gotoh, R. Govindarajan, C. Meneveau, B. Shraiman, E. Siggia, K. R. Sreenivasan, H. Xu, P. F. Yang, P. K. Yeung, for their inputs on a draft of this article. The authors also thank B. Dubrulle, O. Pouliquen, P. Johnson, M. Wilczek, for carefully reading the manuscript and providing feedback that helped improve its clarity and presentation. The authors gratefully acknowledge

https://doi.org/10.1017/jfm.2026.11494 Published online by Cambridge University Press

the Gauss Centre for Supercomputing e.V. for providing computing time on the supercomputers JUWELS and JUQUEEN at Jülich Supercomputing Centre (JSC), where the simulations and data analyses reported in this paper were primarily performed.

Funding. D.B.'s work was partially supported by Texas Tech University. A.P. acknowledges partial support from ANR (project TILT, ANR-20-CE30-0035).

Declaration of interests. The authors report no conflicts of interest.

Data availability statement. The data that support the findings of this study are available from the corresponding author upon reasonable request.

References

Andreotti, B. 1997 Studying Burgers' models to investigate the physical meaning of the alignments statistically observed in turbulence. *Phys. Fluids* **9**, 735–742.

Ashurst, W.T., Kerstein, A.R., Kerr, R.M. & Gibson, C.H. 1987 Alignment of vorticity and scalar gradient with strain rate in simulated Navier–Stokes turbulence. *Phys. Fluids* **30**, 2343–2353.

Bandak, D., Goldenfeld, N., Mailybaev, A.A. & Eyink, G. 2022 Dissipation-range fluid turbulence and thermal noise. *Phys. Rev. E* **105**, 065113.

Beale, J.T., Kato, T. & Majda, A. 1984 Remarks on the breakdown of smooth solutions for the 3-D Euler equations. *Commun. Math. Phys.* **94**, 61–66.

Bell, J.B., Nonaka, A., Garcia, A.L. & Eyink, G. 2022 Thermal fluctuations in the dissipation range of homogeneous isotropic turbulence. *J. Fluid Mech.* **939**, A12.

Benzi, R., Biferale, L., Paladin, G., Vulpiani, A. & Vergassola, M. 1991 Multifractality in the statistics of the velocity gradients in turbulence. *Phys. Rev. Lett.* **67**, 2299.

Benzi, R., Ciliberto, S., Tripiccione, R., Baudet, C., Massaioli, F. & Succi, S. 1993 Extended self-similarity in turbulent flows. *Phys. Rev. E* **48**, R29–R32.

Benzi, R., Paladin, G., Parisi, G. & Vulpiani, A. 1984 On the multifractal nature of fully developed turbulence and chaotic systems. *J. Phys. A* **17**, 3521.

Betchov, R. 1956 An inequality concerning the production of vorticity in isotropic turbulence. *J. Fluid Mech.* **1**, 497–504.

Betchov, R. 1957 On the fine structure of turbulent flows. *J. Fluid Mech.* **3**, 205–216.

Biferale, L., Boffetta, G., Celani, A., Devenish, B.J., Lanotte, A. & Toschi, F. 2004 Multifractal statistics of Lagrangian velocity and acceleration in turbulence. *Phys. Rev. Lett.* **93**, 064502.

Biferale, L. & Procaccia, I. 2005 Anisotropy in turbulent flows and in turbulent transport. *Phys. Rep.* **414**, 43–164.

Bodenschatz, E., Malinowski, S.P., Shaw, R.A. & Stratmann, F. 2010 Can we understand clouds without turbulence? *Science* **327**, 970–971.

Borgas, M.S. 1993 The multifractal Lagrangian nature of turbulence. *Phil. Trans. R. Soc. Lond. A* **342**, 379–411.

Boschung, J. 2015 Exact relations between the moments of dissipation and longitudinal velocity derivatives in turbulent flows. *Phys. Rev. E* **92**, 043013.

Bramwell, S.T., Holdsworth, P.C.W. & Pinton, J.F. 1998 Universality of rare fluctuations in turbulence and critical phenomena. *Nature* **396**, 552–554.

Buaria, D. 2026 Unified multifractal description of longitudinal and transverse intermittency in fully developed turbulence. arXiv: 2601.12528.

Buaria, D., Bodenschatz, E. & Pumir, A. 2020*a* Vortex stretching and enstrophy production in high Reynolds number turbulence. *Phys. Rev. Fluids* **5**, 104602.

Buaria, D., Clay, M.P., Sreenivasan, K.R. & Yeung, P.K. 2021*a* Small-scale isotropy and ramp-cliff structures in scalar turbulence. *Phys. Rev. Lett.* **126**, 034504.

Buaria, D., Clay, M.P., Sreenivasan, K.R. & Yeung, P.K. 2021*b* Turbulence is an ineffective mixer when Schmidt numbers are large. *Phys. Rev. Lett.* **126**, 074501.

Buaria, D., Lawson, J.M. & Wilczek, M. 2024 Twisting vortex lines regularize Navier–Stokes turbulence. *Sci. Adv.* **10**, eado1969.

Buaria, D. & Pumir, A. 2021 Nonlocal amplification of intense vorticity in turbulent flows. *Phys. Rev. Res.* **3**, 042020.

Buaria, D. & Pumir, A. 2022 Vorticity-strain rate dynamics and the smallest scales of turbulence. *Phys. Rev. Lett.* **128**, 094501.

BUARIA, D. & PUMIR, A. 2023 Role of pressure in the dynamics of intense velocity gradients in turbulent flows. *J. Fluid Mech.* **973**, A23.

BUARIA, D. & PUMIR, A. 2025 Universality of extreme events in turbulent flows. *Phys. Rev. Fluids* **10**, L042601.

BUARIA, D., PUMIR, A. & BODENSCHATZ, E. 2020*b* Self-attenuation of extreme events in Navier–Stokes turbulence. *Nat. Commun.* **11**, 5852.

BUARIA, D., PUMIR, A. & BODENSCHATZ, E. 2022 Generation of intense dissipation in high Reynolds number turbulence. *Phil. Trans. R. Soc. Lond. A* **380**, 20210088.

BUARIA, D., PUMIR, A., BODENSCHATZ, E. & YEUNG, P.K. 2019 Extreme velocity gradients in turbulent flows. *New J. Phys.* **21**, 043004.

BUARIA, D. & SREENIVASAN, K.R. 2020 Dissipation range of the energy spectrum in high Reynolds number turbulence. *Phys. Rev. Fluids* **5**, 092601(R).

BUARIA, D. & SREENIVASAN, K.R. 2022*a* Intermittency of turbulent velocity and scalar fields using three-dimensional local averaging. *Phys. Rev. Fluids* **7**, L072601.

BUARIA, D. & SREENIVASAN, K.R. 2022*b* Scaling of acceleration statistics in high Reynolds number turbulence. *Phys. Rev. Lett.* **128**, 234502.

BUARIA, D. & SREENIVASAN, K.R. 2023*a* Forecasting small-scale dynamics of fluid turbulence using deep neural networks. *Proc. Natl Acad. Sci.* **120** (30), e2305765120.

BUARIA, D. & SREENIVASAN, K.R. 2023*b* Lagrangian acceleration and its Eulerian decompositions in fully developed turbulence. *Phys. Rev. Fluids* **8**, L032601.

BUARIA, D. & SREENIVASAN, K.R. 2023*c* Saturation and multifractality of Lagrangian and Eulerian scaling exponents in three-dimensional turbulence. *Phys. Rev. Lett.* **131**, 204001.

BURGERS, J.M. 1948 A mathematical model illustrating the theory of turbulence. *Adv. Appl. Mech.* **1**, 171–199.

CANTWELL, B.J. 1992 Exact solution of a restricted Euler equation for the velocity gradient tensor. *Phys. Fluids A* **4**, 782–793.

CARBONE, M. & BRAGG, A.D. 2020 Is vortex stretching the main cause of the turbulent energy cascade? *J. Fluid Mech.* **883**, R2.

CARBONE, M., PETERHANS, V.J., ECKER, A.S. & WILCZEK, M. 2024 Tailor-designed models for the turbulent velocity gradient through normalizing flow. *Phys. Rev. Lett.* **133**, 184001.

CHEN, S., SREENIVASAN, K.R., NELKIN, M. & CAO, N. 1997 Refined similarity hypothesis for transverse structure functions in fluid turbulence. *Phys. Rev. Lett.* **79**, 2253–2256.

CHEVILLARD, L., ROUX, S.G., LÉVÊQUE, E., MORDANT, N., PINTON, J.-F. & ARNÉODO, A. 2003 Lagrangian velocity statistics in turbulent flows: effects of dissipation. *Phys. Rev. Lett.* **91**, 214502.

CONSTANTIN, P., FEFFERMAN, C. & MAJDA, A. 1996 Geometric constraints on potentially singular solutions for the 3D Euler equations. *Commun. Part. Diff. Equ.* **21**, 559–571.

DAS, R. & GIRIMAJI, S.S. 2022 The effect of large-scale forcing on small-scale dynamics of incompressible turbulence. *J. Fluid Mech.* **941**, A34.

DAS, R. & GIRIMAJI, S.S. 2024 Data-driven model for Lagrangian evolution of velocity gradients in incompressible turbulent flows. *J. Fluid Mech.* **984**, A39.

DHRUVA, B., TSUJI, Y. & SREENIVASAN, K.R. 1997 Transverse structure functions in high-Reynolds-number turbulence. *Phys. Rev. E* **56**, R4928–R4930.

DOERING, C.R. 2009 The 3D Navier–Stokes problem. *Annu. Rev. Fluid Mech.* **41**, 109–128.

DOMARADZKI, J.A. & ROGALLO, R.S. 1990 Local energy-transfer and nonlocal interactions in homogeneous, isotropic turbulence. *Phys. Fluids* **2**, 413–426.

DONZIS, D.A. & SAJEEV, S. 2024 Degrees of freedom and the dynamics of fully developed turbulence. *Phys. Rev. Fluids* **9** (4), 044605.

DONZIS, D.A., YEUNG, P.K. & SREENIVASAN, K.R. 2008 Dissipation and enstrophy in isotropic turbulence: resolution effects and scaling in direct numerical simulations. *Phys. Fluids* **20**, 045108.

DUBRULLE, B. 1994 Intermittency in fully developed turbulence: Log-Poisson statistics and generalized scale covariance. *Phys. Rev. Lett.* **73**, 959.

DUBRULLE, B. 2019 Beyond Kolmogorov cascades. *J. Fluid Mech.* **12**, 45.

DUBRULLE, B. 2022 Multi-fractality, universality and singularity in turbulence. *Fractal Fract.* **6**, 613.

DUCHON, J. & ROBERT, R. 2000 Inertial energy dissipation for weak solutions of incompressible euler and navier–stokes equations. *Nonlinearity* **13** (1), 249–255.

ELSINGA, G.E., ISHIHARA, T. & HUNT, J.C.R. 2020 Extreme dissipation and intermittency in turbulence at very high Reynolds numbers. *Proc. R. Soc. Lond. A* **476**, 20200592.

ELSINGA, G.E. & MARUSIC, I. 2010 Universal aspects of small-scale motions in turbulence. *J. Fluid Mech.* **662**, 514–539.

EYINK, G. 2024 Onsager's ideal turbulence theory. *J. Fluid Mech.* **988**, P1.

EYINK, G.L. 2003 Local 4/5-law and energy dissipation anomaly in turbulence. *Nonlinearity* **16** (1), 137–145.

FALKOVICH, G., GAWĘDZKI, K. & VERGASSOLA, M. 2001 Particles and fields in fluid turbulence. *Rev. Mod. Phys.* **73**, 913–975.

FEFFERMAN, C. 2006 *Existence and Smoothness of the Navier–Stokes Equations*. Clay Mathematical Institute.

FRISCH, U. 1995 *Turbulence: the Legacy of Kolmogorov*. Cambridge University Press.

GHASHGHAIE, S., BREYMANN, W., PEINKE, J., TALKNER, P. & DODGE, Y. 1996 Turbulent cascades in foreign exchange markets. *Nature* **381**, 767–770.

GONG, X., YANG, P.F., XU, H. & PUMIR, A. 2025 Small-scale anisotropy and ramp–cliff structures in turbulent shear flows. *J. Fluid Mech.* **1009**, R6.

GORBUNOVA, A., BALARAC, G., BOURGOIN, M., CANET, L., MORDANT, N. & ROSSETTO, V. 2020 Analysis of the dissipative range of the energy spectrum in grid turbulence and in direct numerical simulations. *Phys. Rev. Fluids* **5**, 044604.

GOTOH, T., FUKAYAMA, D. & NAKANO, T. 2002 Velocity field statistics in homogeneous steady turbulence obtained using a high-resolution direct numerical simulation. *Phys. Fluids* **14**, 1065–1081.

GOTOH, T., WATANABE, T. & SAITO, I. 2023 Kinematic effects on probability density functions of energy dissipation rate and enstrophy in turbulence. *Phys. Rev. Lett.* **130**, 254001.

GOTOH, T. & YANG, J. 2022 Transition of fluctuations from Gaussian state to turbulent state. *Phil. Trans. R. Soc. Lond. A* **380**, 20210097.

GRAHAM, J., *et al.* 2016 A web services accessible database of turbulent channel flow and its use for testing a new integral wall model for LES. *J. Turbul.* **17**, 181–215.

GYLFASON, A., AYYALASOMAYAJULA, S. & WARHAFT, Z. 2004 Intermittency, pressure and acceleration statistics from hot-wire measurements in wind-tunnel turbulence. *J. Fluid Mech.* **501**, 213–229.

HAMLINGTON, P.E., SCHUMACHER, J. & DAHM, W.J.A. 2008*a* Direct assessment of vorticity alignment with local and nonlocal strain rates in turbulent flows. *Phys. Fluids* **20**, 111703.

HAMLINGTON, P.E., SCHUMACHER, J. & DAHM, W.J.A. 2008*b* Local and nonlocal strain rate fields and vorticity alignment in turbulent flows. *Phys. Rev. E* **77**, 026303.

ISHIHARA, T., GOTOH, T. & KANEDA, Y. 2009 Study of high-Reynolds number isotropic turbulence by direct numerical simulations. *Annu. Rev. Fluid Mech.* **41**, 165–180.

ISHIHARA, T., KANEDA, Y., YOKOKAWA, M., ITAKURA, K. & UNO, A. 2007 Small-scale statistics in high resolution of numerically isotropic turbulence. *J. Fluid Mech.* **592**, 335–366.

ISHIHARA, T., MORISHITA, K., YOKOKAWA, M., UNO, A. & KANEDA, Y. 2016 Energy spectrum in high-resolution direct numerical simulation of turbulence. *Phys. Rev. Fluids* **1**, 082403.

IYER, K.P., SREENIVASAN, K.R. & YEUNG, P.K. 2020 Scaling exponents saturate in three-dimensional isotropic turbulence. *Phys. Rev. Fluids* **5**, 054605.

JIMÉNEZ, J., WRAY, A.A., SAFFMAN, P.G. & ROGALLO, R.S. 1993 The structure of intense vorticity in isotropic turbulence. *J. Fluid Mech.* **255**, 65–90.

JOHNSON, P.L. 2020 Energy transfer from large to small scales in turbulence by multi-scale nonlinear strain and vorticity interactions. *Phys. Rev. Lett.* **124**, 104501.

JOHNSON, P.L. & MENEVEAU, C. 2018 Predicting viscous-range velocity gradient dynamics in large-eddy simulations of turbulence. *J. Fluid Mech.* **837**, 80–114.

JOHNSON, P.L. & WILCZEK, M. 2024 Multiscale velocity gradients in turbulence. *Annu. Rev. Fluid Mech.* **56**, 463–490.

KANEDA, Y. & YAMAMOTO, Y. 2021 Velocity gradient statistics in turbulent shear flow: an extension of Kolmogorov's local equilibrium theory. *J. Fluid Mech.* **929**, A13.

DE KÁRMÁN, T. & HOWARTH, L. 1938 On the statistical theory of isotropic turbulence. *Proc. R. Soc. Lond. A* **164**, 192–215.

KATO, T. 1972 Nonstationary flows of viscous and ideal fluids in R^3. *J. Funct. Anal.* **9** (3), 296–305.

KHURSHID, S., DONZIS, D.A. & SREENIVASAN, K.R. 2023 Emergence of universal scaling in isotropic turbulence. *Phys. Rev. E* **107**, 045102.

KIM, J. & LEONARD, A. 2024 The early days and rise of turbulence simulation. *Annu. Rev. Fluid Mech.* **56**, 21–44.

KNUTSEN, A.N., BAJ, P., LAWSON, J.M., BODENSCHATZ, E., DAWSON, J.R. & WORTH, N.A. 2020 The inter-scale energy budget in a von kármán mixing flow. *J. Fluid Mech.* **895**, A11.

KOLMOGOROV, A.N. 1941 The local structure of turbulence in an incompressible fluid for very large Reynolds numbers. *Dokl. Akad. Nauk SSSR* **30**, 9–13.

KOLMOGOROV, A.N. 1962 A refinement of previous hypotheses concerning the local structure of turbulence in a viscous incompressible fluid at high Reynolds number. *J. Fluid Mech.* **13**, 82–85.

LAWSON, J.M. & DAWSON, J.R. 2014 A scanning PIV method for fine-scale turbulence measurements. *Exp. Fluids* **55**, 1857.

Lee, M.K. & Moser, R.D. 2015 Direct numerical simulation of turbulent channel flow up to $Re_\tau \approx 5200$. *J. Fluid Mech.* **774**, 395–415.

Leray, J. 1934 Sur le mouvement d'un liquide visqueux emplissant l'espace. *Acta Math.* **63**, 193–248.

Lund, T.S. & Rogers, M.M. 1994 An improved measure of strain state probability in turbulent flows. *Phys. Fluids* **6** (5), 1838–1847.

Luo, G. & Hou, T.Y. 2014 Potentially singular solutions of the 3d axisymmetric euler equations. *Proc. Natl Acad. Sci.* **111**, 12968–12973.

Makwana, N.N., Kumar, B., Sethuraman, Y.P.M. & Govindarajan, R. 2025 Spatially inhomogeneous phase change, and its effect on cloud turbulence. *Geophys. Res. Lett.* **52**, e2025GL117378.

Marchioli, C., *et al.* 2025 Particle-laden flows. *Intl J. Multiphase Flow* **191**, 105291.

Mellado, J.P. 2017 Cloud-top entrainment in stratocumulus clouds. *Annu. Rev. Fluid Mech.* **49**, 145–169.

Meneveau, C. 2011 Lagrangian dynamics and models of the velocity gradient tensor in turbulent flows. *Annu. Rev. Fluid Mech.* **43**, 219–245.

Meneveau, C. & Sreenivasan, K.R. 1987 Simple multifractal cascade model for fully developed turbulence. *Phys. Rev. Lett.* **59**, 1424.

Meneveau, C. & Sreenivasan, K.R. 1991 The multifractal nature of turbulent energy dissipation. *J. Fluid Mech.* **224**, 429–484.

Meneveau, C., Sreenivasan, K.R., Kailasnath, P. & Fan, M.S. 1990 Joint multifractal measures: theory and applications to turbulence. *Phys. Rev. A* **41** (2), 894.

Moffatt, H.K. & Tsinober, A. 1992 Helicity in laminar and turbulent flows. *Annu. Rev. Fluid Mech.* **24**, 281–312.

Moin, P. & Mahesh, K. 1998 Direct numerical simulation: a tool in turbulence research. *Annu. Rev. Fluid Mech.* **30**, 539–578.

Moitro, A., Dammati, S.S. & Poludnenko, A.Y. 2024 Large/small eddy simulations: a high-fidelity method for studying high-Reynolds number turbulent flows. *Phys. Fluids* **36** (9), 095157.

Monin, A.S. & Yaglom, A.M. 1975 *Statistical Fluid Mechanics*, vol. II. MIT Press.

Musci, B., Dubrulle, B., LeBris, J., Geneste, D., Braganca, P., Foucaut, J.-M., Cuvier, C. & Cheminet, A. 2025 Experimental measurement of the vorticity–strain alignment around extreme energy transfer events. *J. Fluid Mech.* **1016**, A53.

Muzy, J.F., Bacry, E. & Arneodo, A. 1991 Wavelets and multifractal formalism for singular signals: application to turbulence data. *Phys. Rev. Lett.* **67**, 3515–3518.

Nelkin, M. 1990 Multifractal scaling of velocity derivatives in turbulence. *Phys. Rev. A* **42**, 7226–7229.

Nguyen, F., Laval, J.-P. & Dubrulle, B. 2020 Characterizing most irregular small-scale structures in turbulence using local hölder exponents. *Phys. Rev. E* **102**, 063105.

Nomura, K.K. & Post, G.K. 1998 The structure and dynamics of vorticity and rate of strain in incompressible homogeneous turbulence. *J. Fluid Mech.* **377**, 65–97.

Obukhov, A.M. 1962 Some specific features of atmospheric turbulence. *J. Geophys. Res.* **67**, 3011–3014.

Ohkitani, K. 1994 Kinematics of vorticity: vorticity-strain conjugation in incompressible fluid flows. *Phys. Rev. E* **50**, 5107–5110.

Ohkitani, K. & Kishiba, S. 1995 Nonlocal nature of vortex stretching in an inviscid fluid. *Phys. Fluids* **7**, 411–421.

Onsager, L. 1949 Statistical hydrodynamics. *Nuovo Cimento Suppl.* **6**, 279–287.

Orszag, S.A. & Patterson, G.S. 1972 Numerical simulation of three-dimensional homogeneous isotropic turbulence. *Phys. Rev. Lett.* **28**, 76–79.

Paladin, G. & Vulpiani, A. 1987 Degrees of freedom of turbulence. *Phys. Rev. A* **35**, 1971–1973.

Parisi, G. & Frisch, U. 1985 On the singularity structure of fully developped turbulence. In *Turbulence and Predictability in Geophysical Fluid Dynamics and Climate Dynamics*, pp. 84–87. North-Holland.

Patterson, G.S. & Orszag, S.A. 1971 Spectral calculations of isotropic turbulence: efficient removal of aliasing interactions. *Phys. Fluids* **14**, 2538–2541.

Pearson, B.R., Krogstad, P.-A. & van de Water, W. 2002 Measurements of the turbulent energy dissipation rate. *Phys. Fluids* **14**, 1288–1290.

Pope, S.B. 2000 *Turbulent Flows*. Cambridge University Press.

Pumir, A. & Wilkinson, M. 2016 Collisional aggregation due to turbulence. *Annu. Rev. Condens. Matter Phys.* **7**, 141–170.

Pumir, A., Xu, H. & Siggia, E.D. 2016 Small-scale anisotropy in turbulent boundary layers. *J. Fluid Mech.* **804**, 5–23.

Richardson, L.F. 1922 *Weather Prediction by Numerical Process*. Cambridge Univ. Press.

Rogallo, R.S. 1981 Numerical experiments in homogeneous turbulence. *NASA Technical* Memo. 81315.

https://doi.org/10.1017/jfm.2026.11494 Published online by Cambridge University Press

SADDHOUGHI, S.G. & VEERAVALLI, S.V. 1994 Local isotropy in turbulent boundary layers at high Reynolds number. *J. Fluid Mech.* **268**, 333–372.

SAGAUT, P. 2006 *Large Eddy Simulation for Incompressible Flows: An Introduction*. Springer.

SCHUMACHER, J., SCHEEL, J.D., KRASNOV, D., DONZIS, D.A., YAKHOT, V. & SREENIVASAN, K.S. 2014 Small-scale universality in fluid turbulence. *Proc. Natl Acad. Sci.* **111**, 10961–10965.

SHAW, R.A. 2003 Particle-turbulence interactions in atmospheric clouds. *Annu. Rev. Fluid Mech.* **35**, 183–227.

SHE, Z.-S. & LEVEQUE, E. 1994 Universal scaling laws in fully developed turbulence. *Phys. Rev. Lett.* **72**, 336–339.

SHEN, X. & WARHAFT, Z. 2000 The anisotropy of the small scale structure in high Reynolds number turbulent shear flow. *Phys. Fluids* **12**, 2976–2989.

SHEN, X. & WARHAFT, Z. 2002 Longitudinal and transverse structure functions in sheared and unsheared wind-tunnel turbulence. *Phys. Fluids* **14** (1), 370–381.

SHRAIMAN, B.I. & SIGGIA, E.D. 2000 Scalar turbulence. *Nature* **405**, 639–646.

SIGGIA, E.D. 1981 Invariants for the one-point vorticity and strain rate correlation functions. *Phys. Fluids* **24**, 1934–1936.

SQUIRES, K.D. & EATON, J.K. 1991 Preferential concentration of particles by turbulence. *Phys. Fluids A* **3**, 1169–1178.

SREENIVASAN, K.R. 1991 On local isotropy of passive scalars in turbulent shear flows. *Proc. R. Soc. Lond.* **434**, 165–182.

SREENIVASAN, K.R. 1998 An update on the energy dissipation rate in isotropic turbulence. *Phys. Fluids* **10**, 528–529.

SREENIVASAN, K.R. & ANTONIA, R.A. 1997 The phenomenology of small-scale turbulence. *Annu. Rev. Fluid Mech.* **29**, 435–477.

SREENIVASAN, K.R. & YAKHOT, V. 2021 Dynamics of three-dimensional turbulence from Navier–Stokes equations. *Phys. Rev. Fluids* **6**, 104604.

TANG, S.L., ANTONIA, R.A. & DJENIDI, L. 2022 Transport equations for the normalized nth-order moments of velocity derivatives in grid turbulence. *J. Fluid Mech.* **930**, A31.

THORPE, S.A. 2005 *The Turbulent Ocean*. Cambridge University Press.

TSINOBER, A. 2009 *An Informal Conceptual Introduction to Turbulence*. Springer.

VASSILICOS, J.C. 2015 Dissipation in turbulent flows. *Annu. Rev. Fluid Mech.* **47**, 95–114.

VELA-MARTÍN, A. 2022 The energy cascade as the origin of intense events in small-scale turbulence. *J. Fluid Mech.* **937**, A13.

VIEILLEFOSSE, P. 1982 Local interaction between vorticity and shear in a perfect incompressible fluid. *J. Phys.* **43**, 837–842.

WALLACE, J.M. & VUKOSLAVČEVIĆ, P.V. 2010 Measurement of velocity gradient tensor in turbulent flows. *Annu. Rev. Fluid Mech.* **42**, 157–181.

WARHAFT, Z. 2000 Passive scalars in turbulent flows. *Annu. Rev. Fluid Mech.* **32**, 203–240.

WYNGAARD, J.C. 2010 *Turbulence in the Atmosphere*. Cambridge University Press.

YAKHOT, V. & SREENIVASAN, K.R. 2005 Anomalous scaling of structure functions and dynamic constraints on turbulence simulation. *J. Stat. Phys.* **121**, 823–841.

YEUNG, P.K., RAVIKUMAR, K., UMA-VAIDESWARAN, R., DOTSON, D.L., SREENIVASAN, K.R., POPE, S.B., MENEVEAU, C. & NICHOLS, S. 2025 Small-scale properties from exascale computations of turbulence on a periodic cube. *J. Fluid Mech.* **1019**, R2.

YEUNG, P.K., SREENIVASAN, K.R. & POPE, S.B. 2018 Effects of finite spatial and temporal resolution in direct numerical simulations of incompressible isotropic turbulence. *Phys. Rev. Fluids* **3**, 064603.

ZECCHETTO, M. & DA SILVA, C.B. 2021 Universality of small-scale motions within the turbulent/non-turbulent interface layer. *J. Fluid Mech.* **916**, A9.

ZEFF, B.W., LANTERMAN, D.D., MCALLISTER, R., ROY, R., KOSTELICH, E.H. & LATHROP, D.P. 2003 Measuring intense rotation and dissipation in turbulent flows. *Nature* **421**, 146–149.